POLITECNICO DI MILANO

Scuola di Ingegneria Industriale e dell'Informazione

Corso di Laurea Magistrale in Ingegneria Fisica

Strategies for the validation of a new algorithm for the local reconstruction of grains with diffraction contrast tomography

Relatore: Dott. Giacomo Claudio Ghiringhelli
Correlatore: Dott. Wolfgang Ludwig

Tesi di Laurea di:
Lorenzo Valzania
Matricola: 798648

Anno Accademico 2013-2014

To my family

To my grandparents

"We are like dwarfs sitting on the shoulders of giants.

We see more, and things that are more distant, than they did,

not because our sight is superior or because we are taller than them,

but because they raise us up, and their great stature adds to ours."

John of Salisbury, *Metalogicon*

Abstract

THREE-DIMENSIONAL synchrotron radiation X-ray diffraction imaging techniques offer the possibility for non-destructive bulk characterization of polycrystalline materials at the micrometer length scale. Minute changes in electron density (different crystallographic phases, cracks, porosities) can be detected using 3D imaging modes exploiting Fresnel diffraction and the coherence properties of third generation synchrotron beams. Three-dimensional X-ray diffraction techniques on the other hand explore the crystalline structure of materials.

By exploiting the symmetry of Friedel pairs, *X-ray diffraction contrast tomography* (DCT) can image the 3D shape, orientation and elastic strain state of the grains in polycrystalline sample volumes containing up to one thousand grains or more. Previously employed reconstruction procedures used to assign one average orientation per grain, lacking sub-grain resolution and failing when intra-granular misorientations are larger than few tenth of a degree.

In this work we explore the possibility of accessing the intra-granular crystallographic structure with a recently developed six-dimensional algorithm sampling the orientation space, which has been already successfully tested on synthetic data sets. For the first time its performances are validated on experimental data. We present a comparison between a grain map obtained from electron backscattering diffraction and the corresponding DCT reconstruction of a titanium sample, thus providing a first cross-validation of the method. Secondly, a comparison between results from the six-dimensional DCT and pinhole and section topography of a magnesium sample provides unprecedented insight into its crystallographic and sub-grain microstructure. Investigating the strong and weak points of the algorithm, the present work stimulates ideas for future improvements, which may be crucial in the study of deformation processes in structural metals employed in engineering.

Sommario

La presente tesi, sviluppata presso la *beamline* ID11 di ESRF (European Synchrotron Radiation Facility, Grenoble), si occupa di una tecnica diffrattiva e non distruttiva di *imaging* ai raggi X, in grado di caratterizzare campioni policristallini su scala micrometrica. Come è noto, le tecniche di *imaging* sono in grado di rivelare lievi cambiamenti nella densità elettronica del materiale (che si manifestano con porosità, transizioni fra fasi differenti, propagazione di stress). D'altra parte, le tecniche tridimensionali basate sulla diffrazione sondano e rendono accessibile la struttura cristallina.

Questa tecnica prende il nome di *diffraction contrast tomography* (DCT), ed è in grado di ricostruire la forma tridimensionale, l'orientazione e lo stato di *strain* elastico di ogni grano in campioni policristallini contenenti fino ad un migliaio di grani. La procedura utilizzata fino a un anno fa circa utilizzava i consueti algoritmi tomografici di ricostruzione tridimensionale ed assegnava un'orientazione media ad ogni grano, rivelandosi inappropriata quando il grano esibisce uno scostamento dall'orientazione media superiore ad alcuni decimi di grado.

Un algoritmo sei-dimensionale recentemente sviluppato permette di assegnare ad ogni grano una vera e propria distribuzione di orientazioni, producendo una ricostruzione della struttura cristallografica intra-granulare del campione. La validità di questo nuovo algoritmo è stata già verificata con successo su dati sintetici. Per la prima volta, verranno effettuate delle prove di validazione utilizzando dati sperimentali.

La tesi è organizzata come segue. Dopo aver motivato l'interesse nello studio della struttura cristallina e delle proprietà meccaniche di molti materiali utilizzati in applicazioni ingegneristiche (**Capitolo 1**), vengono richiamate le basi fisiche necessarie per affrontare problemi di diffrazione ed *imaging* (**Capitolo 2**).

Il **Capitolo 3** contiene una descrizione tecnica della *beamline* presso cui sono stati effettuati quasi tutti gli esperimenti, e le principali tecniche sperimentali impiegate vengono passate in rassegna.

Il **Capitolo 4** tratta la procedura dedicata per DCT per la ricostruzione della microstruttura di campioni policristallini a partire dalle immagini di diffrazione ed assorbimento.

Il **Capitolo 5** esula lievemente dall'argomento del lavoro, e si occupa della ricostruzione di campioni in geometria di acquisizione non perfetta, ovvero in cui l'asse di rotazione non è esattamente perpendicolare al fascio incidente, utilizzando anche in questo caso la tecnica DCT.

Il **Capitolo 6** è il più importante, in quanto si occupa della validazione del nuovo algoritmo. Una prima verifica è essenzialmente un'analisi superficiale, e consiste in un confronto fra una ricostruzione DCT di un campione di titanio ed una mappa di una sua superficie ottenuta tramite *electron backscattering diffraction* (EBSD). In particolare, vengono messe in luce le differenze fra la ricostruzione DCT a sei dimensioni e quella tridimensionale. Successivamente, viene effettuata una seconda verifica dell'algoritmo eseguendo un confronto fra una ricostruzione DCT sei-dimensionale ed i risultati di un esperimento di topografia diffrattiva particolarmente adatto per rivelare le deformazioni all'interno di un campione di magnesio.

Infine, il **Capitolo 7** traccia le conclusioni del lavoro e propone alcune prospettive future.

Contents

List of Figures

List of Tables

Chapter 1

INTRODUCTION

THE majority of structural materials used in classical engineering applications are polycrystalline metallic alloys or ceramics. The crystalline nature of these materials has important consequences on their mechanical behavior since the individual crystals can exhibit anisotropic elastic and plastic properties. For instance, the elastic modulus in the [100] direction of α Fe (ferrite), E_{100} is 141 GPa, whereas E_{111} is 293 GPa, more than twice larger. An agglomerate composed of elastically and plastically anisotropic crystal grains with different crystallographic orientations will therefore develop incompatibility stresses when subject to a global deformation. These local stress and strain inhomogeneities will trigger plastic activity in regions where the yield stress of the material is exceeded. Polycrystalline materials can relax such local stress concentrations by different physical mechanisms like dislocation glide, grain boundary sliding, phase transformations or twinning.

In the absence of external forces the crystalline microstructure may also evolve due to the presence of internal driving forces. From a thermodynamic point of view, a polycrystalline material is always in a metastable state: grain boundaries, the interfaces between neighboring grains, may be regarded as two-dimensional defects of the crystalline lattice and result in a net increase of the free energy of the system. The elastic strain energy induced by the anisotropy of thermal expansion during cooling or the strain energy associated with the storage of dislocations in deformed materials are other examples of internal driving forces, which will cause a polycrystalline microstructure to evolve in time, provided that sufficient activation energy is available. For instance, during the process of recrystallization observed in metals and their alloys, a deformed microstructure with given mechanical properties will change completely and result in a new microstructure with different mechanical properties. Or, when held at elevated temperatures, one may observe the coarsening of grain

structures (grain growth) in polycrystalline materials, a process driven by the system's attempt to minimize the total grain boundary area. The understanding of these deformation and coarsening mechanisms is essential for material scientists and engineers since ultimately it allows for the design and elaboration of materials with improved performances.

Our understanding of the processes involved in thermo-mechanical processing has seen tremendous progress in the course of the last 50 years. Detailed information at ever increasing spatial resolution has been gathered by use of *transmission electron microscopy* (TEM) and *scanning electron microscopy* (SEM) observations. In both cases, the combination of imaging and diffraction modes has proven invaluable for the quantitative interpretation of the underlying mechanisms. In the course of the last decade, extensions of both techniques into three dimensions have been established. *Transmission electron tomography* and *focused ion beam* (FIB) "dual beam" microscopes now provide three-dimensional images of polycrystalline microstructures with spatial resolutions approaching the nanometer and 50 nm level, respectively. However, there are also a number of physical limitations which one can not circumvent in electron microscopy: the strong interaction with matter limits the maximum sample thickness in TEM to values of a few hundreds nanometers, typically. For most structural materials used in engineering applications the grain size is above 1 μm and TEM observations on such thin foils containing only one grain in through thickness direction are not representative for bulk materials since they are affected by the alteration of the stress and strain fields caused by the presence of the (stress-free) surface. Moreover, for the case of SEM, 3D observations obtained by serial sectioning or FIB milling are destructive and *in-situ* observations of the temporal evolution of a given microstructure during thermo-mechanical processing are restricted to the sample surface.

From that point of view, progress in computational micromechanics has by far exceeded the possibilities provided by experimental characterization techniques. For instance, state of the art *crystal plasticity finite element method* (CPFEM) simulations can predict local stress and strain distributions in representative volumes containing several hundred up to thousand grains. These simulations are necessarily based on approximations and simplifications of the physical deformation mechanisms, the full description of which would require coupling of models at different length scales (molecular dynamics, discrete dislocation dynamics, continuum mechanics). There is consequently a need for direct comparison of such model calculations with experimental observations from the bulk of polycrystalline samples. These observations would ideally provide access to physically measurable, local variables of the crystalline lat-

tice like local orientation, elastic strain, defect density and character.

This is where non-destructive, synchrotron X-ray bulk characterization techniques, the topic of this thesis, come into play. Over the last decade, different variants of three-dimensional grain mapping techniques have emerged. Based on diffraction of hard X-rays, which can penetrate up to millimeter thick specimen, these techniques have started to provide quantitative insight in various aspects of polycrystal deformation behavior, observed at the micrometer lengthscale. If combined with three-dimensional X-ray imaging (*microtomography*), these diffraction techniques provide multimodal characterization capabilities comparable to those provided by electron microscopies (e.g. the combination of *electron backscatter diffraction* (EBSD) and secondary electron imaging in a SEM).

In the current manuscript, advances in reconstruction techniques by means of X-ray *diffraction contrast tomography* (DCT) are presented, and validations of an algorithm able to access intra-granular misorientations are discussed.

In **Chapter 2** the fundamental physics behind diffraction and imaging techniques is recalled.

In **Chapter 3** a technical overview of the beamline ID11 at European Synchrotron Radiation Facility (ESRF), Grenoble, is presented, and the main experimental techniques performed are reviewed, with a focus on the DCT method.

Chapter 4 explains how the DCT code processes raw data in order to generate grain maps and provide further insights into the polycrystalline microstructure.

In **Chapter 5** the problem of reconstructing the sample when the rotation axis is not perpendicular to the beam direction because of misalignment errors is described. Then, a simple solution to cope with it is suggested.

Chapter 6 is the most relevant one, since it contains the description of the newly developed six-dimensional algorithm (PhD thesis of Nicola Viganò) and two validation procedures on experimental data are discussed.

Finally, **Chapter 7** sums up the whole work and draws some conclusions, trying to outline some prospects for future developments.

Chapter 2

THEORETICAL BACKGROUND

WITH the increasing number of synchrotron radiation facilities available worldwide and due to significant progress in instrumentation, X-ray methods are of increasing relevance in the field of non-destructive microstructure characterization.

Before addressing the combination of X-ray imaging and diffraction techniques, the basics of image formation processes encountered in X-ray absorption imaging, propagation-based phase contrast imaging and X-ray diffraction imaging (also named *X-ray topography*) are recalled. The extension of these imaging modalities to the third dimension is based on the concepts of image reconstruction from projections. These topics are preceded by a review of the fundamental concepts underlying diffraction of X-rays from crystals.

Most principles included in this paragraph are taken from a textbook on modern X-ray physics [1].

2.1 X-rays and their interaction with matter

X-rays were discovered by Wilhelm Conrad Röntgen in 1895, an achievement that earned him the Nobel Prize in Physics in 1901. Since that time they have become established as an invaluable probe of the structure of matter. The range of materials for which X-rays have proved to be decisive in unraveling the structure is truly staggering. These include at one limit of complexity simple compounds, through to more complex and celebrated examples, such as DNA.

In the 1970s it was realized that the synchrotron radiation emitted from charged particles circulating in storage rings constructed for high energy nuclear physics experiments was potentially much more intense and versatile than conventional (laboratory) sources of X-rays. Indeed synchrotrons have proven to be such vastly better

sources that many storage rings have been constructed around the world dedicated solely to the production of X-rays. This has culminated to date in the so-called third-generation synchrotron sources, which are more brilliant than the early lab-based sources by a factor of approximately 10^{12}, as indicated in Figure 2.1.1.

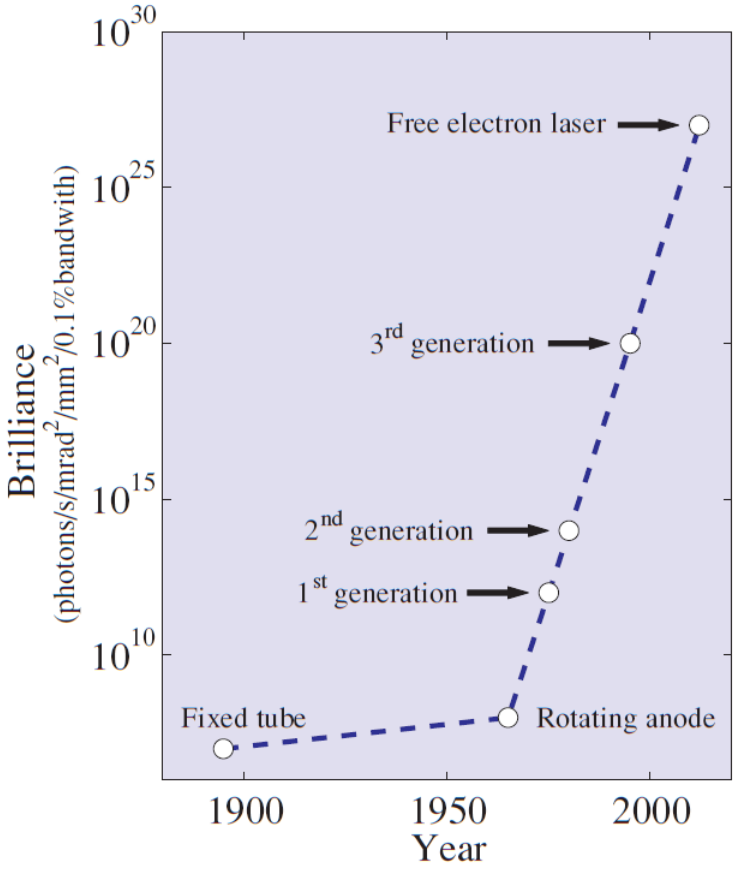

Figure 2.1.1: The brilliance of X-ray sources as a function of time. In the case of *free-electron lasers* (FEL), the average brilliance is plotted. The peak brilliance of a FEL exceeds the average value by a large factor, because of its short pulse length ($\sim$ 100 fs). [1]

In the remainder of this section, all the results shown are true as long as the interaction between the X-ray and the crystal is weak, since multiple reflections of the beam will not be taken into account. This assumption leads to considerably simple treatments and is known as the *kinematic approximation* as opposed to *dynamic* scattering limit.

2.1.1 Elastic scattering from one atom

In the framework of classical physics, the electron distribution within any material is commonly specified by a number density $\rho(\mathbf{r})$. The scattered radiation field is a superposition of contributions from different volume elements of this charge distribution. In order to evaluate this superposition, one must keep track of the phase of the incident wave as it interacts with the volume element at the origin and the one at a generic position **r**, as shown in Figure 2.1.2. The phase difference between two incident rays interacting with the two volume elements is $\mathbf{k} \cdot \mathbf{r}$, where **k** is the wavevector of the incident wave. At sufficiently large distances from the two scattering points, the scattered wave can be regarded as a plane wave with wavevector **k'**. The phase difference between the wave scattered from the volume element around the origin and the one at position **r** is $-\mathbf{k}' \cdot \mathbf{r}$. The resulting phase difference is thus

$$\Delta\phi(\mathbf{r}) = (\mathbf{k} - \mathbf{k}') \cdot \mathbf{r} \equiv \mathbf{Q} \cdot \mathbf{r}$$

where the wavevector transfer or scattering vector $\mathbf{Q} \equiv \mathbf{k} - \mathbf{k}'$ has been defined.

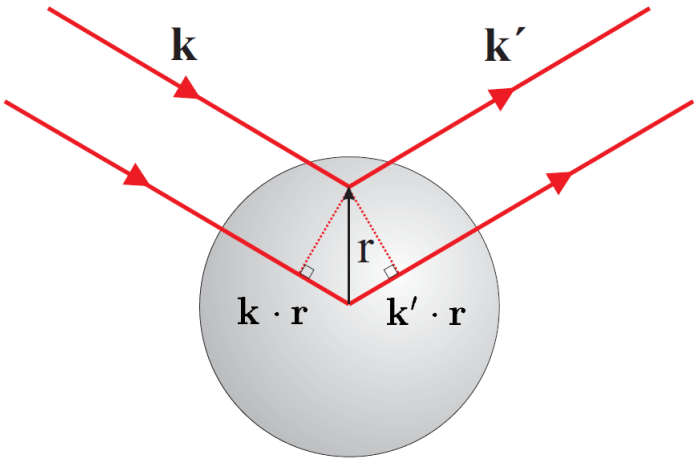

Figure 2.1.2: Scattering of an X-ray beam with wavevector **k** from an atom to the direction specified by **k'**. The scattering is assumed to be elastic, i.e. $|\mathbf{k}| = |\mathbf{k}'|$. The phase difference of the outcoming waves, the first scattered at the origin and the second at position **r**, is $(\mathbf{k} - \mathbf{k}') \cdot \mathbf{r}$. [1]

Since the scattering is elastic, i.e. with $|\mathbf{k}| = |\mathbf{k}'|$, the modulus of the wavevector transfer is $|\mathbf{Q}| = 2\,|\mathbf{k}|\,sin\,\theta = (4\pi/\lambda)\,sin\,\theta$ from the scattering triangle depicted in Figure 2.1.3. Therefore, a volume element d**r** at **r** will contribute an amount $-\,r_0\,\rho(\mathbf{r})\,d\mathbf{r}$ to the total atomic scattering length with a phase factor of $e^{i\,\mathbf{Q}\cdot\mathbf{r}}$. Thus the total scat-

tering length of the atom is

$$-\,r_0\,f^0(\mathbf{Q})\;\equiv\;-\,r_0\int\rho(\mathbf{r})\,e^{i\,\mathbf{Q}\,\cdot\,\mathbf{r}}\,d\mathbf{r}$$

where

$$r_0\;=\;\left(\frac{e^2}{4\,\pi\,\varepsilon_0\,m\,c^2}\right)\;=\;2.82\;\times\;10^{-5}\,\mathring{A}$$

is referred to as the *Thomson scattering length*, or *classical radius*, of the electron, and

$$f^0(\mathbf{Q})\;\equiv\;\int\rho(\mathbf{r})\,e^{i\,\mathbf{Q}\,\cdot\,\mathbf{r}}\,d\mathbf{r}\;=\;\begin{cases}Z & \mathbf{Q}\;\rightarrow\;0\\ 0 & \mathbf{Q}\;\rightarrow\;\infty\end{cases}$$

is known as the *atomic form factor*. One can realize from the last equation that the scattering length can be calculated from the Fourier Transform of the distribution of electrons in the sample. The scattered intensity is thus proportional to the square modulus of this Fourier Transform.

The above calculation is valid as long as the energy E of the incident field is much smaller than any of the absorption edge energy in the atom. Otherwise, two correction terms have to be applied leading to an expression of the atomic form factor like:

$$f(\mathbf{Q},\,E)\;=\;f^0(\mathbf{Q})\;+\;f'(E)\;+\;i\,f''(E)$$

2.1.2 Scattering from a crystal

A crystalline material has the defining property of being periodic in space. Its lattice is thus defined by the relation

$$\mathbf{R_n}=n_1\,\mathbf{a_1}\;+\;n_2\,\mathbf{a_2}\;+\;n_3\,\mathbf{a_3} \tag{2.1.1}$$

where ($\mathbf{a_1}$, $\mathbf{a_2}$, $\mathbf{a_3}$) are the basis vectors of the lattice and (n_1, n_2, n_3) are integers. An elementary treatment of the scattering of X-rays from a crystal lattice was provided by W. L. Bragg and his father W. H. Bragg in 1912. For their important developments in crystallography, they were awarded the Nobel Prize in Physics in 1915. The well known Bragg's law

$$m\,\lambda \;=\; 2\,d\,sin\,\theta \tag{2.1.2}$$

where m is an integer, expresses the condition for the constructive interference of waves having an angle of incidence θ with respect to the surface of a set of lattice planes a distance d apart (Figure 2.1.3). In order to evaluate the scattering amplitude of the crystal, and consequently the intensity of the scattering, one can define a crystal structure by specifying the lattice through lattice vectors $\mathbf{R_n}$ from equation 2.1.1 and the position $\mathbf{r_j}$ of the atoms with respect to each lattice site. Then, the positions of any atom in the crystal is given by $\mathbf{R_n} + \mathbf{r_j}$. It follows that the scattering amplitude for the crystal factorizes into a product like

$$F^{crystal}(\mathbf{Q}) \;=\; \sum_j f_j(\mathbf{Q})\, e^{i\,\mathbf{Q}\,\cdot\,\mathbf{r_j}} \sum_n e^{i\,\mathbf{Q}\,\cdot\,\mathbf{R_n}} \tag{2.1.3}$$

where the first term is called *unit cell structure factor*, and the second term is a sum over lattice sites. The lattice sum in equation 2.1.3 contains phase factors located on the unit circle in the complex plane. The sum will therefore be as large as possible (that is, of order N, the number of unit cells in the crystal) when

$$\mathbf{Q}\,\cdot\,\mathbf{R_n} \;=\; 2\,\pi\,\times\,integer \tag{2.1.4}$$

A unique solution to equation 2.1.4 is found by defining the *reciprocal lattice* as a new lattice spanned by the following vectors:

$$\mathbf{a_1^*} \;= 2\,\pi\,\frac{\mathbf{a_2}\,\times\,\mathbf{a_3}}{\mathbf{a_1}\,\cdot\,(\mathbf{a_2}\,\times\,\mathbf{a_3})}$$

$$\mathbf{a_2^*} \;= 2\,\pi\,\frac{\mathbf{a_3}\,\times\,\mathbf{a_1}}{\mathbf{a_1}\,\cdot\,(\mathbf{a_2}\,\times\,\mathbf{a_3})}$$

$$\mathbf{a_3^*} \;= 2\,\pi\,\frac{\mathbf{a_1}\,\times\,\mathbf{a_2}}{\mathbf{a_1}\,\cdot\,(\mathbf{a_2}\,\times\,\mathbf{a_3})}$$

so that any lattice site in the reciprocal lattice is given by

$$\mathbf{G} \;=\; h\,\mathbf{a_1^*} \,+\, k\,\mathbf{a_2^*} \,+\, l\,\mathbf{a_3^*}$$

where (h, k, l) are all integers. The above equation can be used to calculate the scalar product between a vector in the reciprocal space **G** and one in the direct space $\mathbf{R_n}$:

$$\mathbf{G} \cdot \mathbf{R_n} = 2\pi\,(h\,n_1 + k\,n_2 + l\,n_3) = 2\pi \times integer \tag{2.1.5}$$

By comparing equations 2.1.4 and 2.1.5 it is possible to conclude that

$$\mathbf{Q} = \mathbf{G} \tag{2.1.6}$$

Equation 2.1.6 is the Laue condition for diffraction from a crystalline lattice which may be shown to be completely equivalent to Bragg's law 2.1.2 (for the proof of their equivalence, the reader is referred to any solid state physics book such as Ashcroft and Mermin [2]). Figure 2.1.3 illustrates the Laue condition as well. Scattering from a crystal is thus confined to distinct points in reciprocal space, whose intensities are proportional to the absolute square of the unit cell structure factor. From a large set of intensities from a given crystal one can deduce the positions of the atoms in the unit cell by fitting equation 2.1.3.

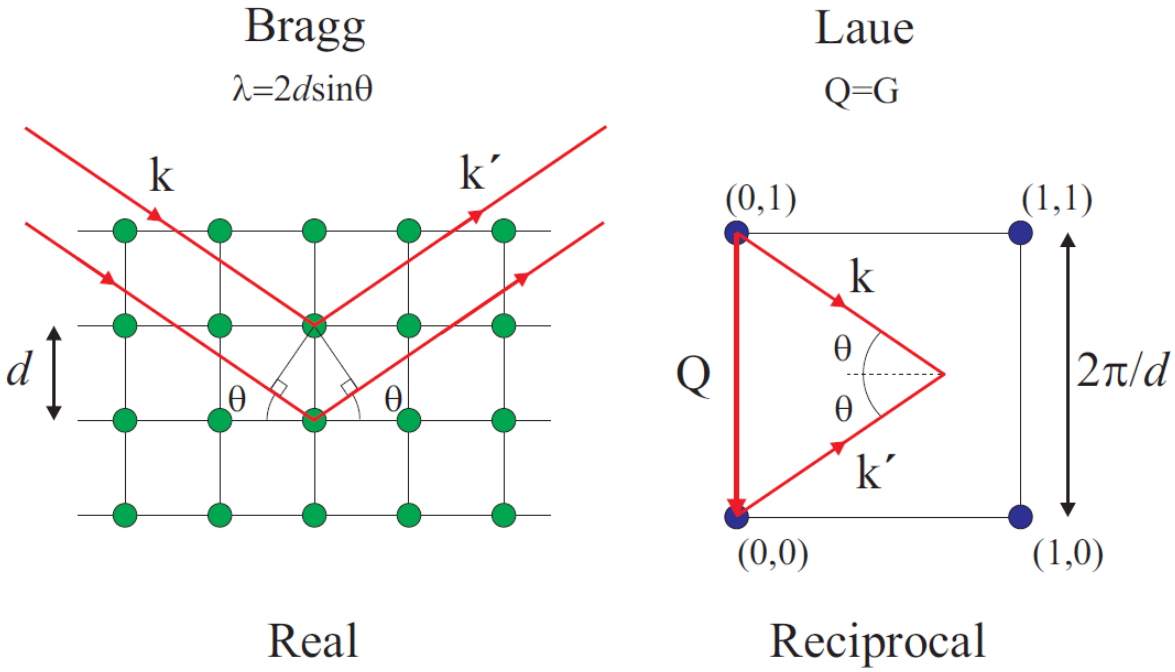

Figure 2.1.3: Comparison between Bragg and Laue condition for diffraction from a 2D square lattice. On the right-hand side, the scattering triangle is indicated in red. [1]

2.2 Introduction to X-ray imaging

X-ray imaging encompasses many fields, which have little in common apart from the desire to produce an image in real space of an object that is invisible to the naked eye. Compared with optical imaging, the two obvious advantages of X-rays are that:

- they can penetrate through matter;
- they have a much shorter wavelength and hence they can potentially produce images with higher spatial resolution.

The former, combined with an imaging contrast due to absorption (the absorption cross section being approximately proportional to the fourth power of the atomic number of the material Z^4), endows X-ray radiography with its usefulness, and explains its wide-spread utility from medicine to materials science. On the other hand, the wave properties of X-rays give rise to a number of advanced imaging techniques allowing the visualization of structures through their ability to scatter an X-ray beam. Although X-ray imaging dates back to the discovery of X-rays themselves, many of these newer imaging techniques rely on the high-brightness and tunability of modern synchrotron sources and consequently have been developed only in recent years.

Scattering or absorption of X-rays when interacting with matter can be included in the expression for the refractive index

$$n \,=\, 1 \,-\, \delta \,+ i\,\beta \tag{2.2.1}$$

with δ proportional to the scattering length density through

$$\delta \,\equiv\, \frac{2\,\pi\,\rho_{at}\,f^0(0)\,r_0}{k^2}$$

and β proportional to the absorption coefficient μ through

$$\beta \,\equiv\, \frac{\mu}{2\,k}$$

This formulation allows describing the amplitude and the phase of X-ray wavefield after transmission through matter by the two-dimensional complex transmittance function

$$T(x,\,y) \,=\, exp\,[-B(x,\,y)]\;exp\,[i\,\phi(x,\,y)] \tag{2.2.2}$$

where $B(x,\, y)$ and $\phi(x,\, y)$ describe the projections of the absorption and refractive index decrements respectively along the beam direction z:

$$B(x,\, y) \,=\, \frac{2\,\pi}{\lambda} \int \beta(x,\, y,\, z)\, dz$$

$$\phi(x,\, y) \,=\, -\frac{2\,\pi}{\lambda} \int \delta(x,\, y,\, z)\, dz \tag{2.2.3}$$

As in general the imaging contrast depends on the spatial variation of the refractive index within the sample, it can be made element specific by tuning an absorption edge around which both δ and β may vary rapidly.

A classification of imaging techniques can be developed by considering the distance from the object to the detector. A plane wave with wavevector **k** incident on two volume elements acting as point sources for spherical waves is considered again. When the phase difference was calculated in 2.1.1 the assumption of infinitely far detector was made (in Figure 2.1.2 both spherical waves are approximated as plane waves of wavevector **k'**). This is the so called *far-field limit* or *Fraunhofer regime*. A better picture of the interaction process is in Figure 2.2.1, where a finite distance from the object to the detector is considered. In this case **k** is perpendicular to **r**, so in the far-field limit we have a phase difference due to a path length difference $\Delta \,=\, OF'$: $\Delta\phi \,=\, (\mathbf{k}' - \mathbf{k}) \cdot \mathbf{r} \,= \mathbf{k}' \,\cdot\, \mathbf{r}$. If the detection point D is closer to the scattering objects, a shortened path length difference must be considered

$$\Delta \,=\, OF' \,- OF \,=\, R \,-\, R\, cos\, \psi \,\approx\, R\,(1 \,-\, (1 \,-\, \psi^2/2)) \,\approx\, a^2/(2\,R)$$

In terms of the three length scales of the problem a, R and λ, the following distinction arises:

$$Fraunhofer\, region:\ \Delta \,\ll\, \lambda \iff R \,\gg\, a^2/\lambda$$

$$Fresnel\, region:\ \Delta \,\approx\, \lambda \iff R \,\approx\, a^2/\lambda$$

$$Contact\, region:\ \Delta \,\gg\, \lambda \iff R \,\ll\, a^2/\lambda$$

In the contact region, the detector is so close to the sample that it becomes meaningless to consider the phase difference between the scattered waves. Then, in this case the imaging contrast arises from differences in absorption between the scatter-

ing points. This clearly shows that the position of the detector has a bearing on the type of image one may expect to observe. An interesting example is the imaging of objects separated by $a \approx 100$ μm (comparable to the grain sizes in most structural materials used in engineering applications) with X-rays with λ = 0.6 $\mathring{A}$ or energy around 20 keV. The ratio $a^2/\lambda \approx 10^2$ m, implying that imaging of objects at atomic resolution is restricted to the contact region.

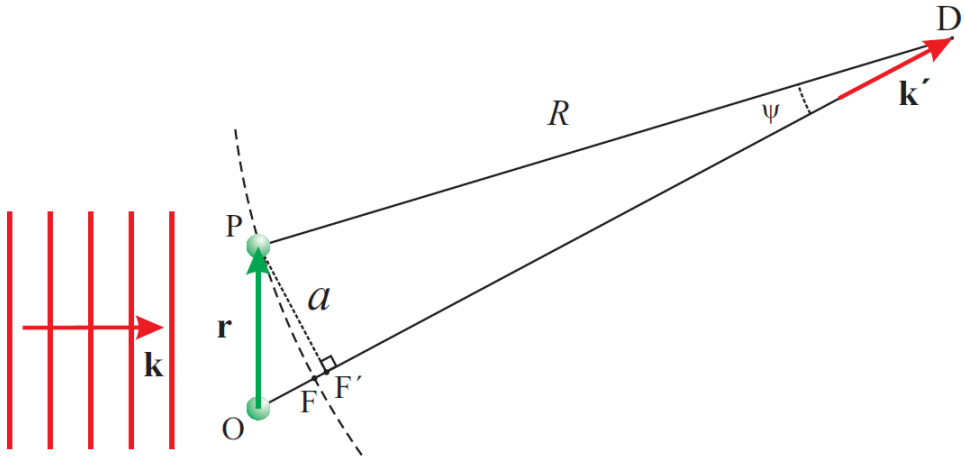

Figure 2.2.1: Interaction of a plane wave with two objects at P and O. Detection point is located at D. [1]

2.3 Absorption contrast imaging

An extremely important breakthrough in medical imaging was made in the 1970's, when Godfrey Hounsfield invented the technique of *Computer Axial Tomography*, now referred to as CAT or CT scanning. The theory underlying CT had been worked out independently in the previous decade by Allan McLeod Cormack, and in 1979 Hounsfield and Cormack were awarded the Nobel Prize in Medicine. CT scanning overcomes the obvious main limitation of conventional radiography which measures a projection of any three-dimensional object onto a two-dimensional plane with a concomitant loss of spatial information. It does this by recording radiographic projections of the object over a wide range of projection angles, from which it is then possible to reconstruct the full three-dimensional structure.

To understand how it works, the absorption of a perfectly narrow X-ray beam in the plane of a two-dimensional object is considered, as sketched in Figure 2.3.1. The beam along the y' axis views the object at an angle θ with respect to the fixed (x, y) coordinate system. For generality the absorption coefficient of the object is assumed

to be non-uniform $\mu(x, y)$. The intensity recorded in a detector located behind the sample corresponds to the intensity recorded by a detector placed at the exit plane of the object and is calculated with the aid of the complex transmittance function T in equation 2.2.2 through

$$I = |T\, u_{inc}|^2 \tag{2.3.1}$$

Its evaluation leads to the well known Lambert-Beer law:

$$I = I_{inc}\, exp\left[-\int \mu(x, y)\, dy'\right] \quad \Longleftrightarrow \quad ln\left(\frac{I_{inc}}{I}\right) = \int \mu(x, y)\, dy' \tag{2.3.2}$$

The ratio of the intensity of the primary beam to that measured in the detector thus gives the integral of the absorption coefficient along a particular direction y' at viewing angle θ and coordinate x'. Scanning the beam parallel to x' for a fixed θ will produce an intensity distribution $R(\theta, x')$ known as *Radon Transform*. The CT scan may therefore be thought as a series of Radon Transforms collected at a set of viewing angles.

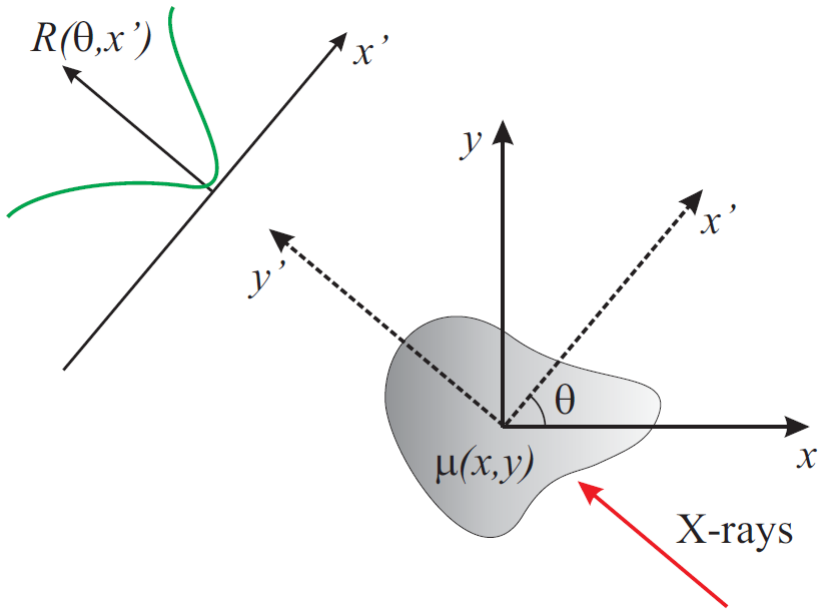

Figure 2.3.1: A narrow X-ray beam incident on an object with a two-dimensional absorption coefficient $\mu(x, y)$. The line integrals $R(\theta, x')$ performed along the propagation direction of the beam y' are known as Radon Transforms and are functions of the viewing angle θ and the coordinate x' perpendicular to y'. [1]

2.4 Phase contrast imaging

The family of phase contrast imaging techniques relies on the refraction of X-rays when they impinge in the material. As discussed in the previous sections, the phase difference of the refracted beam can be written as $\phi = \mathbf{k}' \cdot \mathbf{r}$. The direction of the refracted beam is thus proportional to the gradient of the phase:

$$\frac{\mathbf{k}'}{k'} = \frac{\lambda}{2\,\pi} \nabla\phi(\mathbf{r})$$

It follows that the angular deviation as a function of the coordinates (x, y) in the plane perpendicular to the direction of propagation of the incident beam is given by the two angles

$$\alpha_x = \frac{\lambda}{2\,\pi} \frac{\partial\phi(x,\,y)}{\partial x}$$

$$\alpha_y = \frac{\lambda}{2\,\pi} \frac{\partial\phi(x,\,y)}{\partial y}$$

This means that, by measuring α as a function of (x, y), the phase $\phi(x,\,y)$ can be determined by integration. In Figure 2.4.1 the energy dependence of deviations of the refractive index from unity are reported as a function of the atomic number. For hard X-rays, δ can be up to three orders of magnitude larger than β at energies above 10 keV. This results in a tremendous gain in sensitivity when using phase contrast imaging instead of absorption contrast imaging. Table 2.4.1 gives some values of δ and β at 20 keV for some representative materials used in engineering applications.

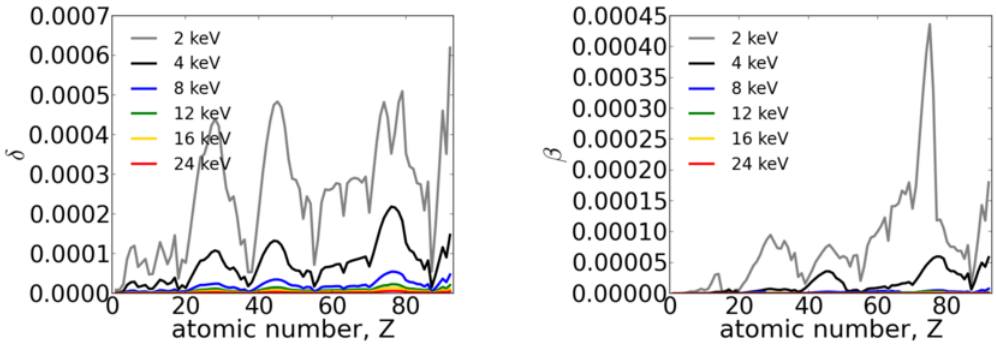

Figure 2.4.1: Energy and atomic number dependence of real (left) and imaginary (right) deviations from unity of the refractive index in the X-ray region. δ is found to be larger than β, especially for heavy elements. [3]

Material	$\delta\,(10^{-6})$	$\beta\,(10^{-8})$	δ/β	$\mu\,(cm^{-1})$	$1/\mu\,(cm)$
Beryllium	0.85	0.004	2.1×10^4	8.2×10^{-2}	12.19
Aluminum	1.4	0.4	3.3×10^2	8.2	0.12
Titanium	2.2	3.4	6.4×10^1	6.9×10^1	0.014
Iron	3.8	9.6	4.0×10^1	1.9×10^2	0.0052
Nickel	4.5	14	3.2×10^1	2.8×10^2	0.0035
Zirconium	2.9	24	1.2×10^1	4.8×10^2	0.0021

Table 2.4.1: Complex refractive index decrements for some representative materials at 20 keV. [4]

A logarithmic subtraction of incoming and transmitted intensities is enough to obtain the projection of the linear attenuation coefficient μ along the beam direction, according to equation 2.3.2. The retrieval of the refractive index decrement (equation 2.2.3) is much more complicated and challenging, since the phase information is lost and only intensities are recorded on the detector screen. For weak defocussing conditions it can be shown [5] that the intensities, recorded after propagation over a distance D, can be approximated as a product of an absorption and a phase contribution. The former is identical to the one in absorption radiography ($D = 0$, equation 2.3.2), and the latter depends on the two-dimensional laplacian of the phase. The overall expression is

$$I_D(x,\,y) \,=\, I_{inc}(x,\,y)\,exp\left[-\int \mu(x,\,y,\,z)\,dz\right]\,exp\left[-\frac{\lambda\,D}{2\,\pi}\,\nabla^2\phi(x,\,y)\right] \tag{2.4.1}$$

Logarithmic subtraction of incoming ad transmitted intensities therefore yields

$$ln\left(\frac{I_{inc}(x,\,y)}{I\,(x,\,y)}\right) \,=\, \int \mu(x,\,y,\,z)\,dz \,+\, \frac{\lambda\,D}{2\,\pi}\,\nabla^2\phi(x,\,y)$$

and the reconstructed quantity can be approximated to (making use of equation 2.2.3)

$$g(x,\,y,\,z) \,=\, \mu(x,\,y,\,z) \,-\, D\,\nabla^2\delta(x,\,y,\,z)$$

The second term contributes to $g(x,\,y,\,z)$ in regions of the object where there are strong variations in the refractive index, acting as a form of enhancement in boundaries between different phases.

2.4.1 Phase retrieval

The computation of the phase shift $\phi(x, y)$ from the intensity distribution 2.4.1 measured at one or several distances has been a hot topic of research for more that ten years. Depending on the assumptions on the object, different formulations have been proposed (an overview on this topic can be found in [6]). For example, Paganin's approach [7] applies to homogeneous objects, with a single acquisition distance. The *mixed transfer function* [8] is based on the acquisition at multiple distances and applies to the case of objects with non-negligible absorption.

2.5 Reconstruction techniques

The goal of reconstructing an unknown object from a set of projections or line integrals was accomplished through a variety of mathematical formalism over the past decades. Two frequently used reconstruction approaches will be briefly discussed here: Fourier analysis techniques, or analytical techniques, or *Filtered Back-Projection* (FBP), and *Algebraic Reconstruction Technique* (ART). The most used is the former, since it is the fastest one and gives the best results when several projections are taken. The latter tends to perform better in terms of noise when less projections are available and some angles are missing (see Figure 2.5.1 for a quick comparison between the two approaches with a variable number of projections). Moreover, it allows to introduce corrections in a relatively straightforward way. For more information about the theory behind them, the books by Kak and Slaney [9] and Herman [10] are suggested to the interested reader.

2.5.1 Filtered Back-Projection

The basic concept behind analytical techniques is a fundamental theorem which is now derived.

Consider a general two-dimensional function $f(x, y)$ which is projected (integrated) along the y axis to generate a new function of x only:

$$p(x) = \int f(x, y)\, dy$$

Its Fourier Transform is

$$P(q_x) = \int p(x)\, e^{i\, q_x\, x}\, dx$$

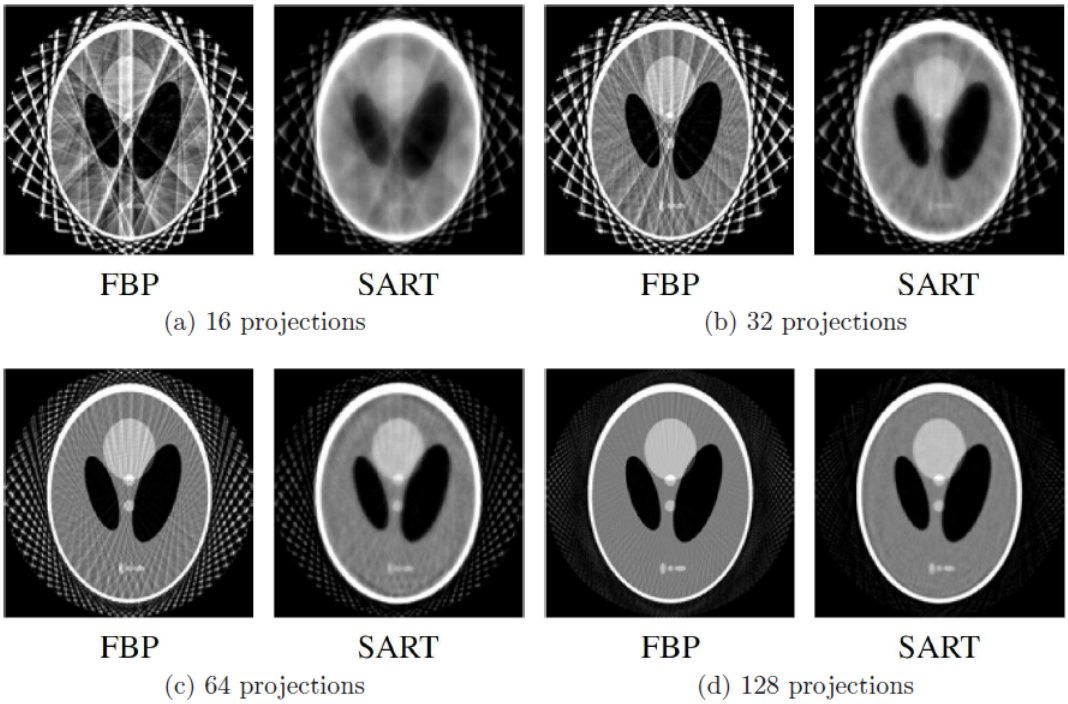

Figure 2.5.1: Comparison of reconstruction quality between FBP and ART, with increasing number of projections. [11]

while the Fourier Transform of the original function $f(x,\, y)$ is

$$F(q_x,\, q_y) \;=\; \int\int f(x,\, y)\, e^{i\,(q_x\, x\, +\, q_y\, y)}\, dx\, dy \tag{2.5.1}$$

Evaluation of equation 2.5.1 in $q_y \;=\; 0$ defines a slice through $F(q_x,\, q_y)$ given by

$$F(q_x,\, q_y \;=\; 0) \;=\; \int \left[\int f(x,\, y)\, dy\right]\, e^{i\, q_x\, x}\, dx$$

Now the term in square brackets can be easily recognized as $p(x)$, thus allowing to write

$$F(q_x,\, q_y \;=\; 0) \;=\; \int p(x)\, e^{i\, q_x\, x}\, dx \;=\; P(q_x)$$

Hence one can state the following

Theorem 2.5.1. ***Fourier Slice Theorem (Figure 2.5.2).*** ***[9]*** *The one-dimensional Fourier Transform of a parallel projection of a two-dimensional object function f(x, y) at an angle θ with respect to the x-axis, gives a slice of the two-dimensional Fourier Transform F(q_x, q_y) of the function f(x, y) at an angle θ with respect to the q_x-axis.*

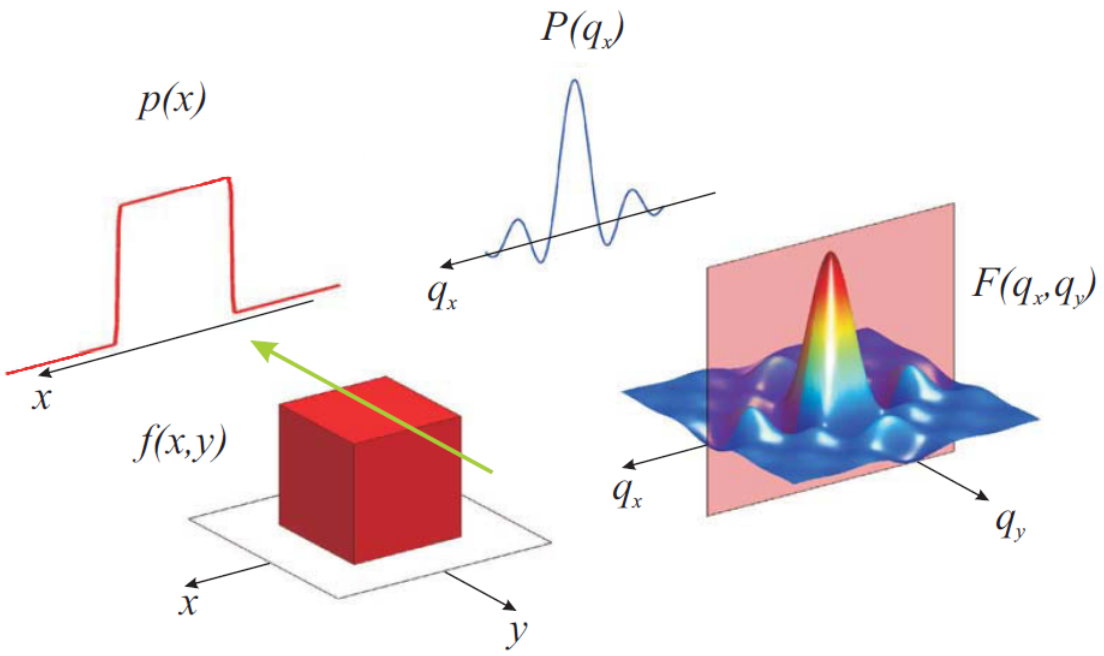

Figure 2.5.2: Illustration of the Fourier Slice Theorem. In this case $F(q_x, q_y) = [sin\,(q_x\,x)/(q_x\,x)]\,[sin\,(q_y\,y)/(q_y\,y)]$. The Fourier Transform of the function $f(x, y)$ projected along the y axis $p(x)$ is $P(q_x) = [sin\,(q_x\,x)/(q_x\,x)]$, which is the $q_y = 0$ slice through $F(q_x, q_y)$. [1]

From the above theorem, the process of CT scanning and FBP reconstruction can be thought of as comprising three key steps:

1. Acquisition of the data as a series of radiographs, i.e., as a series of Radon Transforms $R(\theta, x')$ taken at different viewing angles θ. The plots of the calculated Radon Transforms $R(\theta, x')$ are known as *sinograms*;

2. Fourier Transform of the data $R(\theta, x')$. From the Fourier Slice Theorem, the Fourier Transform of the object can be reconstructed;

3. Anti Fourier Transform to get the reconstructed image of the object.

2.5.2 Algebraic Reconstruction Techniques

The first step of this approach is to superimpose a square grid on the image $f(x, y)$ (Figure 2.5.3). Let $f(x, y)$ be constant in each cell of the grid and f_j , $j = 1, 2, ..., N$ be this constant value in the j-th cell.

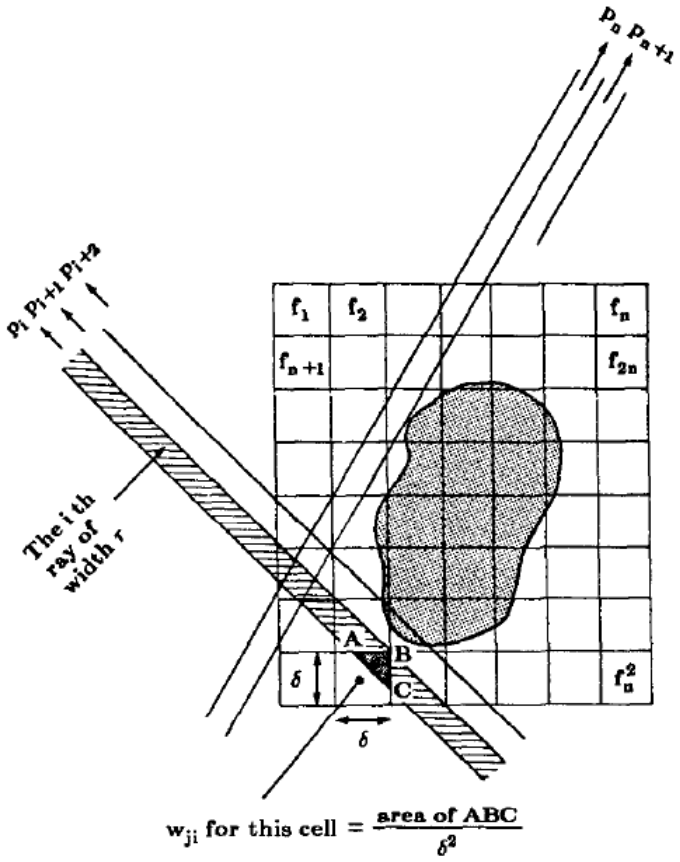

Figure 2.5.3: Superimposition of the square grid and illustration of ray-sums used in ART. [9]

Ray-sums p_i are defined as line integrals measured over rays of finite width and are supposed to be related to the f_js by the following linear relations:

$$\sum_{j=1}^{N} w_{ij} f_j = p_i \qquad i = 1, 2, ..., M$$

Here, M is the number of rays in all the projections and w_{ij} is the weighting factor that represent the contribution of the j-th cell to the i-th ray integral. w_{ij} also corresponds to the fractional area of the j-th image cell intercepted by the i-th ray. The linear system to solve is then

$$\mathbf{W}\,\mathbf{f} = \mathbf{p} \tag{2.5.2}$$

but it is usually impossible to invert it because M and N are of order 10^4 and some noise may be present in the measurement data. For large values of M and N there

exist very attractive iterative methods for solving 2.5.2, like the *Simultaneous Iterative Reconstructive Technique* (SIRT), for a discussion of which the reader is referred to [9]. All these algorithms are based on the *method of projections* as first proposed by Kaczmarz [12] and refined by Tanabe [13].

Chapter 3

BEAMLINE ID11 AT ESRF AND ITS EXPERIMENTAL TECHNIQUES

BEAMLINE ID11 at ESRF is a multipurpose, high flux and high energy beamline, concentrating on 3D grain mapping, diffraction, and *Pair Distribution Function* (PDF) experiments in the area of materials science.

In the first part of this chapter (sections 3.1 to 3.6), a technical overview of beamline ID11 will be presented, with particular focus on experimental facilities and instrumentation. The second part (section 3.7) deals with the main techniques performed.

3.1 Structure of the beamline

Beamline ID11 consists of five operating sections: (1) the X-ray source; (2) the primary optics and (3) the first experimental hutch; (4) the secondary optics and (5) the second experimental hutch.

Figure 3.1.1 schematically shows their locations along the beamline and their distances from the storage ring. Sections are indicated as Source, OH1, EH1, OH2, and EH3, respectively.

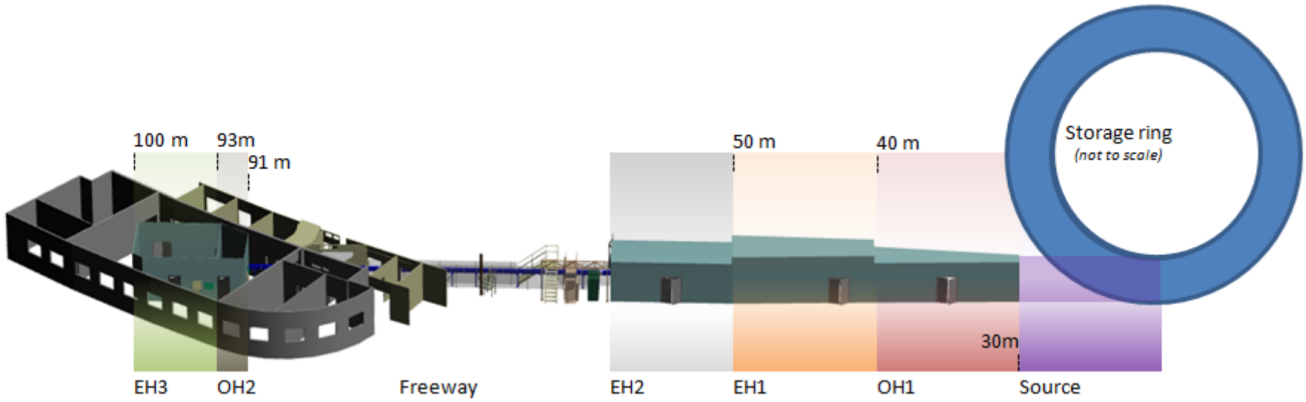

Figure 3.1.1: ID11 piste map schematic. The sections are indicated as Source, OH1 (primary optics hutch), EH1 (first experimental hutch), OH2 (secondary optics hutch), and EH3 (second experimental hutch). EH2 refers to an experimental hutch which is no longer operational. [15]

3.2 X-ray source

The radiation source for ID11 is provided by an in-vacuum undulator. Figure 3.2.1 shows the working principle of the undulator. It consists of a periodic structure of dipole magnets creating a static magnetic field which is alternating along the length of the undulator with a wavelength λ. Electrons traversing the periodic magnetic structure undergo oscillations and radiate an energy which is characteristic of relativistic electrons. The radiation produced in an undulator is very intense, it is concentrated in a narrow energy bands in the spectrum, and it is also collimated on the orbit plane of the electrons. An important figure of merit is the *undulator strength (or deflection) parameter*

$$K = \frac{e\,B\,\lambda}{2\,\pi\,m_e\,c} \tag{3.2.1}$$

where e is the electron charge, B is the magnetic field, m_e is the electron rest mass, and c is the speed of light. If $K \approx 1$ the oscillation amplitude of the motion is small and the radiation displays interference patterns which lead to narrow energy bands. If K is larger (typically $K \geq 10$) the oscillation amplitude is bigger and the radiation contributions from each field period sum up independently, leading to a broad energy spectrum. In this regime of fields the device is no longer called an undulator, it is called a *wiggler*. The reader can become familiar with the general formalism of

radiation emitted by relativistic electrons by reading [16].

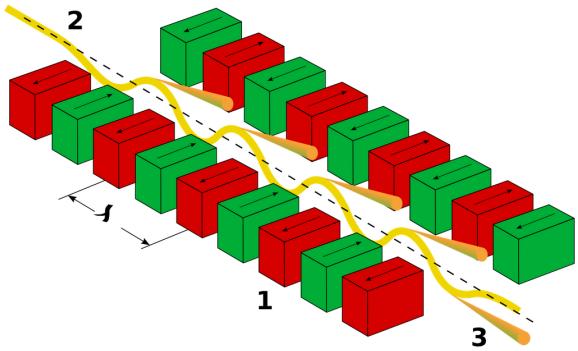

Figure 3.2.1: Working principle of an undulator. 1: magnets; 2: electron beam entering from the upper-left; 3: synchrotron radiation exiting to the lower right. [17]

The undulator used is of type U22 (Figure 3.2.2) and is a 22 mm-period undulator whose length is 2 m. Some results of magnetic measurements are displayed in Figure 3.2.3. The effective magnetic field peak decreases by increasing the distance between the upper and lower magnets (also known as the undulator gap). U22 is used with a 6 mm gap, thus giving a field peak around 0.9 T and a deflection parameter $K \approx 2$. As a result, the energy spectrum is considered discrete (like in the usual working conditions of an undulator as opposed to a wiggler) and consists of energetically equally spaced peaks.

Figure 3.2.2: Photograph of an hybrid U22 undulator. The gap, that is, the distance between upper and lower magnets, is higher than the values which are practically used. [18]

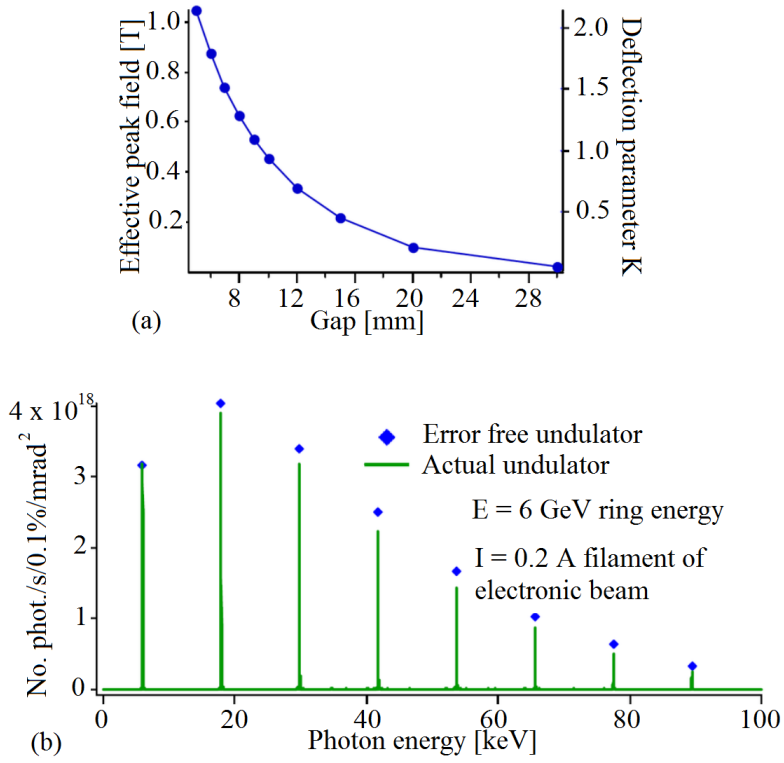

Figure 3.2.3: Magnetic measurements performed on U22 undulator. (a) Measured magnetic field as a function of the undulator gap. The magnetic field is directly proportional to the strength (or deflection) parameter K according to equation 3.2.1. (b) Angular flux of emitted photons as a function of their energy (the undulator was used with a 6 mm gap). [18]

3.3 Primary optics

The primary optics are located on optics hutch 1 (OH1) and serve the whole beamline. Energy selection is provided by a double bent crystal Si(111) monochromator operating in horizontal Laue geometry. The maximum energy range available is from 22.7 to 141.7 keV [14] though, operationally, ID11 is optimized to work at energies above 35 keV. Focusing of the beam can be achieved using an in-vacuum transfocator. It enables focusing throughout the entire energy range (the smallest focal spot achieved is $\sim 50\ \mu\text{m} \times 220\ \mu\text{m}$) in EH3, and up to 75 keV in EH1 (spot sizes being $\sim 6\ \mu\text{m} \times 45\ \mu\text{m}$).

In the rest of this section, the monochromator in Laue-Laue geometry and the transfocator will be described in more detail.

3.3.1 Laue-Laue monochromator

Bent crystals as focusing monochromators have been widely used with conventional X-ray sources, and also at low-energy synchrotron radiation beamlines.

The focal lengths of a thin, bent perfect crystal are given by the lens equation, although the X-rays are not refracted or reflected by the surface of the crystal, but by the atomic planes inside the crystal. Figure 3.3.1 illustrates different focusing cases.

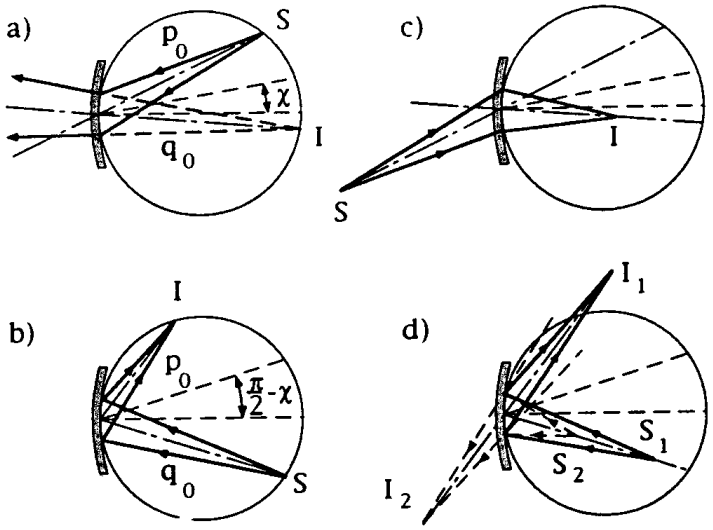

Figure 3.3.1: Focusing by an ideal, cylindrically bent crystal. (a) is the transmission (Laue) case when the source S (real) and image I (virtual) are on the Rowland circle; (b) is the reflection (Bragg) case for monochromatic focusing; (c) is the polychromatic focusing by a Laue crystal; (d) is the polychromatic focusing by a Bragg crystal. In (c) and (d) the image is either real or virtual, depending on the location of the source. [19]

Focal distances are related through [19]

$$q = \frac{q_0}{2 - \frac{p_0}{p}}$$

where

$$p_0 = \rho\,\gamma_0 = \rho\,cos\,(\chi + \theta) \qquad q_0 = \rho\,\gamma_h = \rho\,cos\,(\chi - \theta)$$

Here ρ is the bending radius, θ is the Bragg angle, χ the angle between the reflecting (Bragg) planes and the surface normal of the crystal, and γ_0 and γ_h are the directions cosines of the incident beam and the reflected beams, respectively. The sign convention is such that p and q are positive on the concave side of the crystal. The

crystal reflects a band of energies from a beam of height (or width) h according to the following

$$\frac{\Delta E}{E} = \left[h \left(\frac{1}{p_0} - \frac{1}{p} \right) \right] cot\,\theta$$

so the focusing is monochromatic when the source and the image are on the Rowland circle; i.e. $p = p_0$ and $q = q_0$. In particular, in the transmission (Laue) case the monochromatic focus is virtual. Referring to Figure 3.3.2, which shows the bent double-Laue geometry, the white beam is incident on the first Laue crystal, cylindrically bent to a Rowland circle going through the source S1. Such a bent radius allows all the rays from the source to make the same incidence angle with respect to the crystal planes. The singly diffracted beam emerges as if emanating directly from a virtual source S2, also located on the first Rowland circle. To restore the beam parallel to the original direction and provide a tunable in-line system, a second crystal is introduced and is also bent, but to a Rowland circle going through the virtual source S2. The doubly diffracted beam propagates as if coming from the virtual source S3 located on the second Rowland circle and close to the original source S1.

In the high energy regime, the Laue-type monochromators provide more flexibility in construction than the Bragg-type monochromators. Absorption is not a limiting factor, and χ can be chosen in a wide range, so that the width of the reflectivity curve and the energy band-pass can be tailored to the requirements of the experiment. In addition, the angle between the incident beam and the crystal surface is usually quite large, reducing geometrical aberrations.

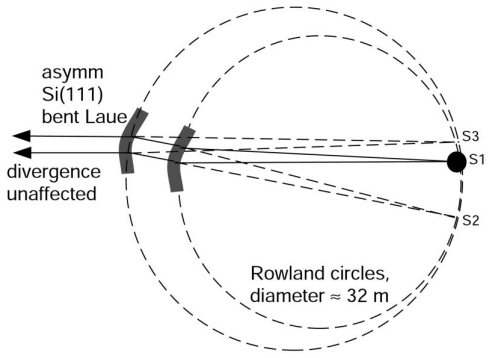

Figure 3.3.2: Tunable in-line monochromator of two vertically diffracting bent Laue crystals located at about 32 m from the undulator source S1. The two Rowland circles intersect tangentially at the virtual source S2. [20]

The monochromator in use at ID11 beamline (Figure 3.3.3) is provided with a pair of Si(111) crystal 2.5 mm thick and with 12.5° asymmetric cut, thus giving an energy resolution $\Delta E\,/\,E \simeq 10^{-3}$ and an energy range between 22.7 keV and 141.7 keV. Three main requirements were imposed by the operation conditions on the beamline:

- a fixed exit offset of 10-15 mm;
- provide low photon energy ($\approx$ 23 keV) when the crystals are close one to each other ($\approx$ 58 mm);
- the mechanical bender should accept rectangular and triangular crystals.

It consists of 14 motorized axes all equipped with limit switches. Among them, 7 are encoded axes. The main rotation (Bragg angle selection) axes are equipped with a piezo actuator for fine movements: rotation offsets from 0° to 15° are possible in order to accommodate crystals with different asymmetric cuts. Between the two stages there is a protective water cooled tungsten beam mask to stop the white beam. Two additional linear stages allow filter selection and diode insertion or removal. Two benders have been foreseen, one for each crystal, and are configurable for different crystal shapes and thicknesses. A horizontal scattering geometry was chosen to preserve the quality of the source in the vertical plane so that subsequent focusing with other elements is possible.

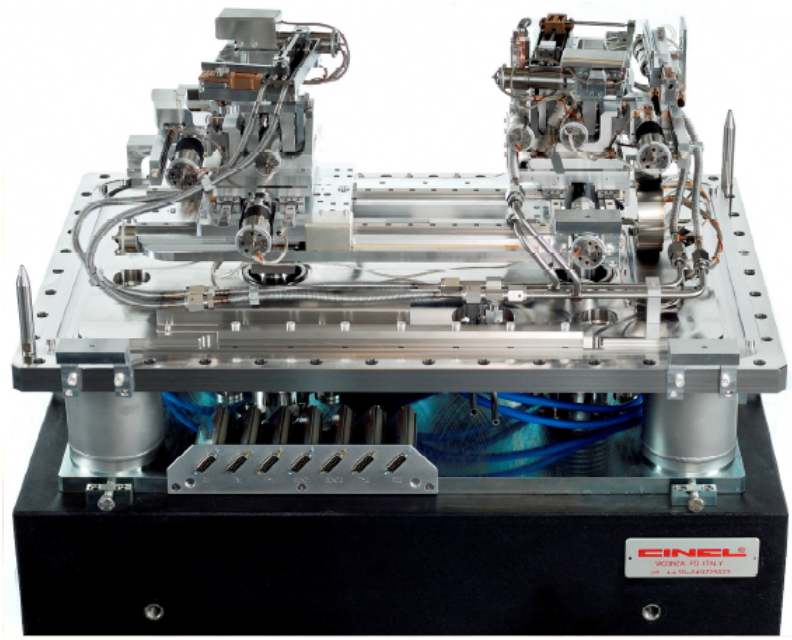

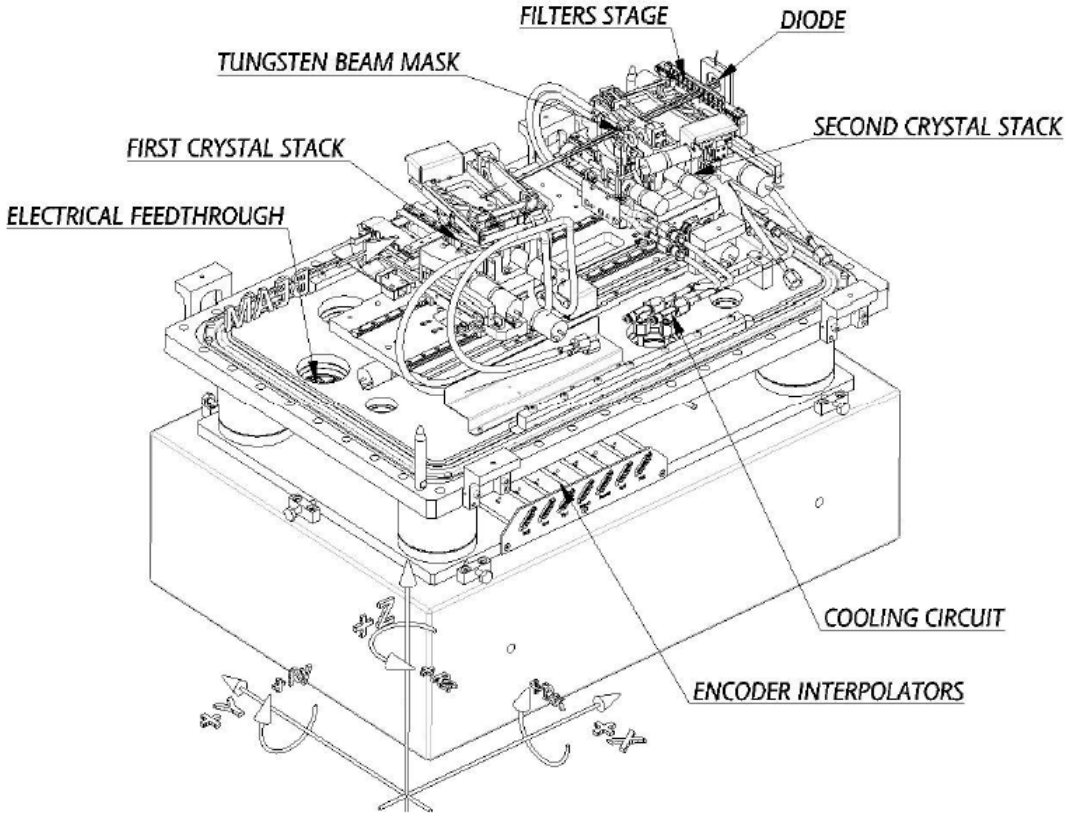

Figure 3.3.3: Overview of the Laue-Laue monochromator. Top (previous page): photograph. Bottom: schematic. [21]

3.3.2 In-vacuum transfocator (IVT)

Compared with other focusing elements, refractive lenses present several attractive features, being simple to align and relatively insensitive to misorientations. Since refractive lenses are in-line optics, they are more stable with respect to angular vibrations in comparison with deflecting optics. Moreover, they can be adapted to very high X-ray energies by modifying their composition and number. As the refraction index for refractive lenses is extremely close to 1 and energy-dependent (section 2.4), a substantial well defined number of lenses are necessary to focus X-rays of a given energy at a given distance. Elements with a tunable number of lenses are called transfocators and are comprised of several cartridges containing a geometric progression of numbers of lenses, such that the focal distance can be continuously adjusted by insertion or retraction of one or more of the lens cartridges.

Based on the design of *in-air transofcators* (IAT), the IVT is considerably more complex from an engineering viewpoint, as the cartridges must translate in vacuum, must be water cooled, and the entire chamber is considerably larger. It consists (Figure 3.3.4) of nine water-cooled cartridges containing 1, 2, 4, 8, 16 and 32 Be lenses, and 32 and 64 Al lenses. The combination of these cartridges allows complete tunability between 18 and 125 keV at 94 m (EH3), and 18 to 75 keV at 42 m (EH1).

Figure 3.3.4: Photograph of the IVT taken during assembly. [22]

A very simple approximation can be used to compute the lens requirements. One Be lens has a focal length in meters given by $k\,E^2$, where E is the X-ray energy in keV and $k \approx 0.296$ m keV^{-2}. An Al lens has a focal length equivalent to ~ 1.568 times the focal length of Be lenses. The number of lenses required at ID11 can then be computed simply via the lens equation:.

$$\frac{1}{S_1\,[m]} + \frac{1}{S_2\,[m]} = \frac{1.568\,n_{Al} + n_{Be}}{0.296\,E\,[keV]^2} \tag{3.3.1}$$

where S_1 and S_2 are the object and calculated image distances, as shown in Figure 3.3.5. From equation 3.3.1 the following relations are obtained:

$$at\ 42\,m\ distance\ from\ the\ source: \qquad 1.568\,n_{Al} + n_{Be} = 0.0376\,E\,[keV]^2 \tag{3.3.2}$$

$$at\ 94\,m\ distance\ from\ the\ source: \qquad 1.568\,n_{Al} + n_{Be} = 0.0141\,E\,[keV]^2 \qquad (3.3.3)$$

In the first experimental hutch (EH1), at 41-44 m from the source, the transfocator can be used to microfocus producing spots on the order of 6 μm $\times$ 45 μm. For the end station (EH3) at 95 m, the smallest focal spot currently produced is on the order of 50 μm $\times$ 220 μm.

A further interesting characteristic of using refractive lenses for focusing/pre-focusing is that the focusing of the lenses is chromatic, so that only a single energy is focused at a given distance, as opposed to typical periodic monochromators such as crystals and multilayers, in which higher order reflections diffract multiples of the fundamental energy. This gives the useful side benefit of suppression of harmonics in the focused beam. This characteristic also means that the transfocator can be used without any other optics as a longitudinally dispersive focusing monochromator, with a band pass proportional to the focal length. Further information about this specific use can be found in [22].

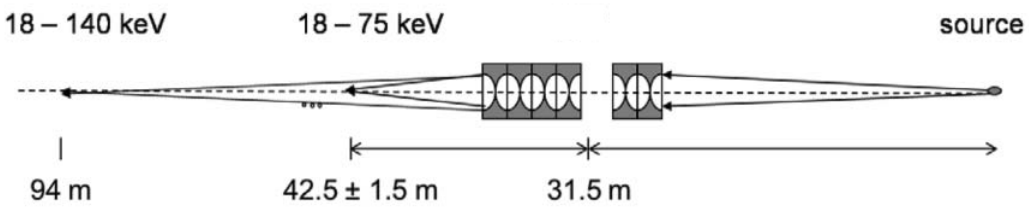

Figure 3.3.5: Schematic of focusing properties of the IVT. [22]

3.4 First Experimental Hutch

The first experimental hutch (EH1) is the heavy duty workstation whose main instrument is a Huber diffractometer with vertical rotation axis offering a very large working area and high load capacity, suitable for complex sample environments.

3.4.1 Beam definition

The beam can be defined using the slit system situated on the Huber tower. This consists of a set of xx type slits mounted in front of a further set of Huber tube slits (Figure 3.4.1). The tube slits are in-vacuum allowing a means of defining the X-ray beam as close to the sample position as possible and reduce the effect of air scattering.

They also act as anti-scatter slits when the regular slits are used to define the beam.

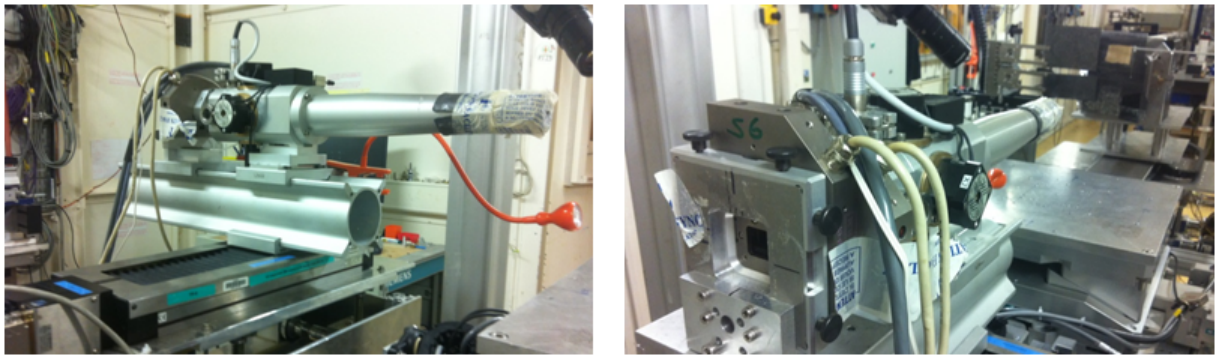

Figure 3.4.1: Beam defining apparatus available in EH1, consisting of a set of regular slits preceding a set of Huber tube slits. [15]

3.4.2 Diffractometer

The Huber diffractometer was installed in 2008 and offers a very large working area and load capacity (>100 kg) for complex sample environments, while maintaining $\sim$ 2 μm sphere-of-confusion and linear positional accuracy. Either white beam or monochromatic X-ray beams are available, with energies of 25-140 keV and sizes of 0.8 mm $\times$ 0.8 mm (H $\times$ V) down to 20 μm $\times$ 7 μm (H $\times$ V). By exploiting the fast readout of the Frelon camera and high X-ray flux, 2D diffraction images can be collected very quickly, allowing time resolved in-situ studies to be carried out. Due to the vertical rotation axis, this instrument can also be used for single crystal diffraction. If required, a second rotation axis can be added in a fixed kappa angle geometry to provide single crystal data which are highly complete and redundant. Figure 3.4.2 shows photographs and schematics of translations and rotations stages available on the EH1 diffractometer. Both the stages and the Huber tower holding the slits are mounted on an x-translation platform.

3.4.3 Detector arrangement

The detector is typically a two-dimensional CCD FReLoN 2k, which is mounted on two x-translations, allowing a wide range of scattering vectors to be accessed depending on the detector-beam stop and the detector-sample positions. There are also two z-translations, allowing the detector to be tilted. Other motors are also available, though not pictured, which may be mounted on the diffractometer such as a sample spinner and other angular rotations. Figure 3.4.3 shows photographs and schematics of the detector tower arrangement and translations. Table 3.4.1 contains other

important parameters of the detector.

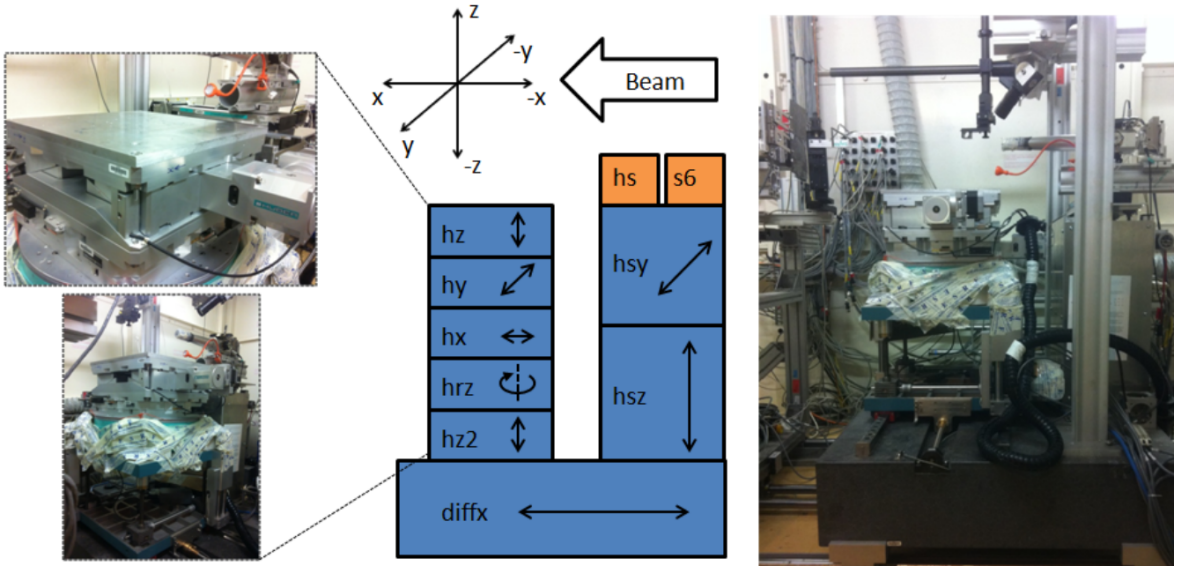

Figure 3.4.2: Translations and rotations stages available on the diffractometer and Huber tower containing the slits: Huber (hs) and regular (s6). Available movements are indicated as black arrows. The beam direction and the laboratory coordinate system are also shown. [15]

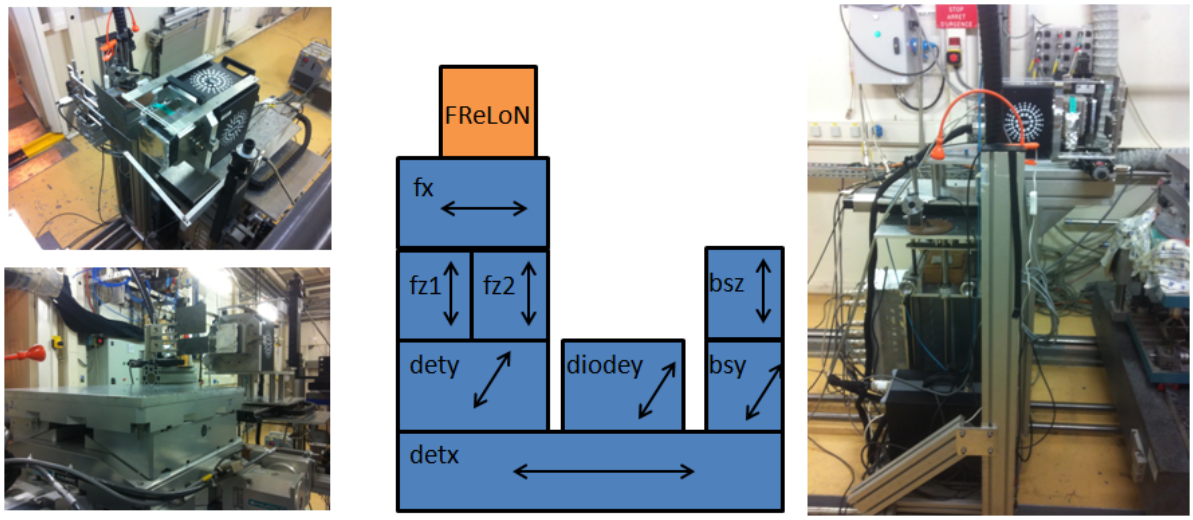

Figure 3.4.3: Detector tower arrangement and translations. Available movements are indicated as black arrows. The available movements of the beam stop (bsy/z) are also shown. [15]

Channel size	Number of channels	Dynamic Range	Minimum readout time
depends on coupling	2048×2048	2^{16}	125 ms

Table 3.4.1: FReLoN 2k detector properties. Note that the effective pixel size depends on the coupling with the phosphor screen and camera optics.

3.5 Secondary optics

The second optics hutch (OH2) is situated before the second experimental station (EH3), 92 m from the source and 1.5-2 m away from the sample position. The variety of optical systems here allows for a range of microfocused beam options for applications in EH3. They include an in-air transfocator (IAT) and a Kirkpatrick-Baez (KB) mirror. The operating principles for the former are the same as for the IVT, but the shorter focal distance (1.2-1.7 m) means that it can be used to focus down to the μm level. It can be translated along the beam to accommodate any energy between 18 and 70 keV.

Kirkpatrick-Baez mirrors are X-ray focusing systems consisting of two total reflection elliptical mirrors, aligned along two perpendicular axes. Their working principle is based on the fact that if a light source is placed at one focus of an elliptic mirror, all light rays on the plane of the ellipse are reflected to the second focus (Figure 3.5.1). This focusing optical system is considered promising due to its potential to remarkably improve the performance characteristics of X-ray microscopy by enabling more efficient collecting of X-rays than in other methods. A further advantage is that the method maintains the focusing state with the same optical arrangement even if the wavelength of the X-rays is shifted. However, to get X-ray beams with an ideal focal size, high efficiency and absence of background noise around a main peak, it is necessary to prepare elliptical mirrors having a very high degree of figure accuracy (approximately 2 nm peak-to-valley figure accuracy) and surface smoothness (approximately 0.2 nm RMS) over an entire reflective area, and position the two mirrors accurately [23]. The KB system is used in conjunction with the primary monochromator in OH1. It suffers from slow thermal drifts, so a software feedback is used to keep them stable. The tank containing the mirrors is thermally isolated from the rest of the hutch in order to make it considerably less sensitive to the day/night thermal cycle. During tests the KB system at ID11 could be used to produce a focus which was entirely stable and a beam position which drifts by less than 5 μm.

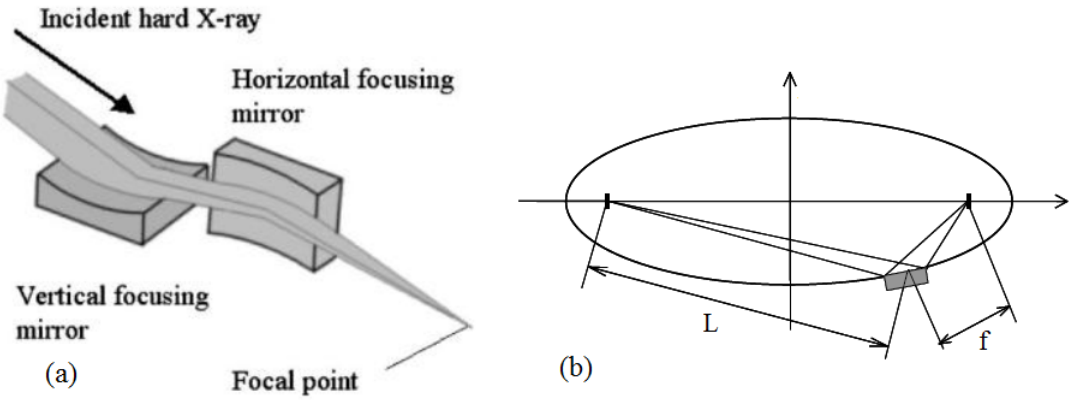

Figure 3.5.1: Kirkpatrick-Baez optics schematic and working principle. (a) It consists of two elliptical mirrors aligned perpendicularly to each other. (b) X-rays from a light source placed at one focus are reflected on the mirror surface and always reach the second focus. [23]

Also, for high-energy nano-focusing applications, two sets of nano-lenses are available: *small radius lenses* and *compound refractive lens CRL chips*. They must be mounted on the same stage as the diffractometer so that the optics and the sample vibrate in tandem. The latter are in-line optical focusing devices that do not deviate the incoming beam path but effectively act as slits, leading to an inherent stability against vibrations in comparison to any other diffracting or reflecting optics.

3.6 Second Experimental Hutch (EH3)

EH3 is the endstation of ID11, dedicated for micro- and nano-focusing applications for diffraction and microscopy experiments in solid state chemistry, physics and materials science. Situated 94 m from the source, this station was built to carry out experiments with ~ 1 μm spatial resolution. EH3 has its own dedicated optical systems (OH2) offering a range of focusing methods. The diffractometer has movement in x, y, z, θ, and ω and a sample stage with movement in x, y, z, rx, and ry and a variety of permanently mounted detector systems are on it, in order to allow the rapid switching between different experimental configurations, as well as simultaneous use of some detectors. The available detectors are:

- Near field FReLoN camera (white beam detector);
- Near field FReLoN camera with lenses;
- 3D Detector;

- Far field FReLoN camera;
- Sensicam;
- Fluoresence detector.

This hutch was originally constructed in a collaborative project with the Synchrotron Working Group, at Risø National Laboratory (Roskilde, Denmark), in order to make three-dimensionally resolved measurements examining strain and texture. These measurements are possible during *in-situ* experiments on thermally or mechanically loaded samples as well as strain analysis with sub-micron resolution near surfaces and grain boundaries.

Behind EH3 there are two laboratories belonging to ID11 and containing an optical microscope, a furnace and various supplies.

3.7 Experimental techniques

ID11 is a truly multidisciplinary beamline, offering a range of diffraction techniques (from high speed 1D point scans to 3D crystallographic reconstructions) whilst working with a wide variety of materials (from nano-crystalline glasses to metal samples). The following is an outline of the main techniques performed at ID11. Particular relevance is given to the description of Diffraction Contrast Tomography (DCT), since it is the technique the present work is concerned with.

3.7.1 Crystallography

ID11 has a strong program of experiments using the "traditional" diffraction methods such as single crystal, powder diffraction techniques, and time resolved studies. Because of the large extent of the topics, the reader is referred to the dedicated literature, such as [1] and [24].

3.7.2 Pair Distribution Function (PDF) analysis

The *Pair Distribution Function* (PDF) analysis is a principally well understood method that was already described in the classical textbook of Warren on X-ray diffraction [25]. It describes a probability of finding any two atoms at given inter-atomic distances (Figure 3.7.1). The primary application of PDF was the study of materials that do not show a long-range lattice periodicity, i.e. liquids or glasses. Their PDFs

show broad features and do not extend over the short-range of the first few coordination spheres. On the other hand, a PDF from a crystalline material is much more structured and gives information on a medium-range of inter-atomic distances.

The PDF is calculated from the Bragg as well as from the diffuse scattering intensities. Therefore, a PDF can discriminate between short-range order (represented by finite non-random displacements from the ideal crystal structure and contributing to the diffuse scattering) and random (thermal) displacements of atoms. Specifically, the experimental PDF $g(\mathbf{r})$ is directly obtained from the diffraction data by Fourier transforming the normalized total structure factor $S(Q)$, with $Q = 4\pi\,(sin\,\theta)/\lambda$. $S(Q)$ is the measured intensity corrected for background, Compton and multiple scattering, absorption, geometric and other factors.

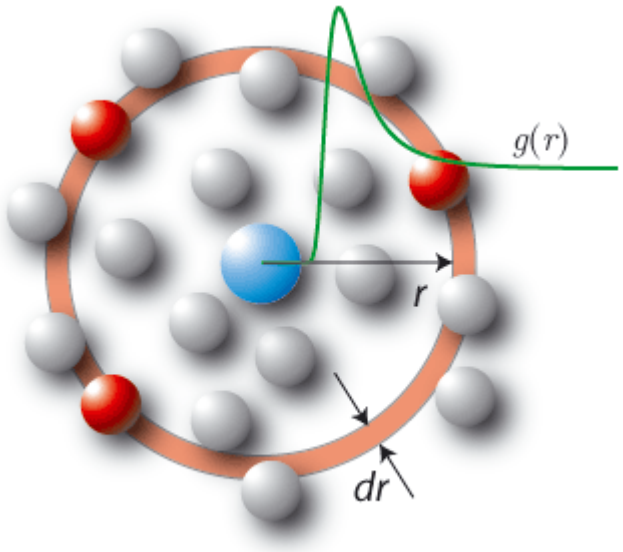

Figure 3.7.1: Illustration of the pair correlation function $g(\mathbf{r})$ for a set of atoms. [26]

3.7.3 3DXRD

Three-dimensional X-ray diffraction (3DXRD) *microscopy* regroups several variants of the monochromatic beam rotation methodology. One may distinguish three different modes of operation: (1) grain center mapping, (2) volumetric mapping, and (3) reciprocal space mapping. The common emphasis and development goals are on fast mapping (providing orientation, shape and elastic tensors) of monophase materials with grain sizes from several μm up to hundreds of μm during mechanical deformation or annealing. In grain center or reciprocal space mapping modes, 3D samples or grain volumes are illuminated by an extended beam and the diffraction patterns are

acquired on a low resolution diffraction detector positioned at intermediate distances (100-200 mm) or large distances (several meters), respectively. In the first case, one may determine the center of mass position as well as average values for the grain orientation and the full elastic strain tensor from analysis of several tens of diffraction spots recorded from the same grain at different sample rotation position. In the second case, the acquisition of far-field diffraction patterns from an individual reflection allows to observe changes in the orientation and elastic strain distribution inside the grain during plastic deformation. However, the features observed in reciprocal space can so far not be associated with a real-space location inside the grain.

The highest level of detail (3D grain shape, local orientation and average elastic strain tensors) is obtained in volumetric mapping mode, where diffraction spots are recorded on a high resolution detector system, which spatially resolves the shape and intensity distribution inside the diffraction spots. Line beam illumination and the use of tomographic reconstruction algorithms applied to spatially resolved diffraction images eliminate the need for scanning the sample in the direction perpendicular to the rotation axis and result in a considerable speed up of the acquisition procedure compared to the point by point scanning procedure employed in polychromatic microdiffraction. Typical acquisition time for a single slice are of the order of a few minutes and 3D sample volumes can be characterized by stacking individual slices. Figure 3.7.2 shows the acquisition geometry used in high resolution grain mapping mode. In order to determine the direction of the diffracted beams, one may either apply ray tracing techniques to near-field diffraction patterns measured at different distances or record the corresponding diffraction patterns on a low resolution diffraction detector placed at larger distances. In practice, images at different distances can now be simultaneously acquired with a new 3D detector system, featuring two high resolution screens in proximity of the sample and a low resolution detector at larger distances. Therefore, the images on the three screens can be acquired simultaneously.

Compared to polychromatic microdiffraction, the 3DXRD methodology allows for faster measurements at the expense of spatial resolution. The improved time resolution may be understood by the change from point (0D) to line (1D) beam illumination mode, which eliminates the need for scanning one of the spatial dimensions. Moreover, the use of advanced tomographic reconstruction methods allows for accurate reconstruction from a limited number of projections. On the other hand, current X-ray imaging detector technology limits the spatial resolution of 3DXRD grain mapping experiments to typical values of about 2-5 μm. The interested reader is referred to the dedicated manuscript by H. F. Poulsen [27] for a thorough treatment of the subject.

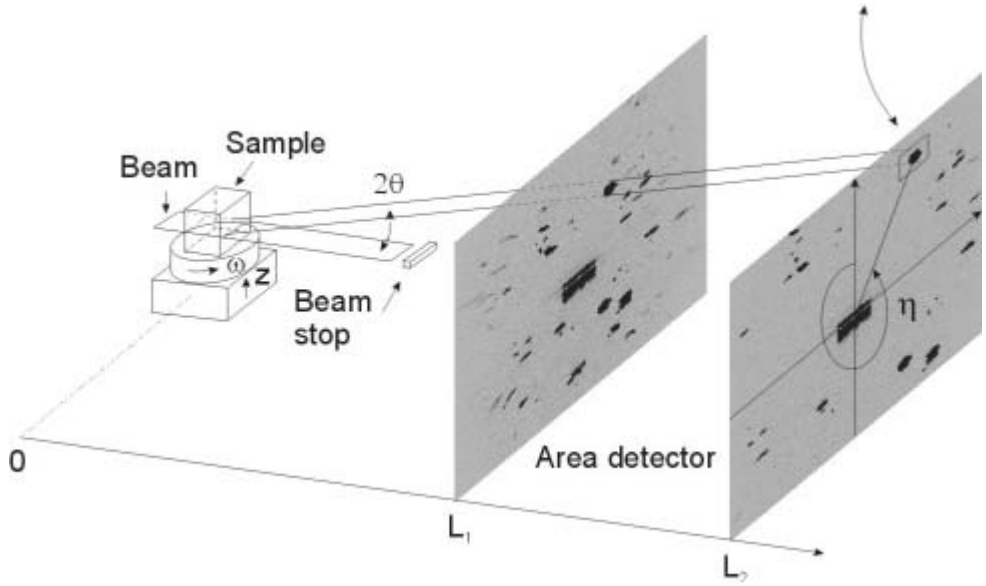

Figure 3.7.2: 3DXRD acquisition geometry. [27]

3D grain mapping techniques would also strongly benefit from the association of 3D imaging modes on the same instrument. The imaging mode is in fact essential for various aspects of microstructure characterization. For instance, it gives access to the shape and spatial arrangements of precipitates, allows for detection of slip bands, porosities, cracks and other features, which can hardly be recognized by diffraction techniques only. Moreover, most imaging modes offer potential for *in-situ* characterization during dynamic experiments (plastic deformation, annealing, fatigue, etc...). In the following sections of this chapter, two such experimental configurations (the so-called *combined methods*), both of which are performed at ID11, are discussed.

3.7.4 Topotomography

Topotomography combines the concepts of X-ray diffraction topography with X-ray absorption tomography and enables three-dimensional characterization of crystals, using two complementary contrast mechanisms. The key idea consists of the alignment of a reciprocal lattice vector of a grain of interest parallel with the tomographic rotation axis (Figure 3.7.3c, tilts T1 and T2). By inclining the rotation axis by the Bragg angle θ (tilt T0) and by performing a small rocking scan over the width of the reflection curve one can record an integrated, monochromatic beam projection of the grain. In the absence of significant orientation gradients, the projection topograph can be approximated to a parallel projection of the grain. Given the alignment of the diffraction vector, the grain stays in diffraction condition during rotation and one may

acquire a large number of projections, regularly distributed over the 360° ω rotation range (Figure 3.7.3a).

By placing the detector in proximity of the sample, both the direct and diffracted beams can be recorded simultaneously using a high resolution imaging detector. Acquiring a large number of projections and adjusting the detector resolution to the size of the grain of interest, one obtains high spatial resolution reconstructions of individual grains within polycrystalline microstructures.

The 3D grain reconstruction can be performed from both the diffracted and the direct beam. In the latter case the projections do not suffer from geometric distortions caused by orientation contrast and the simultaneous absorption (or phase contrast) imaging (Figure 3.7.3b) provides complementary information.

This acquisition geometry was used to analyze the shape evolution of individual grains during the recrystallization process in deformed aluminum single crystals. Results are available at reference [28].

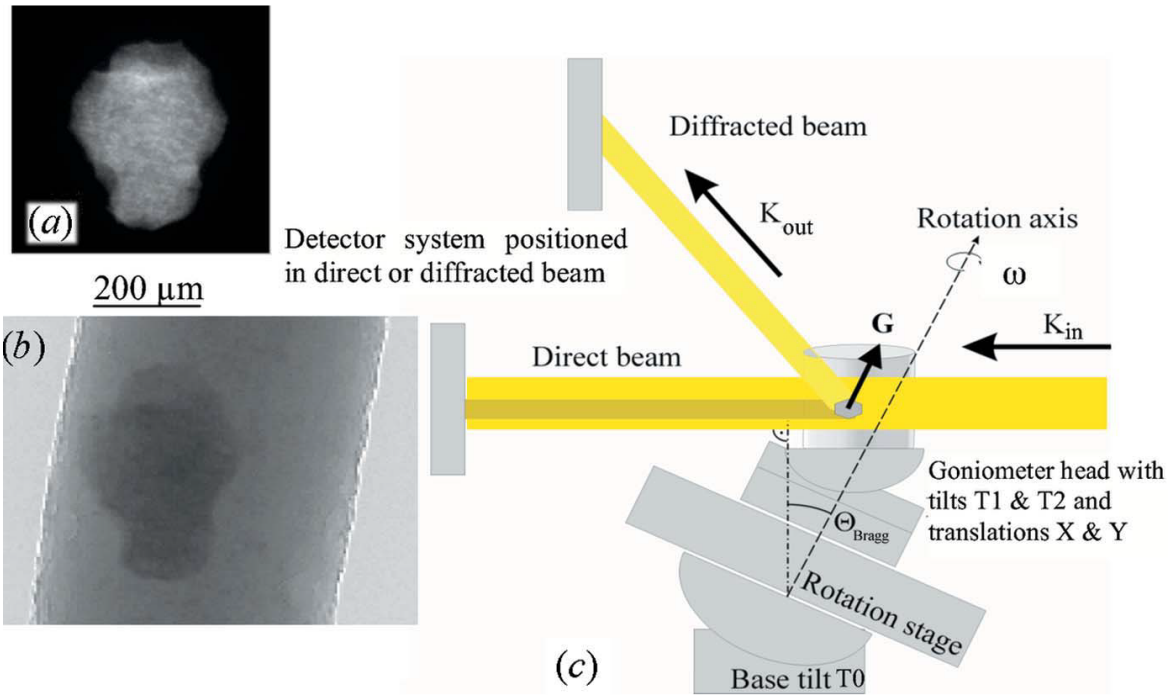

Figure 3.7.3: Principles and results of topotomography. (a) Integrated, monochromatic beam X-ray projection topograph of the (220) reflection from an Al grain inside a polycrystalline sample. (b) Corresponding absorption image showing the cylindrical sample outline and the extinction spot of the diffracting grain. (c) Experimental setup. [29]

3.7.5 Diffraction Contrast Tomography

The term *diffraction contrast tomography* (DCT) refers to different variants of 3D polycrystal characterization techniques capable of mapping 3D grain shapes and orientations in sample volumes containing up to thousand grains or more. A common feature of the different approaches is the combination of absorption and diffraction imaging modes on the same instrument.

As in conventional absorption tomography, the rotation axis is set perpendicular to the beam and the individual grains in the illuminated sample volume will fulfill the Bragg condition (equation 2.1.2) for different reflections only at a subset of rotation angles, dictated by the grain orientation. Two variants of DCT used to exist: the direct beam case and the combined case. The former exploited the extinction contrast, occasionally observed in the transmission images of undeformed, polycrystalline specimens. The latter used the information in diffraction spots as well as in extinction images.

However, such distinction is nowadays obsolete. In this framework, the introduction of the Friedel pair concept, the adaptation of a general purpose, oblique angle, 3D algebraic reconstruction algorithm and the improvement of the polycrystal indexing procedure (master thesis by P. Reischig, section 4.6) resulted in a variant of DCT which is typically based only on the use of diffraction spots.

3.7.5.1 Direct beam case

From an experimental point of view, the direct beam variant of DCT is very similar to conventional absorption contrast tomography. The sample is illuminated by a monochromatic beam with narrow bandwidth ($\Delta\lambda/\lambda \simeq 10^{-3} \div 10^{-4}$). Several thousand projection images are recorded during continuous rotation of the sample over 180° (Figure 3.7.4). During rotation, individual grains will occasionally pass through Bragg diffraction alignments. Reflections with a high structure factor (typically those with low Miller indices) diffract a significant fraction of photons out of the direct beam. These diffraction events can therefore be observed as dark extinction spots (missing intensity) in the direct beam. The Bragg diffraction event may indeed be considered as an additional contribution to the local attenuation coefficient μ of the material (see section 4.2).

Unlike the case of topotomography where the extinction contrast of a selected grain is visible in all the projection images and so no specific image treatment is required to separate diffraction and absorption contrasts, the analysis of DCT data involves the segmentation and classification of the extinction spots, which now can

arise from any of the grains in the illuminated sample volume.

In the case of multicrystals, the classification of extinction spots into sets belonging to the same grain can be entirely based on two spatial criteria. First, the projected vertical size and position of extinction spots is constant during rotation of the sample around an axis perpendicular to the beam; second, the center of mass position of the spots must follow a sinusoidal trajectory.

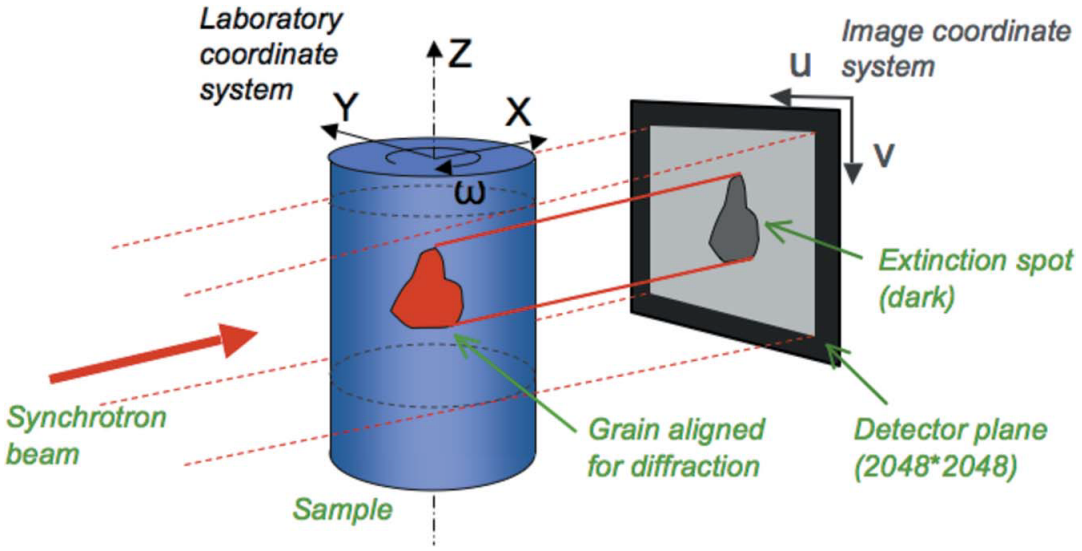

Figure 3.7.4: The acquisition geometry used for the direct beam variant of DCT. [30]

Compared to other grain mapping techniques, the direct beam variant of DCT has a number of advantages:

1. Absence of geometrical distortion of the extinction spots due to the parallel projection geometry;

2. Possibility to adjust the pixel size in order to match the sample size, thus resulting in an enhanced resolution;

3. The conventional flat-field correction procedure (see section 4.3) can be applied to account for non-uniform illumination and spatial variations in the response of the detector system;

4. No constraints on the distance between sample and detector, so that even bulky sample environments can be used. Then, the spatial coherence of third generation synchrotron beams allow direct combination with propagation based phase contrast tomography;

5. Possible combination with X-ray microscopy for further improvement of the spatial resolution.

In kinematical diffraction theory, the visibility of the extinction contrasts is directly proportional to the grain thickness and inversely proportional to the widths of the crystal reflection curves. Imaging conditions can be optimized by adjusting the angular integration range to the typical width of the reflection curves. Sample rotations over a range comparable to the width of the crystal reflection curve will yield strong contrast, whereas a broadband illumination or too large rotation intervals will reduce the contrast of the extinction signal. For crystals with large orientation spreads the contrast will always be poor.

As a result, the direct beam methodology is limited to the case of multi-crystalline samples made of materials exhibiting a low intra-granular orientation spread ($\lesssim 0.2°$) with no more than about 5 grains in the through thickness dimension of the illuminated sample volume. Increasing the number of grains and/or the intra-granular orientation spread quickly leads to a situation where extinction spots from different grains overlap and automatic segmentation procedures fail to extract the accurate spot outlines.

In order to alleviate this problem, the combined case acquisition geometry has been designed.

3.7.5.2 Combined case and the latest variant

In order to capture both extinction and diffraction spots on the same detector, one has to accept a compromise in spatial resolution: with the same number of pixels given by the CCD camera ($2k \times 2k$) an area three to five times larger than the lateral dimension of the illuminated sample volume has to be covered (Figure 3.7.5).

By matching diffraction spots with corresponding extinction contrasts in the direct beam, the combined method allowed polycrystalline samples with more than hundred grains per cross-section to be addressed. However, the analysis route used in the current implementation of DCT has to certain extent merged with the concepts of 3DXRD in the sense that diffraction instead of extinction spots are used for 3D grain shape reconstruction, based on oblique, algebraic reconstruction algorithms.

Though, there are a number of improvements compared to the initial 3DXRD methodology, the most relevant of which relies on the acquisition of Friedel pairs and will be now discussed.

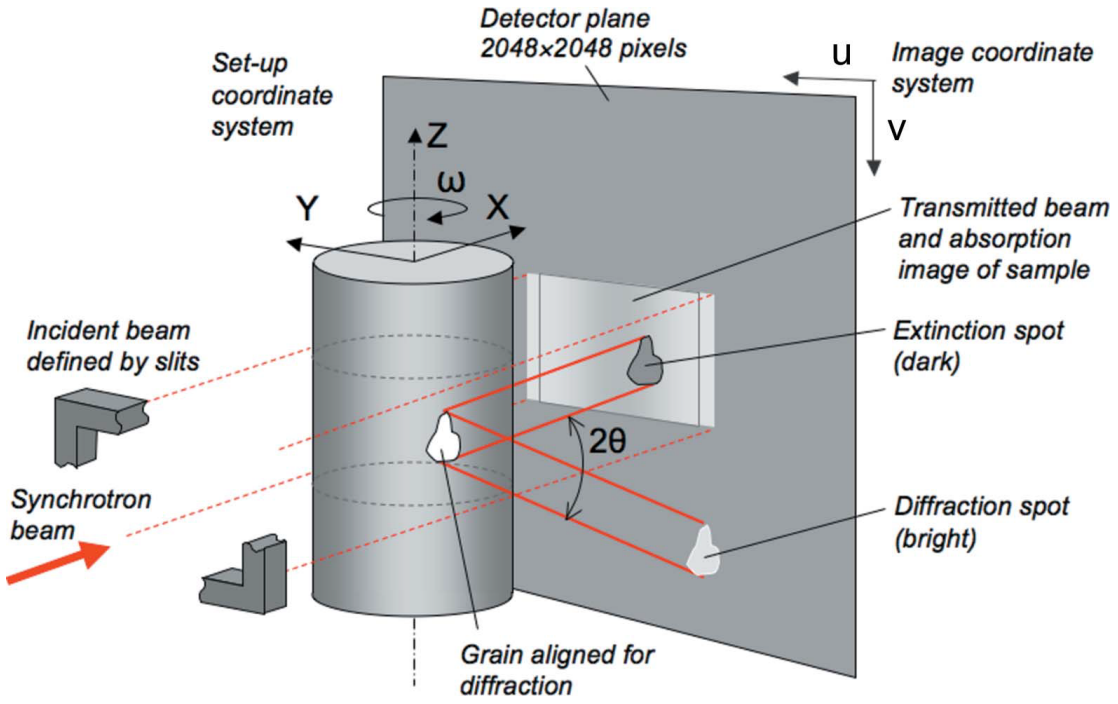

Figure 3.7.5: The acquisition geometry used for the combined case variant of DCT. [31]

The extension of the scanning range from 180° to 360° offers a very precise and unambiguous way to determine the diffraction angles (the rotation angle ω, the azimutal angle of spots on the detector η and the Bragg angle θ) by exploiting the symmetry of Friedel pairs (also known as Bijovet pairs). During a rotation of the sample, the angle between a given crystal plane of a grain and the incident beam varies sinusoidally between zero and some maximum value. In a full 360° rotation this angle coincides with the Bragg angle a maximum of four times, provided that the angle between the rotation axis and the plane normal is bigger than the Bragg angle. Thus, each set of lattice planes can give rise to a maximum of four diffraction spots, which make up two pairs, each separated by a 180° rotation of the sample. Such pairs are called Friedel pairs and they are the Bragg reflections from (hkl) and $\overline{(hkl)}$ lattice planes of the grain. Relative to the sample, the pairs of scattering vectors and the associated diffracted beams are parallel but opposite in sign. As illustrated in Figure 3.7.6, a 180° rotation of a scattering grain around an axis perpendicular to the beam will bring a set of diffracting planes (hkl) into Bragg condition for $\overline{(hkl)}$ reflection. The 180° rotation in the laboratory system is equivalent, in the grain reference system, to a reversal of the direction of the incoming beam and of the position of the detector. The superposition of the image acquired at $\omega = \omega_0$ and the image at $\omega = \omega_0 + 180°$,

flipped around the projected rotation axis, reveals that the extinction spot is located on the line connecting the two corresponding Friedel pair spots (Figure 3.7.7).

The three diffraction angles (ω, η, θ) are determined from the center of mass positions of the pair spots. This eliminates any dependencies on the location of the grain inside the sample. In the absence of orientation and strain gradients, the two diffraction spots forming a pair are symmetric, i.e. they are mirror images, thus facilitating an authomatized recognition of the pair spot in the 180° offset image. Using a combination of search criteria (shape, size, intensity, ω spread and position) a robust search algorithm has been implemented by P. Reischig. Details about the data processing routine are outlined in the following chapter.

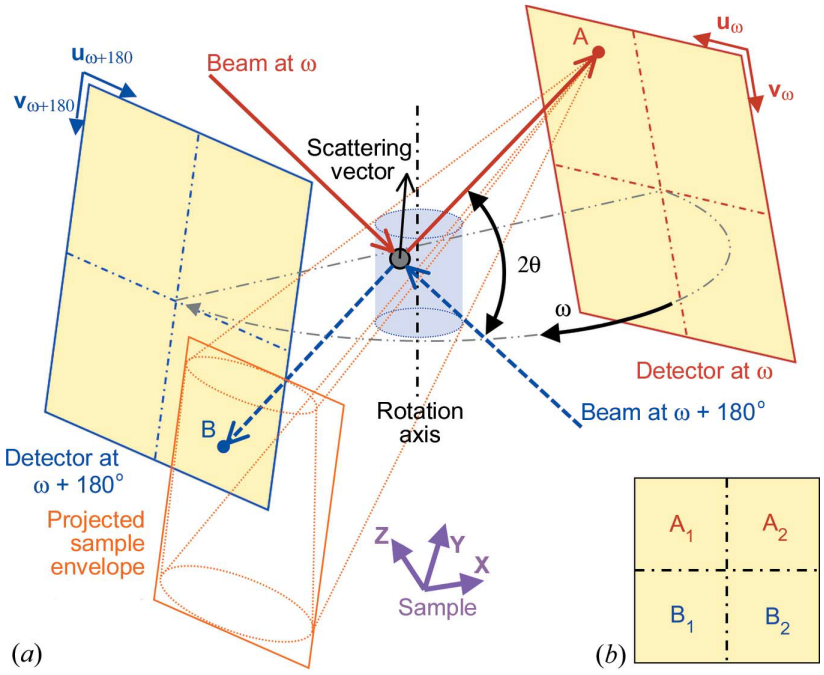

Figure 3.7.6: (a) Geometry of Friedel pairs in an arbitrary detector position. A Friedel pair A-B is illustrated in the reference frame fixed to the sample. The incident beam and the detector are shown 180° offset in ω. The two diffracted beam paths are coincident and connect A with B through the grain. The diffraction angles can be calculated directly without precise knowledge about the grain position. B falls inside the projection of the sample envelope from A onto the detector in the opposite position. (b) Relative positions of the four diffraction spots from an (hkl) crystallographic plane of a grain on the detector. The two Friedel pairs are A1–B1 and A2–B2. [32]

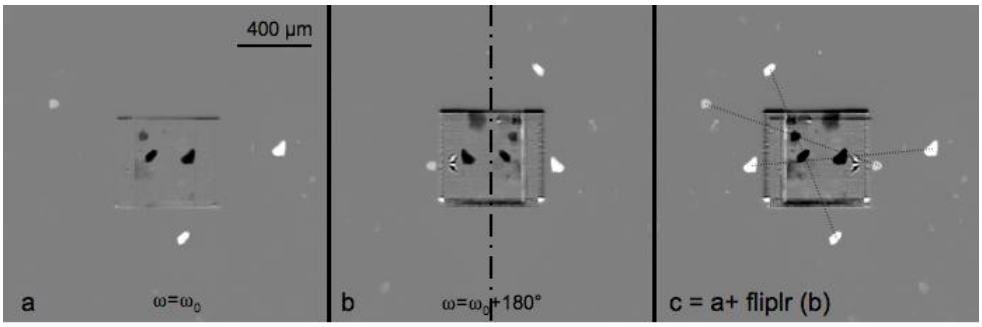

Figure 3.7.7: (a) Background corrected diffraction image with three strong extinction - diffraction spot pairs visible. (b) Corresponding image after 180° rotation of the sample. (c) Sum of images (a) and (b), flipped around the vertical axis. The lines connecting Friedel pairs of diffraction spots run through the extinction spot of the corresponding grains. [33]

The Friedel pair concept brings several advantages compared to the acquisition of diffraction images at multiple sample to detector distances typical in 3DXRD acquisition geometry:

• The line connecting the pair spots precisely determines the direction of the diffracted beam in the laboratory system and is independent of the position of the grain with respect to the axis of rotation. This yields a precision comparable to the one obtained by measuring a single reflection on a diffraction detector, typically featuring 10 times bigger pixel sizes and positioned at larger distances;

• The use of the summed spot pair reduces the asymmetric distortion of the individual spots in the presence of orientation or strain gradients within the grain. This improves the accuracy of the reconstruction;

• The Friedel pair uses effectively twice the distance between the rotation axis and the detector, thus providing a factor of 2 improvement in the determination of diffraction angles for any detector configuration (near field imaging detector or far field diffraction detector);

• When combined with the extinction spot matching, the grain center of mass position can be identified from acquisition of a single spot pair, without the need for indexing an entire polycrystal data set. This provides a fast and simple means for the determination of the position of the grain giving rise to a reflection on the detector.

On the other hand, the acquisition of Friedel pairs is based on a full 360° rotation of the sample, a requirement conflicting with some types of sample environment (i.e. furnaces) and involving twice as long as acquisition times.

DCT scans in combined case also result in more than one order of magnitude re-

duction in scanning times compared to line beam acquisition procedures. Moreover, it ensures isotropic resolution in the reconstructed grain maps and alleviates problems associated to sample drift during measurements. The acquisition of the transmitted beam in the center of the detector enables the reconstruction of the sample microstructure visible in conventional absorption tomographic mode. Absorption (or phase contrast) tomograms can be used, for example, to infer and correct for sample drifts occurring during acquisition of the DCT scan or, in the case of two-phase materials, to determine the location of interphase boundaries. Last but not least, they can reveal the presence of inclusions of material defects (porosities, cracks), thus providing information which can be used in studies of material damage.

Chapter 4

DATA ANALYSIS PROCEDURE

In this chapter the basic assumptions enabling direct interpretation of the diffraction contrast in terms of grain projections are outlined and the principal steps of the current data analysis procedure are explained in more detail.

4.1 *Diffraction Contrast Tomography* (DCT) code

The DCT code for analysis procedure is only usable on the *NICE* computer cluster at ESRF, so users must access ESRF network first, either through *NX Client* or *SSH* protocol. The whole code can be downloaded at the following link:

http://sourceforge.net/projects/dct/files ,

where instructions for the installation are found as well.

The entire process of DCT analysis is carried out by user functions, which have to be run in a specific order. Processing of DCT type experimental data still requires a significant amount of monitoring and user interaction owing to the vast variety of sample and experimental conditions. However, the interactive stages of DCT processing route have been greatly improved by reduced processing times and the addition of graphical user interfaces (GUIs).

4.2 Basic assumptions

As previously discussed, samples are assumed to be composed of very small mosaic blocks, so that each individual diffraction event, from whatever locality within the crystal, acts independently of the others. Effects from dynamical theory of diffraction

are thus neglected and one can use the Lambert-Beer law (equation 2.3.2) to describe the intensity decay of X-ray radiation when passing through a diffracting grain:

$$I(u,\, v) \,=\, I_0(u,\, v)\, exp\left[-\int \mu_{eff}(\mathbf{r})\, dx\right]$$

In this equation:

- $(u,\, v)$ are the coordinates on the detector;
- $\mathbf{r} \,=\, (x,\, y,\, z)$ defines the position inside the sample, the integral being calculated along the beam direction x. The integration along straight lines also implies that local variations of the X-ray refractive index decrement inside the sample δ in equation2.2.1 are neglected;
- $\mu_{eff}(\mathbf{r}) \,=\, \mu_{abs}(\mathbf{r}) \,+\, \mu_{diffr}(\mathbf{r})$ is an *effective attenuation coefficient*. $\mu_{abs}(\mathbf{r})$ comprises all physical phenomena contributing to X-ray attenuation other than coherent scattering from portions of crystal grains aligned for Bragg diffraction. $\mu_{diffr}(\mathbf{r},\, \lambda,\, \varphi,\, F_{hkl},\, L)$ also depends on the wavelength λ, the local misorientation $\varphi(\mathbf{r})$ with respect to the maximum of a given (hkl) reflection, and the corresponding structure factor F_{hkl} and Lorentz factor L. $\mu_{diffr}(\mathbf{r},\, \lambda,\, \varphi,\, F_{hkl},\, L)$ is also supposed to factorize in two terms $\mu_{diffr}(\mathbf{r})$ and $m(\lambda,\, \omega,\, \mathbf{g})$ after integration over local misorientation ranges φ. The spatially varying part $\mu_{diffr}(\mathbf{r})$ expresses local variations of the diffracted intensity arising from spatial variations of the sample density (because of defects and/or phase inclusions) and is independent of the actual orientation of the crystal with respect to the incident beam. The scaling function $m(\lambda,\, \omega,\, \mathbf{g})$, where g represents the orientation matrix of the grain, is nonzero only for particular rotation angles ω, each time a reflection fulfills the Bragg condition. A relevant result of kinematical diffraction theory is that $m \,\propto\, |F_{hkl}|^2\, L$ (a thorough treatment can be found in [1]).

4.3 Preprocessing of the image stack

In the first step some background removal and normalization operations are applied to the raw images containing contributions from both the absorption and the diffraction contrasts: $\mu_{eff}(\mathbf{r}) \,=\, \mu_{abs}(\mathbf{r}) \,+\, \mu_{diffr}(\mathbf{r})$.

1. As a first thing, in order to take into account the effects of optics systems and acquisition camera, a distortion correction is performed using a distortion map based on the radiograph of a regular absorption grid. Then, the footprint of

the direct beam and the boundaries of the diffracted beam area of the images are determined. It is worth noting that the image formed by the direct beam illuminating the detector is treated *separately* from the one formed outside the direct beam.

2. A common flat-field correction of the direct beam image in raw projections is applied:

$$I_{tot}^{\omega} = \frac{image^{\omega} - dark}{reference - dark}$$

where

$$I_{tot}^{\omega} \propto exp\left\{ - \int \left[\mu_{abs}(\mathbf{r}) + \mu_{diffr}(\mathbf{r}) \right] dx \right\}$$

3. Since the angular interval over which diffraction from different reflections significantly contributes to the effective attenuation coefficient are negligible compared to the rotation range of a tomographic scan (180° or 360°), one can neglect μ_{diffr} and evaluate only μ_{abs} by means of a conventional *filtered back-projection* tomographic reconstruction algorithm or a three-dimensional *simultaneous iterative reconstruction technique* (SIRT) algorithm. The three-dimensional absorption microstructure from direct beam projection images $-ln\left(I_{tot}^{\omega}\right)$ is obtained.

4. An absorption background of direct beam images is calculated as a one-dimensional median through a stack of images centered around a current image and extending, equally spaced, over a certain angular range (Figure 4.3.1). By calculating the one-dimensional pixel-wise median value along the stack dimension, one can efficiently reject diffraction events and obtain a good estimate of the slowly varying absorption background:

$$I_{abs}^{\omega} \simeq Median_{\omega} \left\{ I_{tot}^{\omega - n}, I_{tot}^{\omega - n + 1}, ..., I_{tot}^{\omega}, ..., I_{tot}^{\omega + n} \right\}$$

$$I_{abs}^{\omega} \propto exp\left[- \int \mu_{abs}(\mathbf{r})\, dx \right]$$

This again is a consequence of the fact that contributes from diffraction do not survive over long ω-ranges.

5. The absorption background is removed by logaritmic subtraction and diffraction contrast projections P_{diffr}^{ω} are obtained:

$$P^{\omega}_{diffr} \;=\; -\,ln\,(I^{\omega}_{tot}\,/\,I^{\omega}_{abs}) \;=\; \int \mu_{diffr}(\mathbf{r})\,dx$$

6. Background intensity is calculated and removed outside the direct beam in the same way as in steps number 4 and 5.

7. Finally, intensities in the direct beam and non-direct beam areas are normalized before forming the composite image.

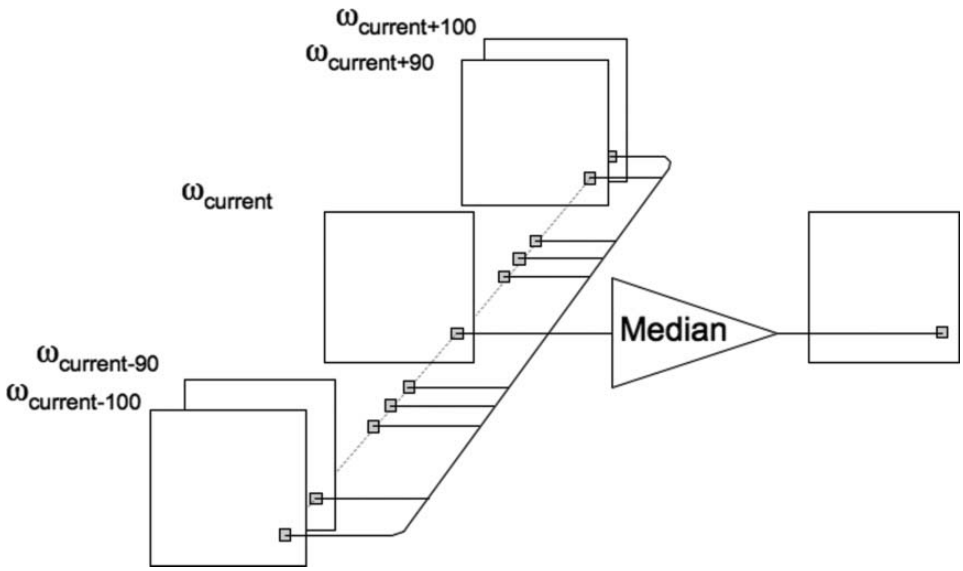

Figure 4.3.1: Calculation of the median filter for a stack of 201 images arranged by angle. [31]

4.4 Segmentation of the diffraction spots

Segmentation is the processing step in which diffraction blobs are separated from the preprocessed images. We use the term *blob* to refer to a *3D entity* with intensity extending in the plane of the detector (u, v) and in the stack of images ω. These 3D regions are eventually summed in the stack direction to create a *2D diffraction spot*.

Segmentation can be performed in two different ways. The first one is by setting a single threshold at the background noise level, such that areas above this threshold are segmented as diffraction spots. The second one, which is usually preferred, is by setting a double threshold such that possible peaks are identified with an intensity threshold, and the second threshold, which is linearly proportional to the given peak intensity, is used for determining the outlines for the spots.

The principle of the algorithm is to work in two phases. The first phase is the seed segmentation. This works in 2D, one image at a time. The image is thresholded with a simple single threshold. This identifies bright regions in the image. The single brightest pixel within each region is a *seed* and its position and intensity is recorded in a database table. These seeds are points from which blobs can be grown. Thus, each blob is grown from a seed; however, not every seed becomes a blob. The second phase is to grow blobs from seeds. Seeds are treated in descending order of intensity, so the brightest seeds are treated first. A region around the seed point is selected. A threshold value is calculated from the seed intensity, and applied to the region. Those voxels above the threshold, and connected to the seed point, are selected. If the thresholded voxels touch the edge of the region, the region is extended. If the region is found to contain another, brighter seed point, or a seed point which already belongs to a grain, the process is abandoned. If the segmented intensity is entirely contained within the region, without reaching the edges, the segmented voxels are assigned to a diffraction blob and written to the database.

The reason to work in this way is that the threshold used can be adjusted as a function of the brightness of the diffraction spot. This is because the same grain may have diffraction spots that vary in intensity because of the structure factor of the reflection, or absorption in the sample, or the distribution of intensity in the direct beam. It would be desirable to use all of these as projections of the grain. Therefore, they should all be of similar size. This implies that the threshold must vary, otherwise bright spots appear bigger than dim spots. Referring to Figure 4.4.1, which is a screenshot of the used *Segmentation Graphical User Interface*, the following parameters are regarded as the most important to control:

- seed threshold is the first threshold that is applied to the images to identify the seeds;
- thr_grow_ratio is defined such that the threshold used to segment the blob is the seed intensity multiplied by this ratio;
- thr_grow_low and thr_grow_high are upper and lower limits to the threshold value. It is useful to set the former somewhat above the noise floor to stop weak blobs from becoming too large. The latter can be used to control the upper limit of the threshold value. The use of these first parameters is shown in Figure 4.4.2 as well;
- blob min size and blob max size: if a segmented blob is outside of these limits, it is assumed to be bad. It can happen that the background noise, or intensity

around the direct beam, or spot overlap, leads to the blob becoming too big. Alternatively, the blob can be too small to be useful;

- seed minimum area: a seed must have a certain number of pixels to be considered. This is stated in order to remove spikes or hot pixels;
- the segmentation bounding box defines a region around the direct beam where nothing is segmented.

Each diffraction spot is segmented as a connected neighborhood using a three-dimensional morphological reconstruction. Overlapping spots may be segmented as one and will be filtered out in later stages. These diffraction metadata are stored in a database.

The possibility of applying a "soft" thresholding instead of a single one has been recently added: that is, the threshold that determines the background noise level or the minimum value in a blob is subtracted from the entire blob volume. This way, the intensity approaches zero at the edges of the blobs, which results in smoother and physically more consistent grain shapes.

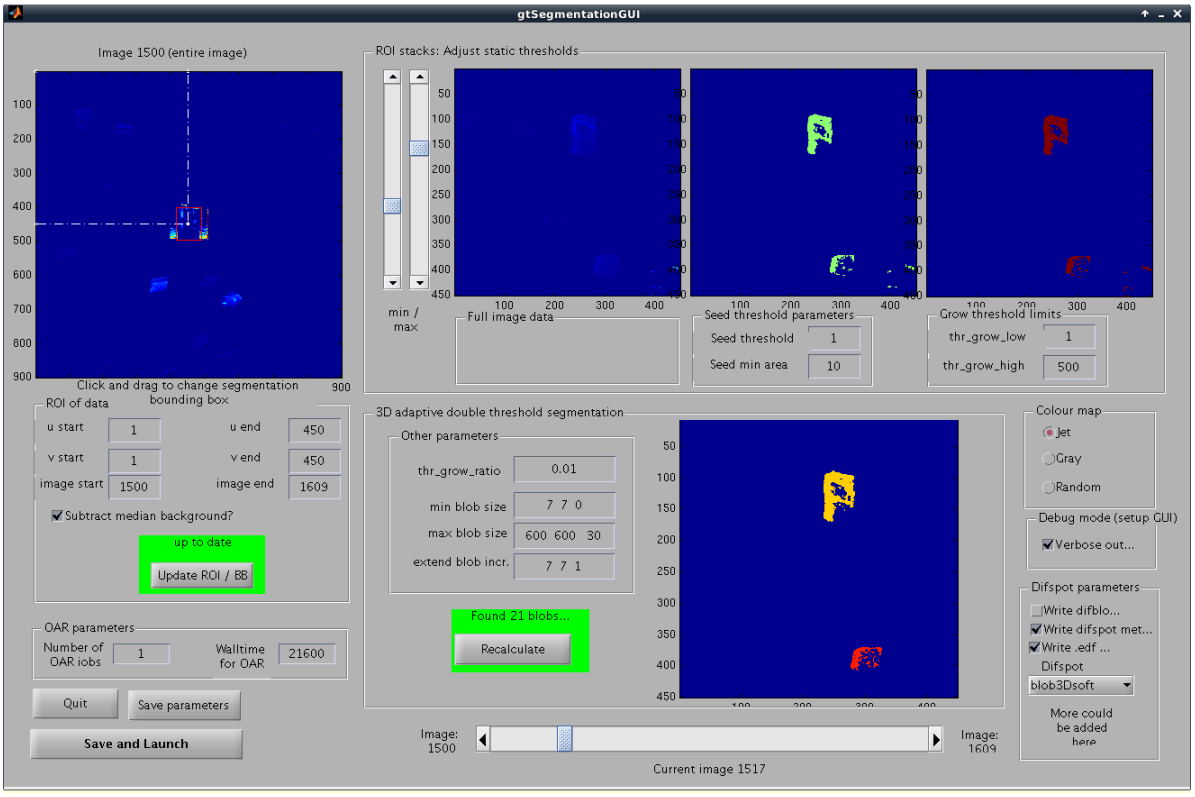

Figure 4.4.1: A screenshot of the Segmentation Graphical User Interface. The meanings of some parameters are outlined in the text.

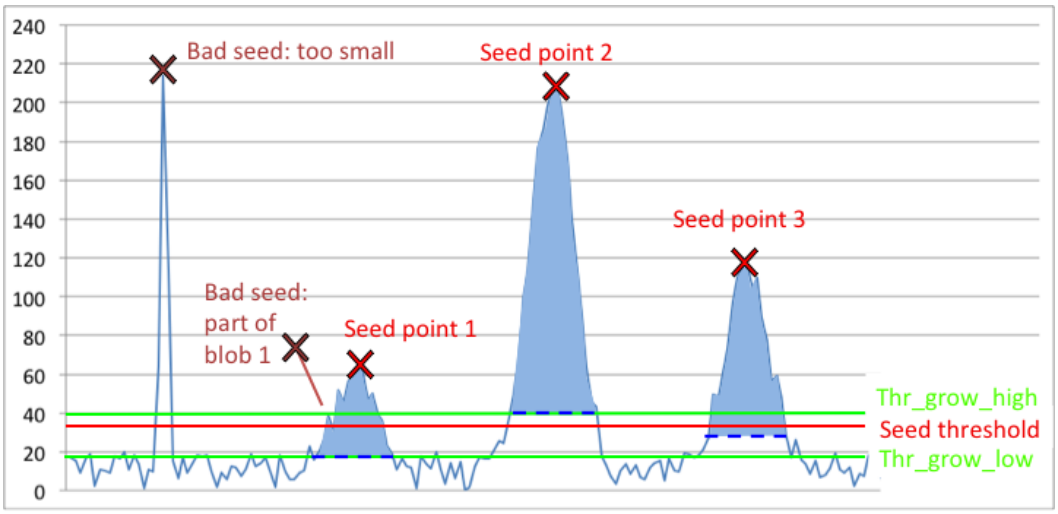

Seed threshold: 40
Growth ratio: 0.25
Thr_grow_low: 18
Thr_grow_high: 40

Seed	Seed value	Value x ratio	Final threshold
1	64	16	18
2	210	52.5	40
3	118	29.5	29.5

Figure 4.4.2: Illustration of some segmentation criteria which are used in the analysis procedure. The vertical axis represents the seed intensities in arbitraty units, while the horizontal axis corresponds to the spread in the number of images (or rotation angle ω).

4.5 Matching of Friedel pairs

The principle behind Friedel pairs has been discussed in the previous chapter. In order to exploit the information they carry, it is necessary to identify the diffraction spot pairs in images separated by 180° rotation.

If the lattice type and lattice parameters of the sample and the wavelength λ of the radiation are known, it is possible to calculate the diffraction angles $\theta_{\{hkl\}}$ through Bragg's law 2.1.2. Using the same sample coordinate system, the diffraction cones with $2\,\theta_{\{hkl\}}$ opening angles corresponding to these angles can be drawn based on the first diffraction spot. These cones intersect the 180° offset detector as circles and the second diffraction spot of the pair must lie on one of these (Figure 4.5.1).

It is also known that the grain must lie in the volume of the sample illuminated by the direct beam. This imposes the further constraint that the second diffraction spot must lie within the region formed by projecting this volume, from the position of the first spot, onto the 180° detector (see Figure 4.5.1 again).

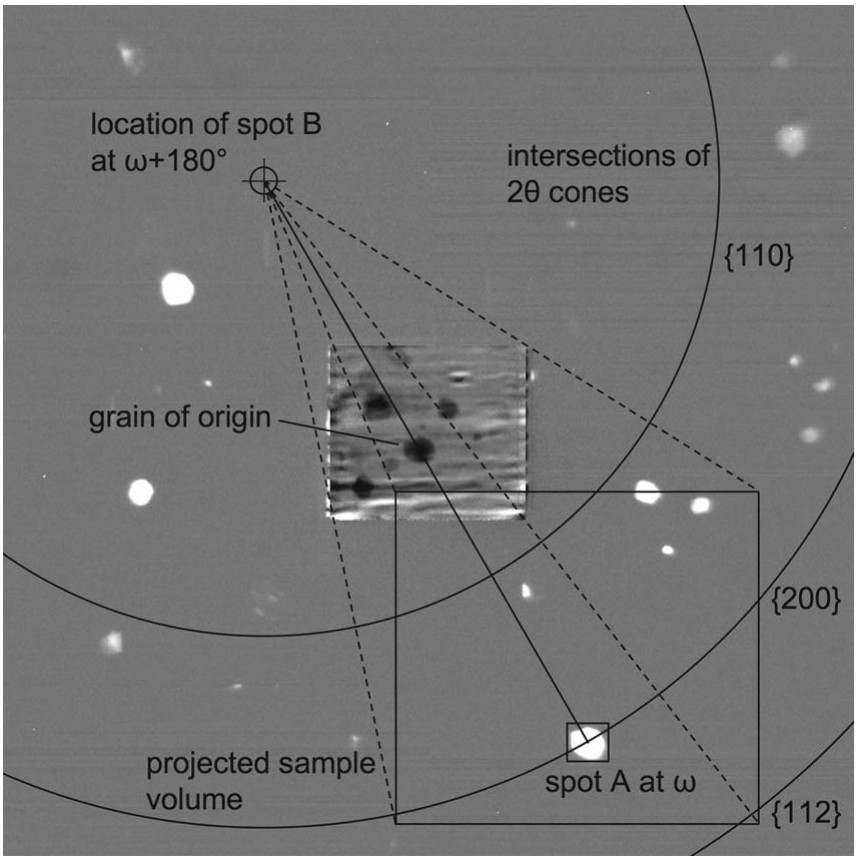

Figure 4.5.1: Spot A, the corresponding pair of spot B, is found in the images at a rotational offset of about 180°. The search area is restricted to the projected sample volume (represented as a square) and to the narrow circular bands along the intersections of the detector plane and cones originating from spot B varying $2\theta_{\{hkl\}}$ opening angles. [34]

The size, shape, and intensity of the paired spots should also be similar. By using these criteria with suitably selected tolerances, pairs of spots can be found reliably. It is not possible to find the pairs of all diffraction spots, because in some cases one of the pair will fall outside the detector area, or may overlap with another diffraction spot or the direct beam. It is not necessary that all the spots are paired, as single diffraction spots can be dealt with in further steps of the analysis procedure. Typically, for a data set comprising of 10^2 - 10^3 grains with cubic symmetry, 10^3 - 10^4 spot pairs are found.

For any Friedel pair the diffracted beam path is obtained as the straight line connecting the two pair spots (Figure 3.7.6). The grain of origin must lie along this line but there is no need to determine the actual grain position at this stage. The direction of the scattering vector can be calculated as the vector difference between the

diffracted and incident beams. The Bragg angle θ and azimuthal angle η are also calculated, as well as the difference from the nearest theoretical $\theta_{\{hkl\}}$ value, average spot size and intensity for the pair. Pair combinations that pass the preset tolerances for deviations in θ, mean ω value, beginning and end of the ω range, bounding box size, intensity, and area are considered in the search. A figure of merit to describe the mean error of a pair ε_{pair} in a single value is calculated as the summed square of those deviations weighted by the squared inverse of its corresponding tolerance limit:

$$\varepsilon_{pair} = \sqrt{\sum_i \left(\frac{relative\ deviation\ (i)}{tolerance\ (i)} \right)^2}$$

The final set of Friedel pairs is selected from all potential pair combinations ranked according to their mean error and includes any diffraction spot maximum once.

Calibration of the exact detector position relative to the beam and the rotation axis is essential to achieve high orientation and three-dimensional shape reconstruction accuracy. While the Debye – Scherrer rings from a powder sample of a standard material can be used to calibrate a far-field detector, this procedure is not suitable for a near-field setup. As the diffraction angles can be computed from the pairs without knowing the grain centroids, the refinement can be performed before the indexing stage. This refinement is applicable with a single-crystal or polycrystal standard that exhibits little or no residual stresses, or can be performed using the actual specimen if its lattice parameters are known. The {hkl} family and the corresponding theoretical lattice spacing yield an X-ray wavelength for any Friedel pair via Bragg's law 2.1.2. A nonlinear least-squares optimization algorithm is applied to minimize a target function – the sum of the squared deviation of the computed X-ray wavelengths from the true value. This implies that the beam energy should be carefully characterized during the experiment, either using an absorption edge or a standard Si crystal. The detector position is refined in the laboratory reference frame, which at the same time defines its position relative to the beam and rotation axis, since these are kept constant and usually are fixed to the laboratory base. The following intuitive parameters are fitted:

- tilt around the u axis;
- tilt around the v axis;
- in-plane tilt;
- angle between the u and v axes;

- mean u and v pixel size;
- pixel size ratio u/v;
- (x, y, z) position of the detector (distance and offset).

From the diffraction geometry, only either the mean pixel size or the rotation axis – detector distance can be fitted at any one time, as they have the inverse effect. The mean pixel size of the detector system is generally known or measured, and the distance is fitted since it is especially difficult to measure precisely for a near-field detector. The detector position in the direction parallel to the rotation axis is a free parameter and cannot be determined from Friedel pairs, as the scattering geometry is unaffected by such a displacement (see Figure 3.7.6). If the geometry is known or has been previously fitted, the crystal lattice parameters for any phase can be fitted with the same optimization procedure. In the case of multiphase materials, the basis of the fitting can be chosen as the phase for which the lattice parameters are known with the smallest uncertainty. It is reasonable to choose a phase with an exact stoichiometric composition or one with a narrow solubility region for alloying elements. Another aspect to be considered is that the number of free lattice parameters should be small (e.g. one for a cubic lattice). The geometry and the lattice parameters of the other phase can then be calibrated according to that basis to result in a consistent measurement.

4.6 Indexing of grains from Friedel pairs

Indexing involves finding grain positions and orientations in the sample by grouping the observed diffraction spots. The effectiveness of indexing algorithms depends on the extent and accuracy of the information on which they primarily rely. For example, far-field data have better orientation accuracy, while near-field data contain more precise spatial and size information about grains.

The updated version of the iterative indexing algorithm manages to find grains using all the available information from each Friedel pair, namely: potential {hkl} families and phases, scattering vector direction, diffracted beam path through the sample volume, average bounding box sizes, intensity, and area of the two diffraction spots. Each phase in a multiphase material is indexed independently, by considering only those Friedel pairs for which the Bragg angle was found to be close enough to one of the given phases in the pair matching stage. This way, the algorithm can account for multiphase materials, as well. A flow-chart of it works is shown in Figure 4.6.1.

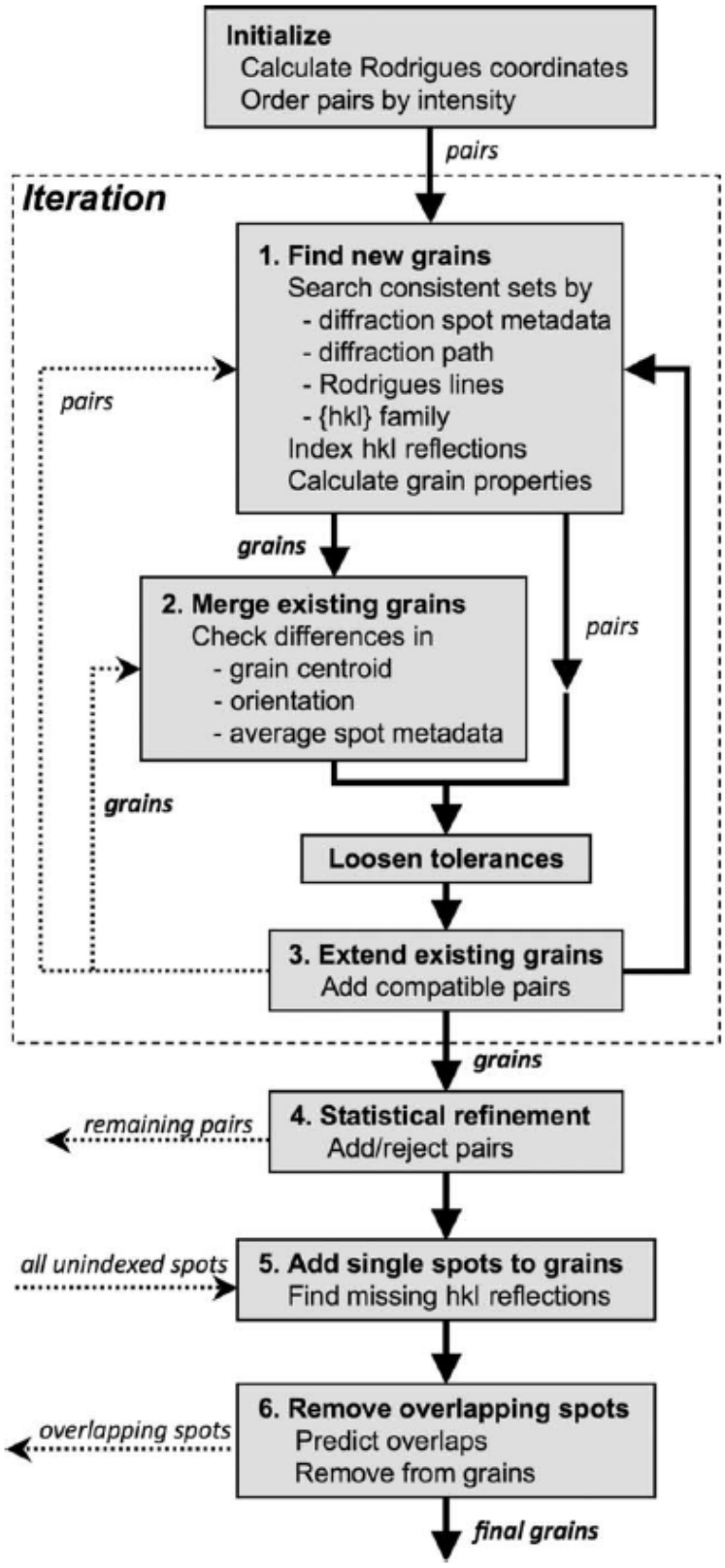

Figure 4.6.1: Flow-chart of the indexing algorithm that is applied to each crystal phase present in the sample. [32]

The core is an iterative search for grains in which tolerances are gradually loosened. This ensures robustness as erroneously segmented diffraction spots or wrong Friedel pair matches, as well as coincident "fake" grains in a large data set containing many spots, are less likely to be indexed. The first iteration loops are expected to index Friedel pairs with the smallest angular and positional error, and the last loops can account for higher errors but in a much reduced set of pairs. The user is allowed to revise and adjust preset tolerances and parameters according to the actual data set by setting values for the first and last iteration loops.

Grain orientations are handled in Rodrigues space. A three-dimensional Rodrigues space provides a mapping of the orientation space where each point uniquely defines a three dimensional rotation. Crystal symmetries are accounted for by restricting this space to the fundamental zones. Therefore, triclinic or monoclinic crystals cannot be directly handled this way, since the Rodrigues space would be infinite. Each potential hkl and $\overline{hkl}$ reflection assigned to a Friedel pair of a given phase represents a line crossing the fundamental zone. Line segments falling outside the fundamental zone correspond to symmetry equivalents and are folded back into this zone, resulting in a set of m lines, where m is the multiplicity of the hkl reflection. More information about descriptors of orientations can be found in [35].

In the initialization process, Rodrigues search lines for all pairs and compatible angles between all combinations of two (hkl) plane normals are pre-calculated and stored in memory to save computation time later. Friedel pairs are ordered according to their average spot intensity in order to speed up searches in stages 1 and 3, as pairs with similar intensities are more likely to belong to the same grain. Stages 1 to 3 are applied iteratively, while stages 4 to 6 are sequential refinements.

1. *Search for new grains.* New grains are found by a consistent search for small subsets of pairs that may constitute a grain. A subset must contain a preset minimum (usually 3 to 5) of Friedel pairs which are all consistent pairwise in terms of bounding box sizes, intensity, area and the angle between the scattering vectors. Furthermore, their diffracted beam paths need to intersect at the same point (within errors) in the sample envelope, as well as their Rodrigues lines in the fundamental zone. In order to optimize speed, consistency criteria are applied in an increasing order of approximate computation time – the latter two criteria being the most demanding – and only in the case of positive results from the previous checks. Grain locations, orientations and the specific {hkl} family in the grain are assigned to the indexed Friedel pairs.

2. *Merging existing grains.* Friedel pairs originating from the same grain may be

erroneously split between two or more grains as they only fulfill the constraints as separate subsets in stage 1 in the early iteration steps. These grains are identified as having close centroid location, orientation and spot properties, and are merged into one grain.

3. *Extending existing grains.* The tolerances used in stage 1 are loosened, so that more Friedel pairs can be assigned to the already existing grains.

4. *Statistical refinement.* Statistics on the deviation of the plane normals and diffracted beam paths from the average expected values and on the spot properties are calculated for every grain. Additional pairs whose properties fall closer than a few (usually 3 – 4) standard deviations from the mean values are included in the grain. Outlier pairs are identified and excluded in a similar manner. The strength of this additional refinement is that it depends little on the parameters preset by the user but primarily on the actual data set.

5. *Adding single spots to grains.* Once the grains have been indexed, a scattering vector and hkl reflection for any diffraction spot can be determined with respect to the center of a grain. Unpaired and paired but unindexed diffraction spots can thus be tested for consistency on the basis of the statistical principles mentioned in stage 4 and can be included in the indexed grains.

6. *Removal of overlapping spots.* The expected diffraction spot positions for all grains and all hkl reflections are calculated to account for diffraction spots that may not have been segmented and indexed. Potentially overlapping spots are thus detected and optionally removed from the grains for better reconstruction of grain shape, or for orientation and strain fitting.

If the maximum number of Friedel pairs from a given (hkl) plane in a 360° scan (which is 2) is exceeded, only the best fitting two Friedel pairs are kept in the grain, and the others are moved to the unindexed set. If the data set constitutes a low risk for erroneous assignments (e.g. because of little strain and/or mosaicity and/or accurate segmentation), iteration of stages 1 to 3 can be avoided and the algorithm can be run fully sequentially. Steps 4 to 6 are optional but are expected to improve the grain shape reconstructions. The typical running time on a single processor in iterative mode excluding steps 5 and 6 is of the order of minutes for hundreds of grains and tens of minutes for thousands of grains.

Once the grain positions and orientations have been identified, the locations of all other diffraction spots belonging to each grain can be predicted through a forward

simulation approach. Hence, other unpaired, diffraction spots can be added to the sets.

4.7 Shape reconstruction

The three-dimensional shapes of indexed grains are reconstructed individually from their diffraction spots before being assembled in a grain map.

Algebraic reconstruction techniques [9] have proved to be successful in reconstructing both convex and concave grain shapes, despite the limited number of available projections (see Figure 2.5.1 again).

A SIRT algorithm has recently been integrated into the processing route from the ASTRA (*All Scale Tomographic Reconstruction Antwerp*) Tomography Toolbox (Palenstijn *et al*., 2011), a MATLAB toolbox based on high-performance GPU primitives for 2D and 3D tomography, developed jointly by the ASTRA-Vision Lab research group at the University of Antwerp (Belgium) and CWI, Amsterdam (The Netherlands) and available for free at http://sourceforge.net/p/astra-toolbox/wiki/Home/ . It enables reconstructions from arbitrary three-dimensional oblique angle projections and thus it is well adapted to the diffraction geometry. Thanks to GPU acceleration, reconstruction times are as short as a few seconds even for large grains. For the best reconstruction quality, the diffraction spots are segmented using soft thresholding, as explained in section 4.4.

However, before the projections of a given grain set can be input to a tomographic reconstruction algorithm, one has to eliminate the dependence on the scaling function $m \propto |F_{hkl}|^2 L$ (different families of hkl reflections give rise to different diffracted intensities, section 4.2). If the structure and Lorentz factors are known (i.e. after indexing and orientation determination), one may normalize the projections images by dividing them by these multiplicative factors. Otherwise, one may eliminate the dependency on m by dividing each of the projection images by its own integral. This is due to the fact that the area integral (two-dimensional) of a parallel projection image is equal to the volume integral (three-dimensional) of the underlying object function and hence is independent of the projection direction.

The projection geometry is calculated from the fitted grain orientation (and strain) as the predicted diffracted beam directions. Accounting for the average strain state of the grains is expected to provide improved accuracy as it influences the lattice plane orientations. The projection directions could alternatively be determined from the observed spot centroids and fitted grain centroids. Nevertheless, both are prone to errors and so the approach is expected to be less robust than using the average

orientation.

Using the diffraction spots has several advantages over the extinction spots which were previously used [30, 31]. They are much less affected by spot overlap, as they are spread over a larger area of the detector. Furthermore, since diffraction spots are recorded as a bright spot on a dark background, whereas the extinction spots are recorded as missing intensity in the direct beam, the diffraction spots have better contrast and are less affected by noise.

4.8 Optional postprocessing of the grain map

The final grain map is assembled by placing the individual grain reconstructions at their correct positions. Postprocessing operations might be needed in order to resolve cases where a voxel has been assigned to more than one grain or it has not been assigned to any grain, which is physically unacceptable. Unlabeled voxels thus give rise to grain maps that are not completely space-filling. A 3D morphological dilation of the grains into such unlabeled voxels may be applied, until all the voxels have been assigned. Reasonable physical constraints are used, that is, grains are allowed neither to grow into each other, nor to grow beyond the reconstructed sample volume.

As an example, results from a small fragment of UO_2 of irregular shape are shown (Figure 4.8.1).

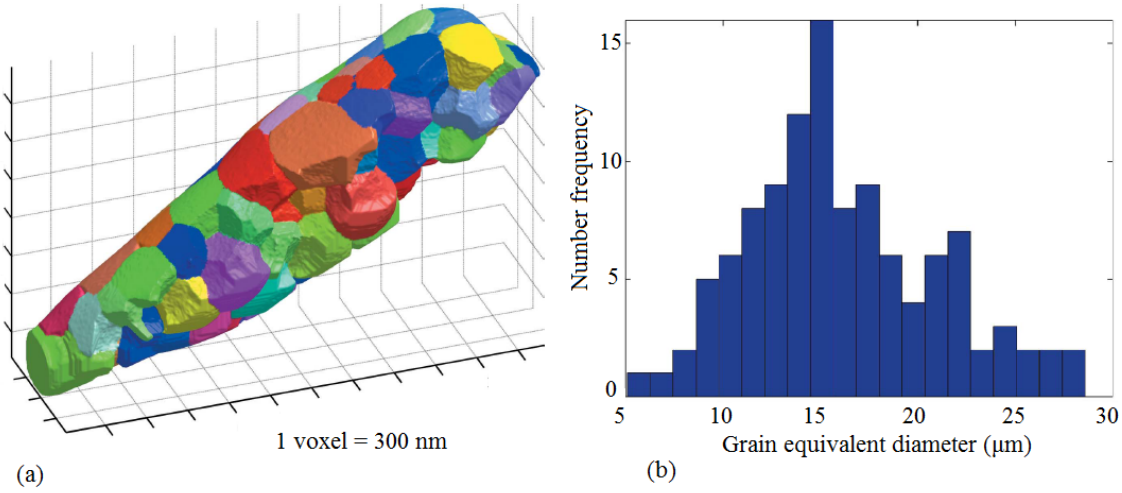

Figure 4.8.1: Reconstruction results of a UO_2 sample containing 119 grains. (a) High resolution DCT grain map. Some grains are not rendered for better visibility of other subsurface grain boundaries. (b) Histogram of the average grain diameters. [32]

The maximum sample dimension is about 100 μm. The DCT processing reconstructed 119 grains from the observed diffraction spots. The average grain diameter is about 15 μm, and the smallest reconstructed grains are less than 10 μm in diameter. Figure 4.8.1a shows the final reconstruction, after dilation of grains, while Figure 4.8.1b collects some statistics on average grain diameters. The accuracy of the reconstructed grain map is estimated to be around 1 μm, by considering how well adjacent grains fit together in the final assembled volume before the optional morphological dilation step.

Chapter 5

DCT WITH NON PERPENDICULAR ROTATION AXIS

THE topic of this chapter is the reconstruction of polycrystalline samples with DCT when the axis of rotation and the direction of the beam have some known perpendicularity error. The study was a review of a manuscript submitted by Qiru Yi (Institute of High Energy Physics, Beijing) *et al.* to the supervisor (Wolfgang Ludwig, ID11, ESRF). It is justified by the wish to perform reconstruction of the sample even if some misalignment errors have occurred during the measurements. This would imply no need to repeat experiments in the correct geometry, which is good if one thinks of quite short beam time slots at ESRF. Furthermore, being able to predict the behavior of diffraction spots when misalignment errors occur would relax the geometric acquisition requirements of DCT experiments.

In particular, the validity of the current matching algorithm for DCT data processing (which has been outlined in section 4.5) has been tested, and some modifications have been applied in order to account for these new conditions. An Al 2.5 % Li alloy sample was investigated in two different acquisition geometries:

- the rotation axis is perpendicular to the beam direction;
- the rotation axis is inclined by 0.5° towards the incoming beam.

A comparison between reconstructions in the two cases was carried out, showing that an exact prediction of Friedel pairs is now complicated by a number of factors which altogether lead to a decrease in reconstruction performances.

5.1 Geometric approach to diffraction and Friedel Pairs

An efficient algorithm in the theory of three-dimensional rotation is worth quoting at this point because of its later use.

Theorem 5.1.1. ***Rodrigues rotation formula****. [36] Let* $\mathbf{v}$ *be a vector in* $\mathbb{R}^3$ *and* $\mathbf{r} \in \mathbb{R}^3$ *be a unit vector describing an axis of rotation about which* $\mathbf{v}$ *rotates by an angle* ω *according to the right-hand rule. Then, the rotated vector* $\mathbf{v_{rot}}$ *can be expressed as*

$$\mathbf{v_{rot}} = \mathbf{v}\, cos\,\omega + (\mathbf{r} \times \mathbf{v})\, sin\,\omega + \mathbf{r}\,(\mathbf{r} \cdot \mathbf{v})\,(1 - cos\,\omega) \tag{5.1.1}$$

The same equation can also be expressed in matrix notation. If we represent $\mathbf{v}$ and $\mathbf{r} = (r_1; r_2; r_3)$ as column vectors, we obtain

$$\mathbf{v_{rot}} = \mathbf{S_{rot}}\,\mathbf{v}$$

where $\mathbf{S_{rot}}$ is the rotation tensor associated with the rotation about $\mathbf{r}$ by the angle ω. It can be decomposed in the sum of three terms

$$\mathbf{S_{rot}} = \mathbf{S_{const}} + \mathbf{S_{cos}}\, cos\,\omega + \mathbf{S_{sin}}\, sin\,\omega$$

with

$$\mathbf{S_{const}} \equiv \mathbf{I} + \mathbf{R^2} \qquad \mathbf{S_{cos}} \equiv -\mathbf{R^2} \qquad \mathbf{S_{sin}} \equiv \mathbf{R}$$

$$\mathbf{I} \equiv \begin{pmatrix} 1 & 0 & 0 \\ 0 & 1 & 0 \\ 0 & 0 & 1 \end{pmatrix} \qquad \mathbf{R} \equiv \begin{pmatrix} 0 & -r_3 & r_2 \\ r_3 & 0 & -r_1 \\ -r_2 & r_1 & 0 \end{pmatrix}$$

Hence, if $\mathbf{p_{lab}}$ is a given plane normal in the laboratory coordinate system, the incident beam $\mathbf{b}$ will be diffracted at Bragg angle θ at rotation angles ω such that

$$\mathbf{b} \cdot \mathbf{p_{lab}} = \pm\, sin\,\theta \tag{5.1.2}$$

The Rodrigues rotation formula 5.1.1 links the plane normal vectors in the laboratory coordinate system $\mathbf{p_{lab}}$ and in the sample coordinate system $\mathbf{p}$:

$$\mathbf{p_{lab}} = \mathbf{S_{rot}}\,\mathbf{p}$$

so that equation 5.1.2 can be rewritten as

$$\mathbf{b} \cdot (\mathbf{S_{const}}\,\mathbf{p}) + \mathbf{b} \cdot (cos\,\omega \cdot \mathbf{S_{cos}}\,\mathbf{p}) + \mathbf{b} \cdot (sin\,\omega \cdot \mathbf{S_{sin}}\,\mathbf{p}) = \pm\, sin\,\theta$$

This implies solving two quadratic equations (one with + sign in the equation , the other with - sign) in the following form

$$A\,cos\,\omega + B\,sin\,\omega + C = 0$$

with

$$A \equiv \mathbf{b} \cdot \mathbf{S_{cos}}\,\mathbf{p} \qquad B \equiv \mathbf{b} \cdot \mathbf{S_{sin}}\,\mathbf{p} \qquad C \equiv \mathbf{b} \cdot \mathbf{S_{const}}\,\mathbf{p} \mp sin\,\theta$$

each of which has two solutions

$$\omega = 2\,atan\left(\frac{-B \pm \sqrt{A^2 + B^2 - C^2}}{C - A}\right)$$

The overall four solutions correspond to the four reflections from four directions in the laboratory coordinate system and the same crystal plane in the system rotating with the sample.

Figure 5.1.1 explains the difference between the two acquisition geometries which were tested. Let φ be the angle between the plane normal of lattice plane (hkl) and the negative direction of the beam. When diffraction from (hkl) lattice plane at Bragg angle θ occurs at rotation angle ω, φ = 90° - θ. In the condition where the axis of rotation is perpendicular to the incident beam, diffraction occurred at $\overline{(hkl)}$ lattice planes will appear at $\omega + 180°$ with φ = 90° + θ. When the rotation axis is not perpendicular to the incident beam, the angle offset between the pair spots is different from 180°.

An immediate visualization of the solutions to the two quadratic equations can be found by giving an explicit expression of φ. Coming back to the rotated plane normal via the Rodrigues formula, one gets

$$\mathbf{p_{rot}} = \mathbf{p}\,cos\,\omega + (\mathbf{r} \times \mathbf{p})\,sin\,\omega + \mathbf{r}\,(\mathbf{r} \cdot \mathbf{p})\,(1 - cos\,\omega) \qquad \mathbf{p} = (p_1, p_2, p_3)$$

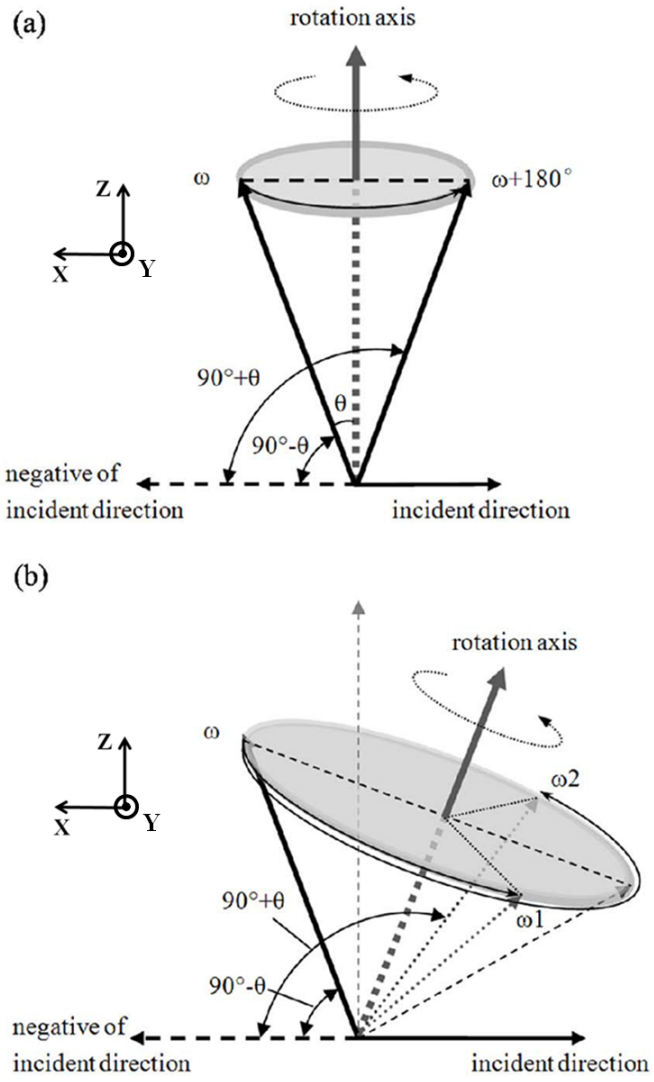

Figure 5.1.1: (a) Friedel pairs representation when the axis of rotation is perpendicular to the incident beam. (b) The pair of the diffraction spot appeared at ω does not appear at $\omega + 180°$ when the axis of rotation is inclined. (from the unpublished manuscript by Qiru Yi *et al*, 2014)

which can be written as

$$\mathbf{p_{rot}} = (p_1, p_2, p_3) \begin{pmatrix} r_1^2(1-c\omega) + c\omega & r_1 r_2 (1-c\omega) + r_3 s\omega) & r_1 r_3 (1-c\omega) - r_2 s\omega) \\ r_2 r_1 (1-c\omega) - r_3 s\omega) & r_2^2 (1-c\omega) + c\omega & r_2 r_3 (1-c\omega) + r_1 s\omega) \\ r_3 r_1 (1-c\omega) + r_2 s\omega) & r_3 r_2 (1-c\omega) - r_1 s\omega) & r_3^2 (1-c\omega) + c\omega \end{pmatrix}$$

where $c\,\omega = cos\,\omega$ and $s\,\omega = sin\,\omega$. Assuming the negative direction of the beam to be (1, 0, 0), the relationship between φ and ω is finally obtained:

$$cos\,\varphi = \frac{\mathbf{p_{rot}} \cdot (1,\,0,\,0)}{p_{rot}}$$

which becomes, after expansion:

$$cos\,\varphi = (p_1\,r_1^2 + p_2\,r_2\,r_1 + p_3\,r_3\,r_1)\cdot(1 - cos\,\omega) + p_1\,cos\,\omega - (p_2\,r_3 - p_3\,r_2)\,sin\,\omega \quad (5.1.3)$$

Diffraction holds for φ = 90° $\pm\,\theta$, giving rise to a maximum of four solutions. Figure 5.1.2 graphically shows the solutions for an axis of rotation inclined 0.01° towards the incoming beam direction in XZ plane.

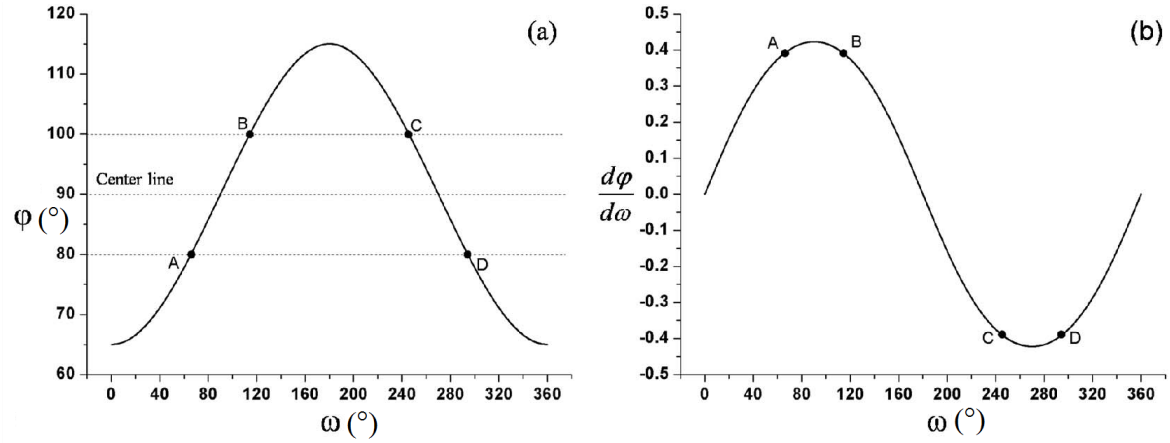

Figure 5.1.2: (a) shows how φ changes with ω in the condition that the axis of rotation is inclined 0.01° towards incoming beam direction in XZ plane. ω where diffraction is occurring for Bragg angle θ = 10° are labeled as A-D. (b) shows the gradient of the curve $\varphi(\omega)$ in (a) and the corresponding positions of A-D. (from the unpublished manuscript by Qiru Yi *et al*, 2014)

As a first application of equation 5.1.3, the family of {hkl} crystal planes corresponding to θ = 10° and a rotation axis inclined by 0.01° to the vertical axis towards the incoming beam (negative X - positive Z plane region) are considered. The corresponding rotation angles of the first Friedel pair for different plane normals in XZ plane have been calculated, together with the omega displacement from 180° required for the observation of the pair spots (Table 5.1.1). It can be seen that the closer the

plane normal to the XY plane, the smaller the displacement. When the plane normal is close to the XY plane, the absolute gradient of $\varphi(\omega)$ is large, causing negligible displacement in omega offset from 180°. On the other side, plane normals close to the Z axis will take greater effect from non perpendicular axis of rotation.

Normal vector	Rotation angle (A)	Rotation angle (C)	$\Delta\omega \equiv 180° - (C - A)$
[sin(15°), 0, cos(15°)]	47.88°	227.78°	0.10°
[sin(30°), 0, cos(30°)]	69.69°	249.65°	0.04°
[sin(45°), 0, cos(45°)]	75.79°	255.77°	0.02°
[sin(60°), 0, cos(60°)]	78.44°	258.43°	0.01°
[sin(75°), 0, cos(75°)]	79.65°	259.64°	0.01°
[sin(90°), 0, cos(90°)]	80.00°	260.00°	0.00°

Table 5.1.1: Rotation angles corresponding to Friedel pair A, C and displacement from 180° for different plane normal vectors belonging to {hkl} crystal planes with θ = 10°. The rotation axis is assumed to be inclined by 0.01° to the vertical axis towards the incoming beam. (from the unpublished manuscript by Qiru Yi *et al*, 2014)

5.2 Modifications applied to the matching algorithm

The main idea to account for non perpendicularity errors is to consider that part of the matching algorithm dealing with the search of pair candidates for each diffraction spot.

As discussed in the previous sections, the calculation of the exact rotation angles at which reflections are observed for each given plane normal in the sample coordinate is feasible. What is still unknown at this stage of the analysis is the position of the scattering grain inside the sample, since it is not needed in order to match pair spots only if the direction of the beam and the axis of rotation are perpendicular to each other. This uncertainty implies an uncertainty in the prediction of the offset rotation angle where a pair is found. This adds on top of the already present tolerances accounting for possible differences in size, shape, and intensity between pair spots.

The choice which has been taken was to determine plane normals and diffracted vectors for each observed spot as if the scattering grain was located on the eight vertices of the sample bounding box, leading to eight different predictions of the rotation angle. The limits (in number of images) for search of the pair were set to

$$lower\ limit\ =\ min_{vertex}\left(\omega_{vertex}\right) / \delta\omega\ -\ tolerance \tag{5.2.1}$$

$$upper\ limit\ =\ max_{vertex}\left(\omega_{vertex}\right)/\,\delta\omega\ +\ tolerance \tag{5.2.2}$$

where $min_{vertex}\left(\omega_{vertex}\right)$ and $max_{vertex}\left(\omega_{vertex}\right)$ are respectively the minimum and the maximum among the eight rotation angles calculated (one for each vertex of the sample bounding box), and $\delta\omega$ is the angular range over which the signal is integrated on the detector, to form a single image. This assumption is supposed to make its best predictions when the uncertainty is small, that is, when the region illuminated by the direct beam is negligible compared to the whole detector area, so that the portion of the sample illuminated by the direct beam can be assumed to be a point and the scattering point is no more unknown.

A simple MATLAB script computing the said algorithm has been attached in Appendix **??**.

5.3 Experiment results

DCT experiments were performed at beamline ID11 at ESRF. The sample was a cylindrical Al 2.5 % Li alloy with diameter of 0.85 mm and mean grain size of about 130 μm. X-ray energy was 40 keV and the illumination was limited to roughly 1.20 mm $\times$ 0.72 mm by slits. The two-dimensional X-ray detector was a CCD camera FRELON HD2k containing 2048 $\times$ 2048 pixels and coupled via visible light optics to a luminescent screen, resulting in an effective pixel size of 1.4 μm. The sample was rotated over 360° with a step size of 0.1°.

In the following part of this section, results of reconstructions for two acquisitions in different geometries are shown, with particular focus on performances of the modified matching algorithm. The first acquisition was done in perfect alignment, the second one with a non-perpendicularity error of 0.5°.

5.3.1 Acquisition with no perpendicularity errors

Data processing was performed as discussed in chapter 4. The current matching algorithm, that is, the one not accounting for perpendicularity errors, gave the results shown in Table 5.3.1.

Total number of spots considered	8592	100 %
Number of pairs analyzed	4529	100 %
Number of matched pairs	1748	43.0 %
Number of pairs matched with $260° < \eta < 280°$	357	20.4 %
Refined position X (mm)	8.6450	sample - detector distance
Refined position Y (mm)	0.8352	lateral offset of detector

Table 5.3.1: Matching performances for aluminum - lithium sample with no perpendicularity errors.

Based on this, the observed diffraction spots could be grouped into 205 grains, making up a space filling reconstruction.

Some slices of the reconstructed sample are shown in Figure 5.3.1, and Table 5.3.2 shows indexing results.

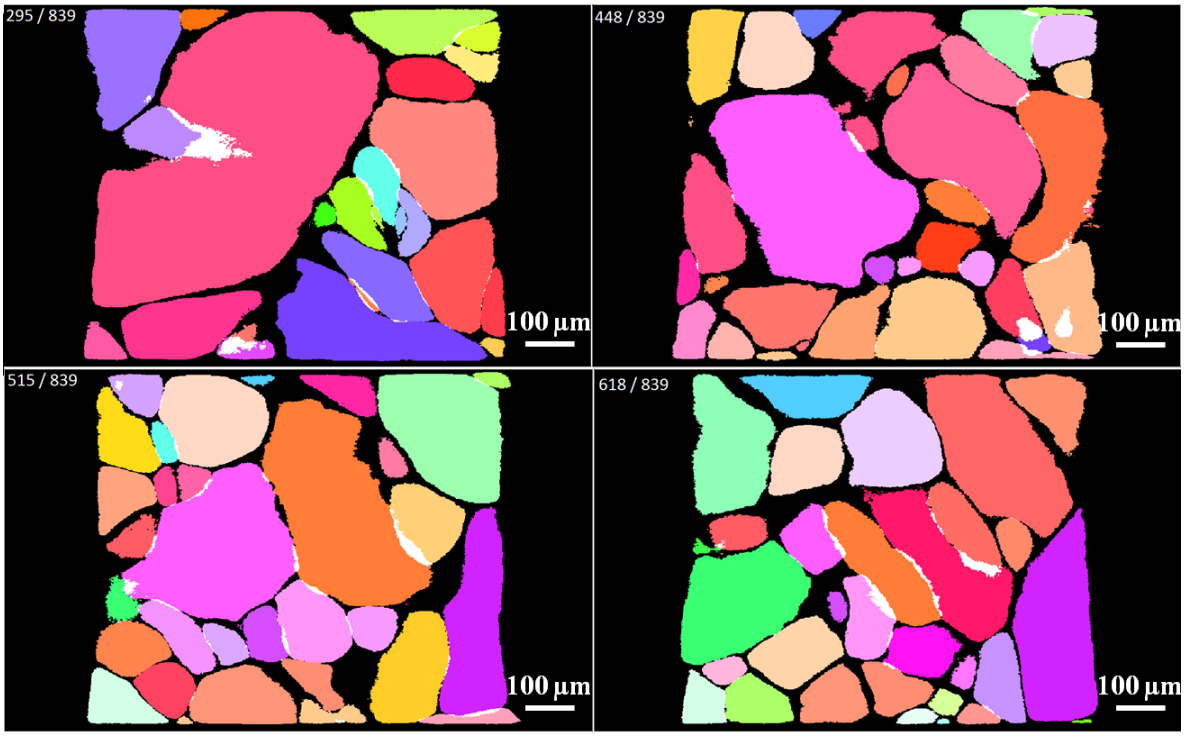

Figure 5.3.1: Reconstructed slices of the sample from aligned acquisition geometry. The number of each slice is indicated on the upper-left corners.

Number of grains found	205
Pairs per grain average	6.23
Number of pairs ...	
indexed in total	+ 1278
indexed in iterations	1228
fitted using grain statistics	50
excluded using grain statistics	0
unindexed	+ 470
input in total	= 1748

Table 5.3.2: Indexing performances for aligned acquisition geometry.

5.3.2 Acquisition with misaligned axis of rotation and discussion

In order to account for misalignment between the axis of rotation and the direction of the beam, all the vectors in the laboratory coordinate system except for the axis of rotation were rotated by 0.5° in such a way that the direction of the beam is still perpendicular to the detector plane.

Results obtained applying the new matching algorithm, which should account for the axis of rotation inclined by 0.5° towards the incoming beam, are shown in Table 5.3.3.

A comparison between the two algorithms can be found as well. Results applying the current matching algorithm are shown in Table 5.3.4.

Total number of spots considered	9328	100 %
Number of pairs analyzed	5268	100 %
Number of matched pairs	817	20.1 %
Number of pairs matched with $260° < \eta < 280°$	356	43.6 %
Refined position X (mm)	8.6450	sample - detector distance
Refined position Y (mm)	0.8352	lateral offset of detector

Table 5.3.3: Matching performances for aluminum - lithium sample with 0.5° perpendicularity error using the new version of matching algorithm.

Total number of spots considered	9328	100 %
Number of pairs analyzed	5268	100 %
Number of matched pairs	776	19.1 %
Refined position X (mm)	8.6450	sample - detector distance
Refined position Y (mm)	0.8352	lateral offset of detector

Table 5.3.4: Matching performances for aluminum - lithium sample with 0.5° perpendicularity error using the current version of matching algorithm.

Some observations can be made based on the above results.

Both the new and the current algorithm manage to match about half of the spots when the acquisition geometry is changed to the misaligned one, so the prediction of the rotation angle at which the pair spot should be found brings no significant improvements, at least to this data set.

The new algorithm mostly succeeds when analyzing the spots lying close to the horizontal (XY) plane, i.e. the ones for which η is close to 270° and plane normals have negligible z-component. This statement can be easily confirmed by checking the fourth entry in Tables 5.3.1 and 5.3.3, and it may have been expected according to the conclusions drawn on section 5.1.

The increase in the number of matched spots is from 19.1 % to 20.1 %, as one can see in Tables 5.3.3 and 5.3.4. A visual analysis by eye of the images allows to conclude that only 50 % of matched spots look very similar and make a pair with no doubts. Matching percentages can be increased, up to about 25 %, by allowing for larger tolerance values, at the costs of a worse quality of pair matching. Then, care should be taken when enlarging search limits to try overcome perpendicularity errors.

It has been found, in fact, that the used prediction of the number of image where the pair spot is supposed to be found leads to a search interval much larger than the search intervals employed in conventional matching. Table 5.3.5 shows the lower and upper limits calculated with equations 5.2.2-5.2.2 for a set of observed diffraction spots. These results have to be compared to the limits of search of the conventional matching algorithm, that are, 4-image intervals centered around the corresponding 180° offset images for each spot. It must be recalled that such large intervals are due to the unavoidable uncertainties on the positions of the scattering grains.

This is thought to be one of the reasons why matching performances do not improve: the current criteria employed in the search of pair spots, namely similarities in size of the bounding boxes enclosing the spots, their intensities, and their areas, appear no more sufficient when looking into a large ($\gg 4$) number of images.

Spot ID	Image	Lower image limit	Upper image limit	Amplitude
1	1330	3083	3140	57
2	897	2689	2698	9
3	708	2507	2520	13
4	450	2248	2259	11
5	641	2440	2456	16
6	437	2217	2250	33
7	1525	3329	3348	19
8	1133	2925	2934	9
9	257	2054	2070	16

Table 5.3.5: Predicted intervals for the search of the pair spot for a set of nine diffraction spots using the modified version of the matching algorithm.

The small number of pairs per grain do not allow an acceptable indexing of the grains (see Table 5.3.6 below). Results are shown in Table 5.3.6 and clearly indicate that more pairs are needed in order to index grains.

Number of grains found	8
Pairs per grain average	3.00
Number of pairs ...	
indexed in total	+ 24
indexed in iterations	24
fitted using grain statistics	0
excluded using grain statistics	0
unindexed	+ 793
input in total	= 817

Table 5.3.6: Indexing performances for misaligned acquisition geometry.

5.4 Conclusions

The aim of this study was to determine whether it is possible to analyze data taken with some known perpendicularity error and still be able to reconstruct the sample.

The idea behind the unpublished work by Qiru Yi *et al* (2014) is to use only spots lying in the "horizontal" plane (i.e., the ones with $\eta \approx 90°$, or $\eta \approx 270°$), since they are less affected by such misalignment. Based on this, a slightly different study was carried out: try to predict the rotation angles at which Friedel pairs occur for each diffraction spot, no matter its azimuthal position on the detector.

Matching and indexing results lead to the conclusion that the prediction model described in section 5.2 does not work on this data set. Most of the pairs which were matched correspond to spots lying on the horizontal plane. Then, the new algorithm behaves as the old one. It has been shown that the uncertainty in the position of the scattering grains leads to such a large broadening of search intervals, that the current similarity criteria used to identify pairs are no more efficient.

A way to improve the reliability of this prediction is to let the sample and the direct beam bounding boxes be very small compared to the detector area, so that uncertainties in grain positions are small. An order of magnitude can be given considering the current case, where the portion of the detector covered by the direct beam (a figure of merit which can be called *fill factor FF* of the detector) is

$$FF = \frac{direct\,beam\,area}{detector\,area} = \frac{856\,pixels \times 516\,pixels}{2048\,pixels \times 2048\,pixels} = 10.5\,\%$$

Then, fill factors much smaller than 10 % have to be employed in order to match a sufficient number of spots allowing the reconstruction of the sample.

In order to increase the number of spots both in horizontal and in vertical planes, more crystallographic families are needed, as well. Reducing the sample to detector distance and using higher energy X-ray radiation could be some valuable solutions.

5.5 Further developments

A different and more complicated modification for the matching algorithm is only suggested here, just in case further solutions to the problem will be needed in the future. If one wants to overcome the said uncertainties, one should try to make a better guess of the position of the grain center corresponding to a specific diffraction spot. The following steps could then be followed:

- Divide the sample bounding box in N cubic cells;
- For each diffraction spot belonging to the first half:
  - For each cell belonging to the sample, determine the diffracted vector, the plane normal and Bragg angle θ_{calc}

- Choose the best θ_{calc} as the closest to one element in the set of $\theta_{\{hkl\}}$, which is theoretically calculated from Bragg's law
- The corresponding cell is the best possible guess for the chosen size of the cubic cells. The same holds for the diffracted vector and the plane normal. Since there must be only one cell whose θ_{calc} matches $\theta_{\{hkl\}}$, N can not be too low, i.e., the division in cells has not to be too coarse
- Draw the cone whose vertex is in the diffraction spot considered and with opening angle twice the Bragg angle chosen
- Based on the best diffracted vector and plane normal, predict ω offset between a spot and its pair in a way similar to that employed here
- Once the images potentially containing the pair have been found, get Debye - Scherrer rings and sample envelope in the way described in 4.5 and determine a search zone for the corresponding pair
- Apply the search criteria already present in the current matching algorithm and determine the pair spot.

Chapter 6

RECONSTRUCTION OF LOCAL ORIENTATIONS IN GRAINS USING A SIX-DIMENSIONAL ALGORITHM: PRINCIPLES AND VALIDATIONS

RECENTLY, considerable effort has been put into the creation and improvement of algorithms for the solution of the general problem of the microtexture analysis. In this chapter, a new algorithm by Nicola Viganò (PhD thesis student at ESRF, ID11) [37], allowing for the reconstruction of local orientations in grains and using data from monochromatic beam three-dimensional X-ray diffraction techniques, is presented. In section 6.1 the problem of the reconstruction of deformed grains is discussed, explaining the reasons why sampling of the orientation space is needed. Section 6.2 contains a brief summary of the mathematical framework leading to the definition of the six-dimensional space over which the optimization is performed. Performances are tested on real experimental data in the next sections. In section 6.3, a *surface validation* is carried out through a comparison between the six-dimensional DCT reconstruction and an EBSD mapping of a Ti alloy sample surface. Finally, in section 6.4, the results of the new algorithm are compared to experimental data acquired from a Mg multicrystal sample characterized by pinhole and section topography.

6.1 The need for a better reconstruction of deformed materials

The reconstruction approach behind DCT, involving algebraic techniques like SIRT (see section 2.5), performs very well for undeformed materials exhibiting limited ($\lesssim$ 0.5°) intra-granular misorientation spreads. In such cases, one can assume that a single constant orientation is present in the whole grain volume.

The natural extension of this three-dimensional reconstruction model includes a sampling of the local orientation space, centered around the grain average orientation, and extends its applicability to materials exhibiting intra-granular orientation spread of up to several degrees. In order to benefit from the six-dimensional approach, experiments must be performed in such a way that diffraction signals from different grains have limited overlap. A suitable acquisition geometry has already been described in section 3.7.5. For moderately deformed materials, the previously described indexing approaches still allow to determine the average grain orientations, which are then assumed to be known to the six-dimensional algorithm. The dimensions of the illuminating beam may possibly be restricted to a one-dimensional line beam or even to pencils, thus reducing the convolution of the signals on the detector from three-dimensional volumes to one-dimensional line integrals through the illuminated sample volume. Figure 6.1.1 shows the diffraction of one grain in a near-field diffraction imaging experiment for both full beam and line-beam illumination.

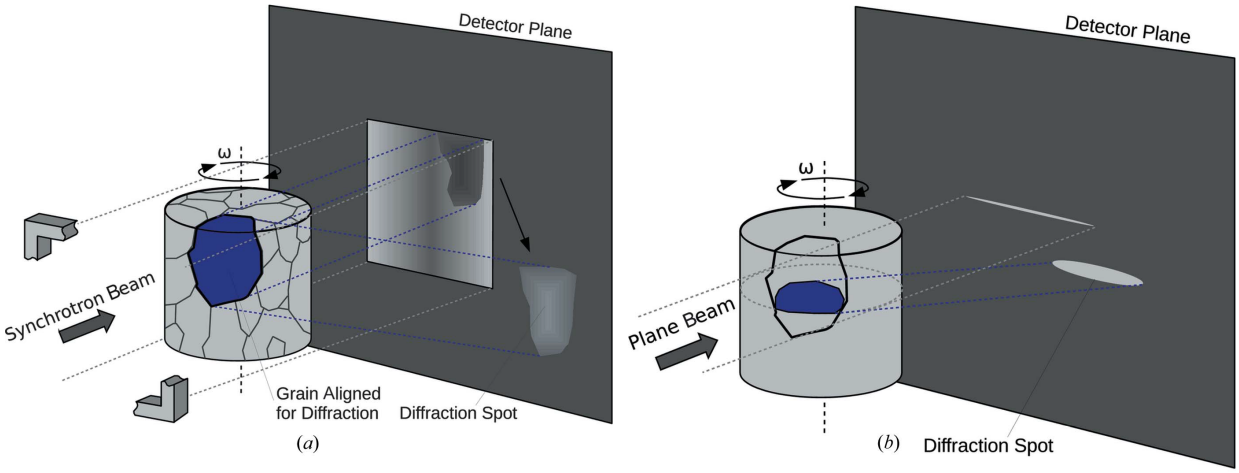

Figure 6.1.1: Diffraction of one grain in a near-field diffraction experiment, performed with (a) two-dimensional full-beam illumination and (b) one-dimensional line-beam illumination. [37]

When using previously established algorithms for reconstruction of deformed materials, one would very often face two main problems:

- Some crystallites are not indexed. This mainly happens in textured materials and/or deformed materials, where several crystals share a common orientation or break up into overlapping subspots.
- The hypothesis of parallel projection of grains may no longer be correct. In fact, in the idealized case of completely undeformed grains, each of them can be considered a perfect lattice. All voxels belonging to the same grain give rise to diffraction signals, referred to as *diffraction spots,* in the same direction and for the same angles of rotation. The grain volume is simply geometrically projected on the detector, so its shape can be reconstructed by oblique angle tomography techniques, like SIRT. On the other hand, when the whole grain exhibits some variations in orientation between close regions, it is not projected on a single detector image per reflection any more. In this case, different volume elements of the grain will project on a range of adjacent images, giving rise to a three-dimensional entity per reflection (two spatial coordinates on the detector and one corresponding to the angles of rotation), which is referred to as a *diffraction blob* (Figure 6.1.2). Moreover, the directions of the scattered beams from the same grain will no longer be parallel, thus leading to a distorted projection of the grain volume on the detector.

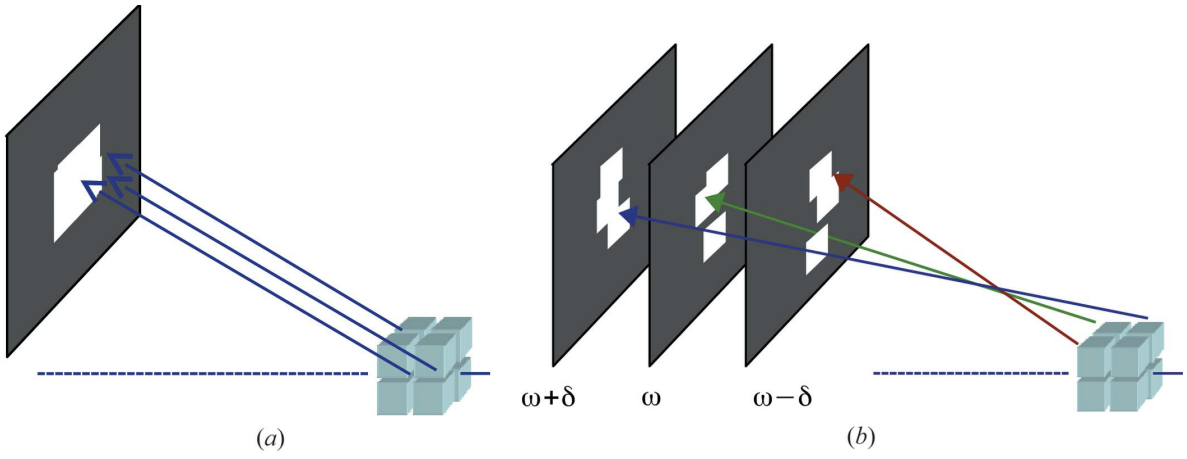

Figure 6.1.2: Projection of (a) a “perfect” grain with one single orientation and of (b) a “deformed” grain, giving rise to a 3D diffraction blob volume. [37]

It should be noted that the previous three-dimensional reconstruction approach like the one described in chapter 4 would use diffraction spots, created by summing

the corresponding blobs along the ω direction, so that diffraction signals would be treated as parallel projections of the (deformed) grain volume (see section 4.4). This can be done without significant loss in the quality of the reconstruction as long as the grain deformation is $\ll 1°$. In the other cases, it becomes necessary to include this orientation spread into the reconstruction process.

6.2 Mathematical model

Synchrotron-based microstructure mapping techniques are either based on the solution of the forward problem or of the inverse one.

Algorithms solving the former problem analyze the possible scattering from localized region of the sample and search for optimum orientations over a discrete orientation space. An outstanding example is the adaptive reconstruction method from Suter et al. [38, 39], which reconstructs the orientation of each voxel in the sample by minimizing a cost function involving combinatorial and local, voxel-wise optimization of the simulated diffraction signals against the experimental data.

On the other hand, the DCT mapping technique is based on the solution of the inverse problem of finding the underlying material structure that would give rise to the observed diffraction images on the detector.

6.2.1 Formulation of the problem

The optimization performed in the present case is a fully six-dimensional one. In order to do so, a discrete six-dimensional reconstruction space is defined as the outer product between the three-dimensional real space and orientation space:

$$\mathbb{X}^6 = \mathbb{R}^3 \otimes \mathbb{O}^3$$

where the local orientation space is chosen as a discrete Rodrigues space, which is known to be almost Euclidean for small deformation components [35]. This implies that we can regard the six-dimensional space as either:

1. a collection of three-dimensional discrete orientation spaces, one for each volume element; or, conversely,

2. a collection of real space volumes, one for each sampled orientation.

Let $\mathbf{x} \in \mathbb{X}^6$ represent an element of this six-dimensional space, and let each of them be mapped to a scalar value, which is regarded as the scattering power for that cor-

responding element. In many cases, the assumption of *sparsity* of the signals can be made, that is, most of such scalar entries would be zero, since a given real space voxel will contain only a small subset of the sampled orientations. The formulation of the problem is based on the classical forward-projection operator $\mathbf{A}$ which is commonly used in tomography:

$$\mathbf{A}\,\mathbf{x} \;=\; \mathbf{b}$$

where $\mathbf{b}$ is a collection of all measured pixel intensities on the detector during the rotation of the sample, so it is a vector, representing a three-dimensional entity with two spatial dimensions and one corresponding to the rotation angles. The solution $\mathbf{x}$ is the set of intensities corresponding to each element in real space, giving rise to the measured distribution of pixel intensities on the detector. Now, since each real space element is associated to a three-dimensional vector in orientation space, the projection matrix $\mathbf{A}$ becomes a stack of projection matrices, one for each sampled orientation. It should be noted that each of these projection matrices is constant. If the number of sampled orientations is N, the linear system to be solved is:

$$\mathbf{A}\,\mathbf{x} \;=\; \sum_{i=1}^{N} \mathbf{A}_i\,\mathbf{x}_i \;=\; \mathbf{b} \tag{6.2.1}$$

Assuming the real space and the orientation space to be sampled by two grids of size $n \times n \times n$ and $p \times p \times p$ respectively, the dimension of the solution space is of order $O(n^3 p^3)$, while the dimensions of a diffraction blob are only of order $O(n^2 t)$, where t is the number of images onto which the blob extends. This implies the number of blobs to be of order $O(n\,p^3/t)$, or $O(n\,p^2)$ if a linear relationship between p and t is assumed, based on the fact that the lower the orientation spread of a grain, the lower the number of sampling points needed to reconstruct it. For example, considering blobs with orientation spread of 1° and 0.1° angular steps, one would have $t \sim 10$. Assuming also the size of spots to be $\sim 50 \times 50$ and the sampling of the orientation space to be each 0.1°, that would lead to $n \sim 50$, $p \sim 10$ and $\sim 50\times\ 10^2$ = 5000 required blobs, that is way more than the actual number of blobs in a scan, typically ranging from 20 to 100. That makes the problem stated in equation 6.2.1 highly underdetermined, thus requiring a minimization formulation.

It can be shown quite easily [37] that each solution minimizing the l_2 norm of the residuals:

$$\mathbf{x}^* = argmin_{\mathbf{x}} ||\mathbf{A}\,\mathbf{x} - \mathbf{b}||_2 \tag{6.2.2}$$

is also a solution of equation 6.2.1, with the advantage that any solution of equation 6.2.2 is more stable to noise. It was also demonstrated [40, 41] that an additional l_1 minimization term over the whole six-dimensional space can not only recover sparse signals, but also prefer sparse solutions in the cases where the solution is not unique. The full formulation of the problem is then the following:

$$\mathbf{x}^* = argmin_{\mathbf{x}} \left\{||\mathbf{A}\,\mathbf{x} - \mathbf{b}||_2 + \lambda\,||\mathbf{x}||_1\right\}, \tag{6.2.3}$$

$$subject\,to\,\mathbf{x} \succeq 0$$

with λ being a parameter balancing the relative importance of the data fidelity term $||\mathbf{A}\,\mathbf{x} - \mathbf{b}||_2$ and the regularization term $||\mathbf{x}||_1$. The constraint of non-negativeness of $\mathbf{x}$ both expresses the fact that diffracting powers can not be negative for physical reasons, and helps the algorithm converge quicker.

Alternatively, one can suggest a different optimization, based on a *total variation* (TV) formulation, which is expressed through the following:

$$\mathbf{x}^* = argmin_{\mathbf{x}} \left\{TV\,(T\,\mathbf{x})\right\}, \tag{6.2.4}$$

$$subject\,to\,\mathbf{A}\,\mathbf{x} = \mathbf{b}\,and\,\mathbf{x} \succeq 0\,,$$

where TV is the total variation operator $TV\,(\mathbf{x}) = ||\nabla\mathbf{x}||_1$ and T is an operator which integrates the solution $\mathbf{x}$ over the sampled orientations for each real space voxel:

$$T : \mathbb{X}^6 \longmapsto \mathbb{R}^3 \qquad (T\,\mathbf{x})_{xyz} = \sum_{a,\,b,\,c} x_{xyz,\,abc}$$

The choice of the TV approach is due to the fact that one expects the scattered intensity from a grain to be roughly constant and with sharp edges through its real space volume, so its gradient would be a sparse signal.

Recovery of sparse solutions both in problems like equation 6.2.3 and 6.2.4 can be performed using the Chambolle-Pock class of algorithm, for which the reader may find [42] of interest.

6.2.2 Main assumptions and limitations

The algorithm relies on several strong hypotheses:

- Kinematic diffraction is assumed, requiring proportionality between real space dimensions of the crystal and integrated scattered intensity. This is not always the case, since extinctions and absorption cause a deviation of the intensity from being a simple projection of the grain on the detector. Primary extinction is responsible for a loss of intensity due to multiple scattering in a single crystal according to dynamic diffraction. Fortunately, deformed materials tend to develop a mosaic structure, reducing this effect. Secondary extinction is very common in polycrystals and refers to local changes in the intensities of the diffracted beams, due to the attenuation of incident or diffracted beam by other grains satisfying Bragg's law.

- The model does not consider elastic distortion of the crystal unit cells. Otherwise, one would have to add six more dimensions to the algorithm, thus making its resolution no more feasible in terms of computational power and memory needs. Though, for crystalline materials, the effects introduced by elastic deformations are negligible compared to the misorientations which have been treated here by some degrees. For instance, pure metals yield plastically at strains far below 1 %.

- The current method treats each grain individually, so a limited overlap between blobs originating from different grains is required. The number of grains that can be simultaneously illuminated is inversely proportional to the intragranular orientation spread of each grain, and it can be reduced with the use of beam-defining slits.

The algorithm has already been validated against several synthetic cases, with convincing results [37]. The next step is to evaluate its performances on experimental data, which is the topic of the next sections.

6.3 First way of validation: Comparison with electron backscatter diffraction results

The performances of the six-dimensional algorithm were tested on a Ti 4% Al sample, the name referring to the weigth % Al content, which is close to 4 %. A comparison with a conventional three-dimensional reconstruction and with a surface mapping

obtained with *electron backscatter diffraction* (EBSD). was conducted, showing the strong points and the weaknesses of the model.

6.3.1 The Ti-4Al sample

The sample was prepared in order to study twinning mechanisms in metals with hexagonal unit cell (PhD thesis of Laura Nervo).

Twinning mechanisms in crystals lead to the formation of two or more domains with different, but symmetry related, crystal orientations. In particular, titanium alloys are very important engineering materials for their application in aerospace industry, because of their high strength to weight ratio and high-elevated temperature properties. The presence of many twinning planes in the Ti crystal lattice (which is hexagonal close packed (hcp) at room temperature) is one of the reasons why hcp Ti shows relatively high ductility, as well.

Experiments were performed on a 10 mm diameter cylinder of the material . It was compressed in a stress-rig with its longitudinal direction aligned with the {0002} plane normal, up to the onset of deformation twinning. Then it was cut to have a cylindrical sample with 400 μm diameter and 3 mm height, suitable for the DCT experiment. Finally, in order to enable EBSD surface analysis, the sample underwent a polishing treatment, so that it exposed a flat surface.

6.3.2 Experimental setup

DCT scans were performed at the ID11 beamline at ESRF, where an undulator source and a Si(111) double-crystal Bragg monochromator provided a 60 keV X-ray beam with a relative energy bandwidth of 10^{-3}.

A scan was performed over a 360° continuous rotation of the cylindrical sample with 0.1° rotation steps. The rotation axis was vertical and perpendicular to the incoming beam, as in the conventional geometry in tomographic acquisitions. The sample was illuminated by an extended beam with dimensions 0.55 mm $\times$ 0.19 mm (horizontal $\times$ vertical) defined by slits.

The detector was a FReLoN camera containing 2048 $\times$ 2048 pixels and coupled via visible light optics to a luminescent screen, resulting in an effective pixel size of 1.4 μm. It was mounted in the conventional DCT geometry, that is, centered in the direct beam and at a distance of $\sim$ 8.09 mm from the sample. The position of the detector was fitted according to Friedel pair data during the pair matching analysis.

6.3.3 Results and discussion

The detector covered a 2θ range of 15°, allowing 19142 spots to be segmented and considered by the matching routine. 2613 Friedel pairs were found, mainly from the first seven {hkl} families, from which 131 grains were indexed. The volume of the orientation space was estimated from the spread of blobs in the ω dimension. Each grain was sampled with a lattice of $9 \times 9 \times 9 = 729$ points, that is, 9 equally spaced points along each direction in orientation space, centered around the grain average orientation.

Figure 6.3.1 shows a comparison between three different reconstructions. On top of the figure, an EBSD map (courtesy of Gaurav Singh, The University of Manchester) is shown. A comparison with the part of the sample analyzed in the DCT experiment can be found at the bottom, where three-dimensional rendering of two reconstructed volumes are shown. Grain colors are based on an *inverse pole figure* (IPF) color map for α-phase of Ti. The rendering on the left is a result of the conventional three-dimensional SIRT algorithm (10 iterations), while the one on the right has been obtained from a six-dimensional total variation (6DTV) regularization over $\mathbb{X}^6$.

Some of the most evident errors of the three dimensional algorithm, when compared to the EBSD reconstruction, are indicated through red circles in Figure 6.3.1b. Area 1 is a region where the purple grain extends more than it should, growing from top and touching the pink one. The green grain on the right-hand side of area 1 does not actually grow until the very surface. The same problem is encountered in area 2, where the two triple junctions have not been reconstructed properly. Moreover, the red grain which is supposed to grow at the surface in area 3 has not been entirely reconstructed, since it is not visible in the three-dimensional reconstruction.

The improvements obtained by sampling the orientation space are shown in Figure 6.3.1d and are very clear. The junctions in area 2 are resolved better now, and a red grain appears in area 3, which limits the extension of the violet nearby grain. Area 1 is maybe the most critical, and more efforts must be put into the reconstruction of the green grain, in order to improve the accuracy of the three-dimensional shape reconstruction. Part of the reason for the problem may be a non perfect alignment between the reconstructed volume and the absorption volume which is superimposed in order to crop the surface grains and create sharper boundaries. The misaligned mask calculated from the absorption volume may have cut the reconstructed volume a few pixels inside the sample, a distance sufficient to change details of the topology of grain neighborhoods.

However, it is clear that the six-dimensional reconstruction is necessary to recover the correct shape and orientation of clusters of grains, especially near grain boundaries, where deformations are stronger than in the bulk.

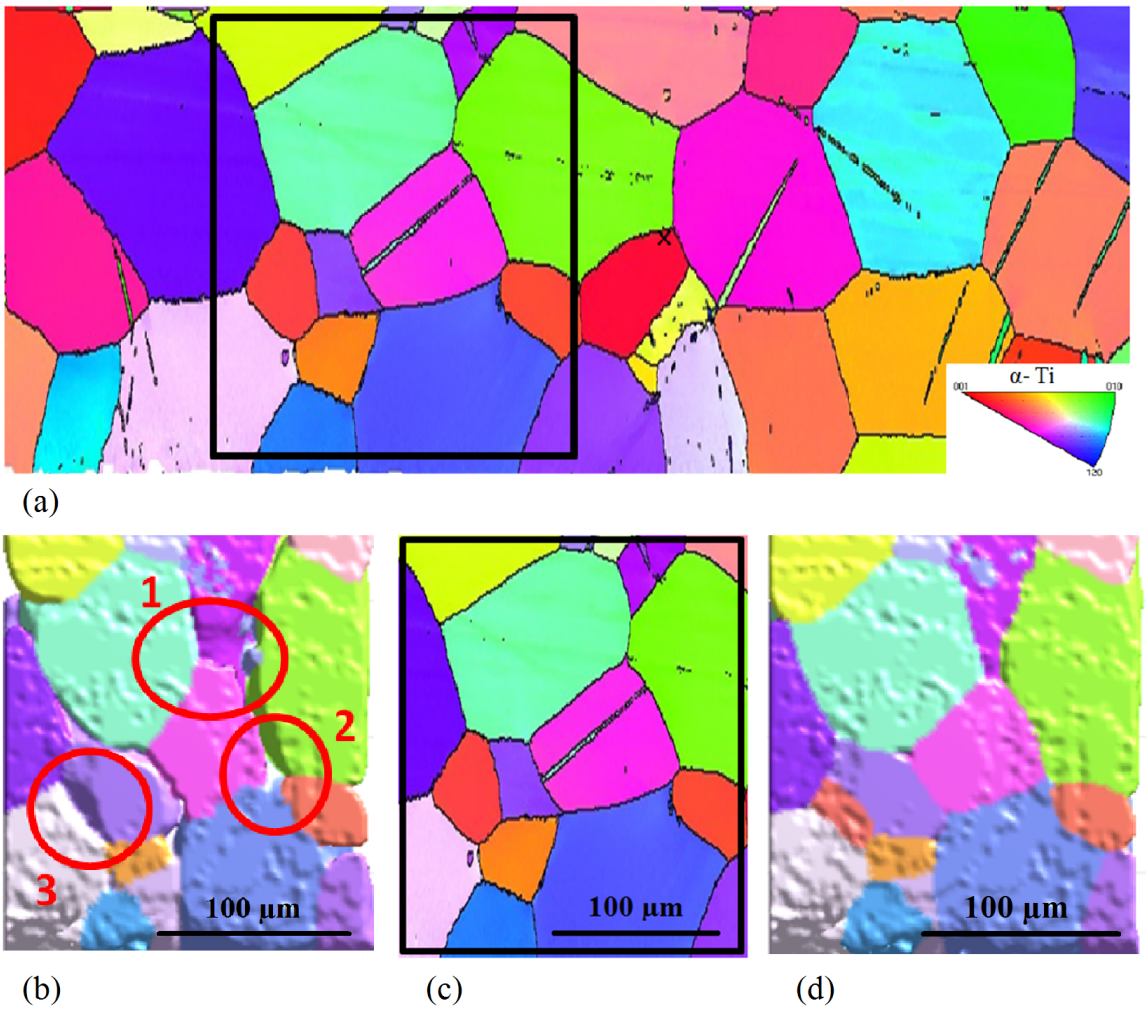

Figure 6.3.1: Comparison between an EBSD grain map and two DCT reconstructions of a Ti sample. (a) is the EBSD grain map, (b) is a rendering of the volume reconstructed with a three-dimensional SIRT algorithm, (c) is the selected region from EBSD reconstruction, and (d) is a rendering of the volume reconstructed with the 6DTV approach. The red circles in (b) indicate regions where the 6D algorithm performed clearly better than the 3D SIRT approach.

This is more evident in Figure 6.3.2, which shows some properties of the green grain and of the pink one (Figure 6.3.1d) in orientation space.

On the left column, an isosurface for the *orientation distribution function* (ODF) has been calculated. The ODF of a grain is defined as the fraction of volume elements

in that grain with a certain orientation g [43]:

$$ODF(\mathbf{g}) = \frac{1}{V}\frac{dV(\mathbf{g})}{d\mathbf{g}}$$

where each orientation has been identified using the three rotation angle around the three axes X, Y, and Z. So, each point in this space describes a transformation from the sample's reference system into the crystallographic frame of each volume element of the grain. It should be noted that, if the grains were perfect crystals, one single point, i.e., the average orientation of the grain (indicated as a red point in Figure 6.3.2), would be present in the ODF.

On the right column, for the grain slices visible in Figure 6.3.1c, the *intra-granular misorientation* (IGM) has been plotted. The IGM is a scalar depending on the deviations of each volume element from the average orientation in the grain. For instance, in a grain containing N volume elements, each of them with orientation $\mathbf{r}_i$ identified using a three-dimensional Rodrigues vector and with average orientation $\mathbf{R}$, one would have:

$$IGM = \sqrt{\sum_{i=1}^{N} |\,\mathbf{r}_i - \mathbf{R}\,|^2}$$

In order to get the IGM in degrees, it is then sufficient to recall the definition of Rodrigues vector, whose magnitude is:

$$r = tan\left(\frac{\theta}{2}\right)$$

from which one has:

$$\theta = 2\,atan\,(r)$$

It becomes clear in these cases that the three-dimensional reconstruction starts to fail when misorientations come close to $\sim 1°$. One can see that the regions of the two grains with the highest IGM are badly reconstructed by the three-dimensional algorithm. These boundaries do not extend until the rendered surface, because they lack a number of orientations.

An important reason why this study was conducted was to find how many twins could be indexed and reconstructed. In the reconstructed region of the surface, one out of two twin features is visible, that is, in the violet elongated grain. Further

investigation would be required to assess the best conditions for the reconstruction of the biggest twin structure visible in the pink central grain. A possible extension of the reconstruction process would include the expected twin variants as additional orientations to be sampled.

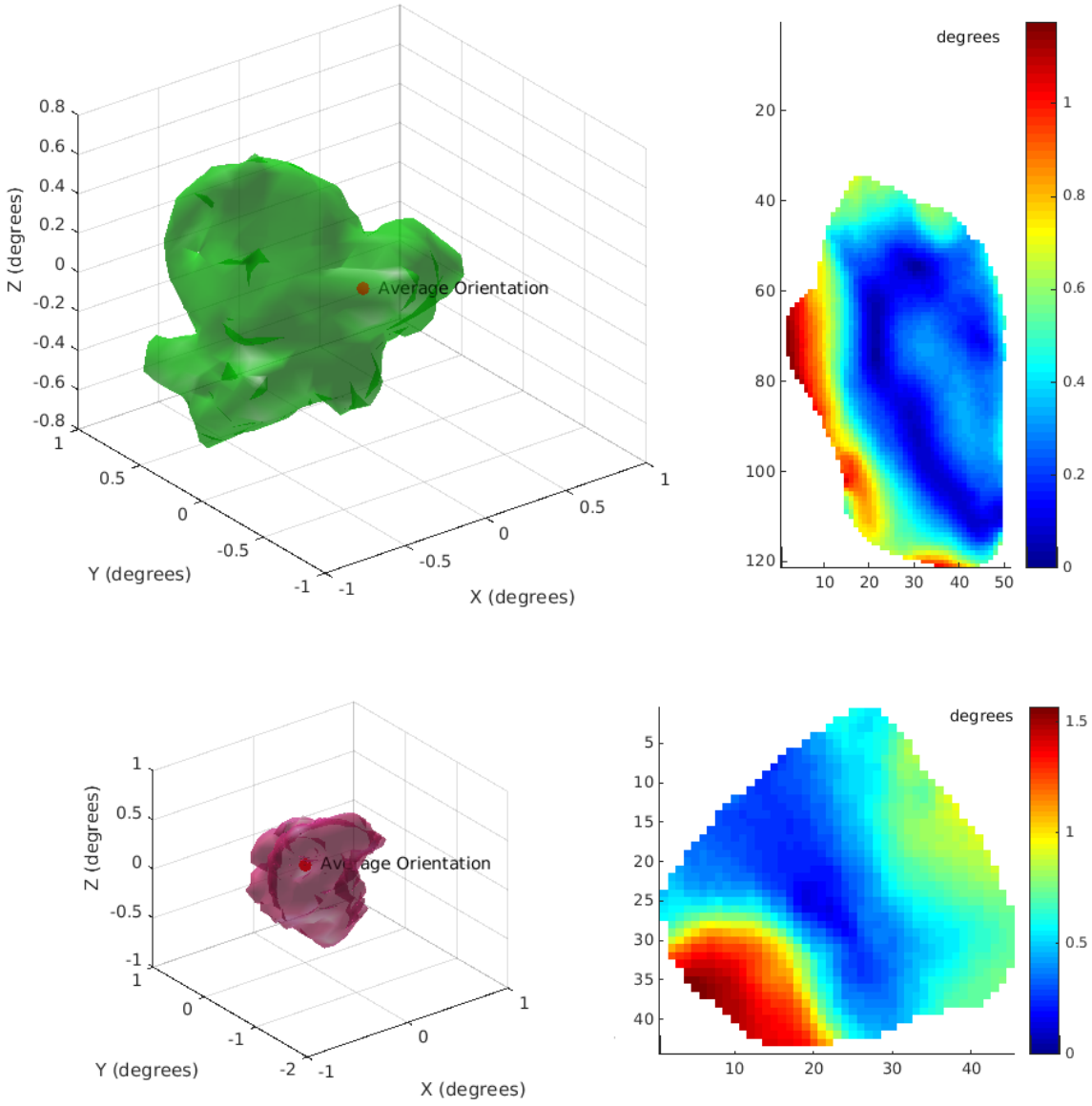

Figure 6.3.2: Properties of two grains in orientation space. The left column shows their ODF centered on the average orientation, the axes corresponding to rotation angles around X, Y, and Z sample axes. The isosurfaces shown are at 2.5 % of the maximum intensity variation. On the right, IGM is plotted for each volume element in the surface slices of the grains shown in Figure 6.3.1 (1 voxel = 1.4 μm).

6.4 Second way of validation: Imaging of the deformation state of a deformed sample

The second route for the validation of the six-dimensional algorithm basically followed these steps:

1. A DCT experiment was performed on a magnesium sample with full beam illumination and horizontal rotation axis. The term *Experiment 1* will be used to refer to it in the rest of the chapter;

2. The six-dimensional algorithm was run, so that a reconstruction in both real and orientation space is obtained;

3. Based on the results of the six-dimensional reconstruction, diffraction images corresponding to a *pinhole* and *section topography* experiment were *simulated*. The term *Experiment 2* will be used to refer to this experiment in the rest of the chapter;

4. Simulated results were compared with experimental results of *Experiment 2*.

6.4.1 The magnesium sample

Magnesium is a hcp metal at room temperature which is the third most commonly used structural metal, following steel and aluminum. Its fields of use range from agricultural, chemical and construction industries, to automotive and manufacturing of electronic devices. Among its several attractive engineering properties, its alloys can endure elevated temperatures up to 400 °C.

As for the Ti-4Al sample, this Mg sample (an extruded Mg3% Al1% Zn sample) was prepared in order to study deformation twinning, and was also preferred because of its low absorption coefficient ($\mu/\rho \approx 6.358$ cm^2/g at 15 keV) if compared to other structural metals.

6.4.2 Experimental setups and acquisition geometries

Both *Experiment 1* and *Experiment 2* were performed at ID18 beamline at ESRF, where an undulator source and a Si(111) double-crystal Bragg monochromator provided a 14.4 keV X-ray beam with a relative energy bandwidth of 10^{-4}. In contrast to conventional tomography experiments, the sample rotated around a horizontal axis perpendicular to the incoming beam.

In *Experiment 1*, the sample was illuminated by a full beam with dimensions 1.04 mm $\times$ 0.85 mm (horizontal $\times$ vertical) defined by slits. The detector was an ATMEL FReLoN camera containing 2048 $\times$ 2048 pixels with 3.5 μm effective pixel size mounted in the conventional DCT geometry, that is, centered in the direct beam and at a distance of $\sim$ 4.19 mm from the sample. A scan was performed over a 360° continuous rotation with 0.05° rotation steps.

In *Experiment 2*, an absorbing mask was used to create either:

- a line beam profile illuminating a 7 μm-thick slice of the sample, parallel to the rotation axis, or
- a periodic array of pencil beams with period 50 μm and individual sections of about 7 μm $\times$ 7 μm.

Diffraction signals were recorded by a FReLoN E2v camera containing 2048 $\times$ 2048 pixels with 1.5 μm effective pixel size mounted $\sim$ 2.34 mm above the sample. Three arbitrary reflections of the biggest grain were selected, and seven pencil beam scans were performed for each reflection and its corresponding Friedel pair. Each image was integrated over a ω range of 1.5°, covering the angular range of the reflection curve. The seven pencil beam scans were needed to illuminate the whole slice by shifting the grid along the rotation axis direction.

Line beam scanning with vertical detector

The acquisition geometry exploited in the *Experiment 2* is shown in Figures 6.4.1 and 6.4.2 and its aim was to reconstruct deformed microstructured materials with μm spatial resolution. Working at lower beam energies opens new interesting possibilities for acquisition geometries. At energies below $\sim$ 25 keV, one can detect diffraction cones with higher opening angles. Though, beams impinging on the detector far from normal incidence are imaged with worse resolution due to parallax effects on the scintillator screen. In addition, diffraction images suffer from compression along vertical direction if intercepted on a forward detector. As a result, one would prefer the detector to be positioned almost perpendicular to diffracted beams. Moreover, the linear polarization of the synchrotron beam results in a $cos^2(2\theta)$ dependence of the diffracted intensity when working in the conventional tomography geometry, i.e., with forward detector and vertical rotation axis. If one wants to detect spots at $2\theta \approx 90°$, it is necessary to switch to the vertical acquisition plane, and consequently to use a horizontal rotation axis.

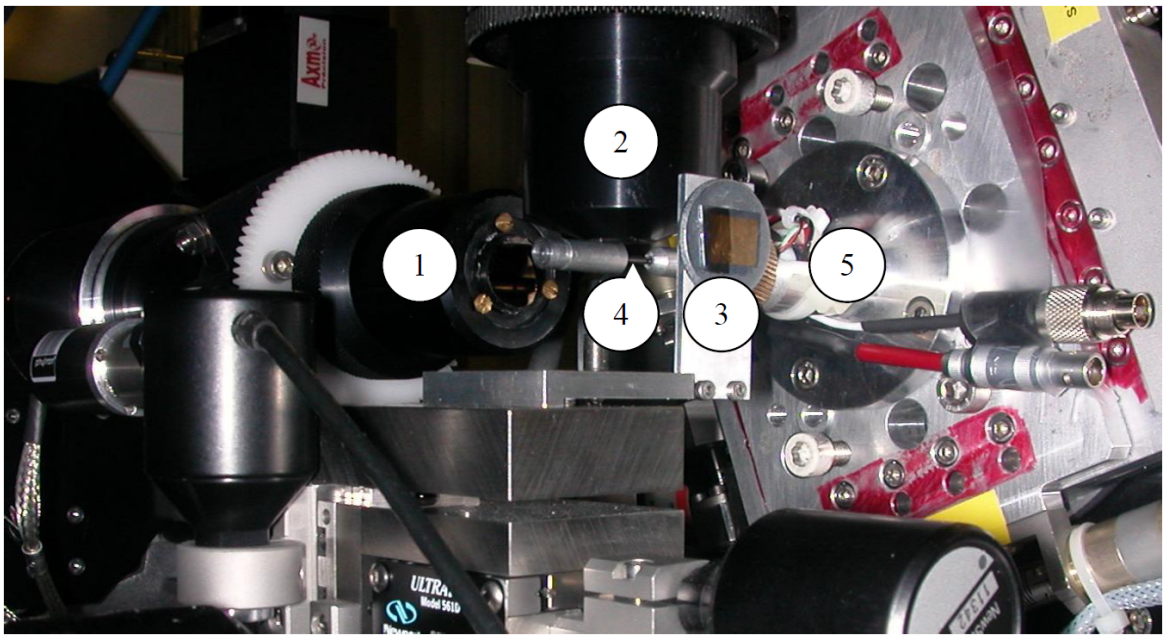

Figure 6.4.1: Experimental setup of optimized 3DXRD acquisition geometry. The beam comes from the right and the direct and forward diffracted beams are recorded on a high-resolution detector system (1). Beams diffracted at angles close to 90° are recorded on a second high-resolution detector system (2), positioned vertically above the sample. The beam profile can be changed from extended (2D) to line beam (1D) by insertion and vertical scanning of a micro slit (3) aligned parallel to the rotation axis. The sample (4) is mounted in a miniature compression rig (5), positioned on the axis of a precision rotation table in horizontal configuration. [33]

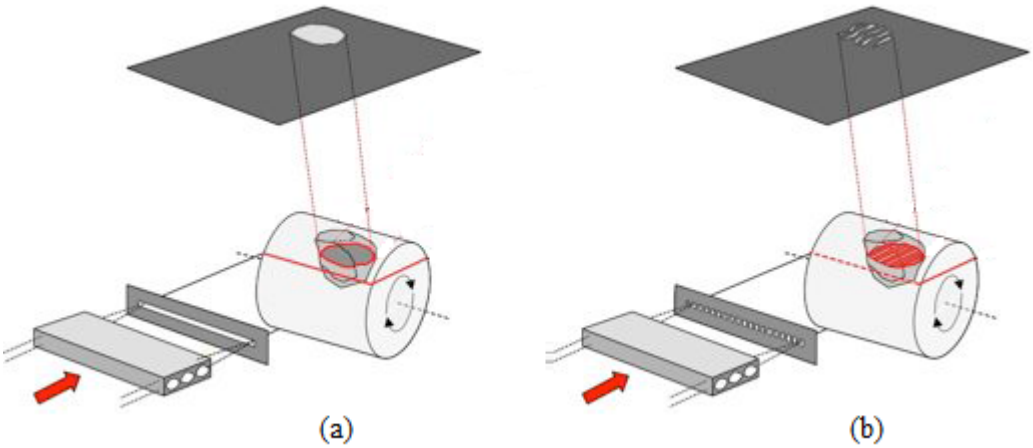

Figure 6.4.2: Illustration of the vertical acquisition geometry with (a) line beam (1D) and (b) pencil beam (0D) illumination mode. [33]

Placing a detector vertically above the sample offers several advantages:

- Optimum spatial resolution. Compared to the conventional 3DXRD geometry with line beam illumination, now horizontal cross-sections of the grains are imaged, and do not suffer from the compression of the vertical direction as observed on the forward scattering detector. As already mentioned, spatial resolution is improved also by the reduction of parallax effects in the scintillator. The three-dimensional grain volume is assembled by stacking the individually reconstructed layers.

- Better azimuthal angle sensitivity. The distortion of projection images due to orientation gradients inside a grain is more pronounced at high diffraction angles. Let D be the distance between the sample and the detector and θ the Bragg angle of a given diffracted beam. A change in the azimuthal angle $\triangle\eta$ of the diffracted beam will result in a displacement $\triangle u^{(forward)} \approx D \triangle\eta \, tan\,(2\theta)$ on the forward detector and $\triangle u^{(vertical)} \approx D \triangle\eta$ on the vertical detector. A typical value for the maximum 2θ scattering angle intercepted by the forward detector is about 20°, resulting in a factor $\gtrsim 1 \,/\, tan\,(20°) \approx 3$ improvement in angular resolution.

- Improved elastic strain resolution. If changes in the lattice spacing d can not be neglected, a change in the diffraction angle of $\triangle\theta = -(\triangle d/d)\, tan\,\theta$ is expected. Compared to the forward scattering geometry, one can gain a factor 5 improvement in elastic strain sensitivity.

- Reduced background. Since only diffracted beams impinge on the detector, problems associated with interaction of the strong direct beam with the scintillator screen are avoided.

- One can still collect Friedel pairs of diffraction spots, and have easy access to the directions of the diffracted beams.

- In addition, using the line or pencil beam illumination helps reduce the convolution of diffraction data.

Pencil beam scanning with vertical detector

In order to have a better access to local diffraction vectors, the dimensionality of the beam can be further reduced.

Scans were also performed in the geometry depicted in Figure 6.4.2b. Here the incoming beam is structured into an array of pencil beams. The analysis of the lateral

displacement of diffracted vectors recorded on a 90° vertical detector provides access to local variations in η angle. Compared to the line beam illumination mode, two (ω, η) out of three diffraction angles can be determined from the analysis of the stripe pattern.

The interest in these experimental variants of three-dimensional orientation microscopy is twofold. First, accessing two out of three diffraction angles is mandatory for characterization of all nine components of the displacement gradient tensor (three rotation components and six components for elastic strain). In order to determine all of its components, all three diffraction angles would have to be measured for at least three linearly independent diffraction vectors. Knowledge of local η diffraction angle is a strong additional constraint which can be applied to iterative reconstruction algorithms, thus improving the chance of finding the correct solution.

Secondly, measurement of local diffraction vectors from isolated diffraction volumes will serve as a verification and test case for the establishment of advanced reconstruction algorithms applicable to fast acquisition schemes like two-dimensional illumination.This is the principle which was followed in this work. Moreover, supposing negligible elastic strain, access to local ω and η diffraction angles is enough to assign orientations to individual voxels in a deterministic way.

6.4.3 Processing and six-dimensional reconstruction

Scans acquired with full beam illumination and forward detector geometry were processed with the conventional procedure discussed in chapter 4.

A binning of the stack of raw images by a factor 2 in both coordinates on the detector and by a factor 4 in the ω dimension was performed to reduce computational time and to be able to allow for an appropriate sampling in orientation space.

1659 diffraction spots were segmented, and 175 Friedel pairs were processed on the forward detector. 12 grains were indexed in order to identify three pairs of reflections from the same grain which could be acquired in the experiment with the optimized acquisition geometry.

The six-dimensional reconstruction was performed with particular focus on the largest grain. Two different volumes of the orientation space were chosen for the sampling. The first one is large enough to envelop all the orientations in the grain. In the second case, a reduced orientation space volume was sampled, whilst keeping the number of orientations constant, thereby increasing the sampling frequency and try to resolve finer details. Results will be shown and discussed in section 6.4.5.

6.4.4 Validation procedure

In order to simulate the line beam and pencil beam patterns on the vertical detector, two steps are involved, as indicated in Figure 6.4.3. First, the illumination for each voxel for each considered reflection is needed. This is obtained by *back-projecting* the intensity distribution of the mask (either the line mask or the mask giving the pencil profile) from the in-line detector into the sample volume, for each of the rotation angles corresponding to the reflections one wants to simulate. The ASTRA Tomography Toolbox (Palenstijn *et al*., 2011) was used to compute back-projections related to three chosen reflections. This step has been indicated with number 1 in Figure 6.4.3, and more details can be found in section A.2 of appendix **??**, containing the code developed and used for the computation of active voxels.

The next step is to *forward-project* the intercepted voxels on the vertical detector (step number 2 in Figure 6.4.3), thus creating a simulated diffraction pattern which is finally compared to experimental observations. The forward-projection was performed using the same settings employed in *Experiment 2* and a modification of an existing projection code designed by P. Reischig.

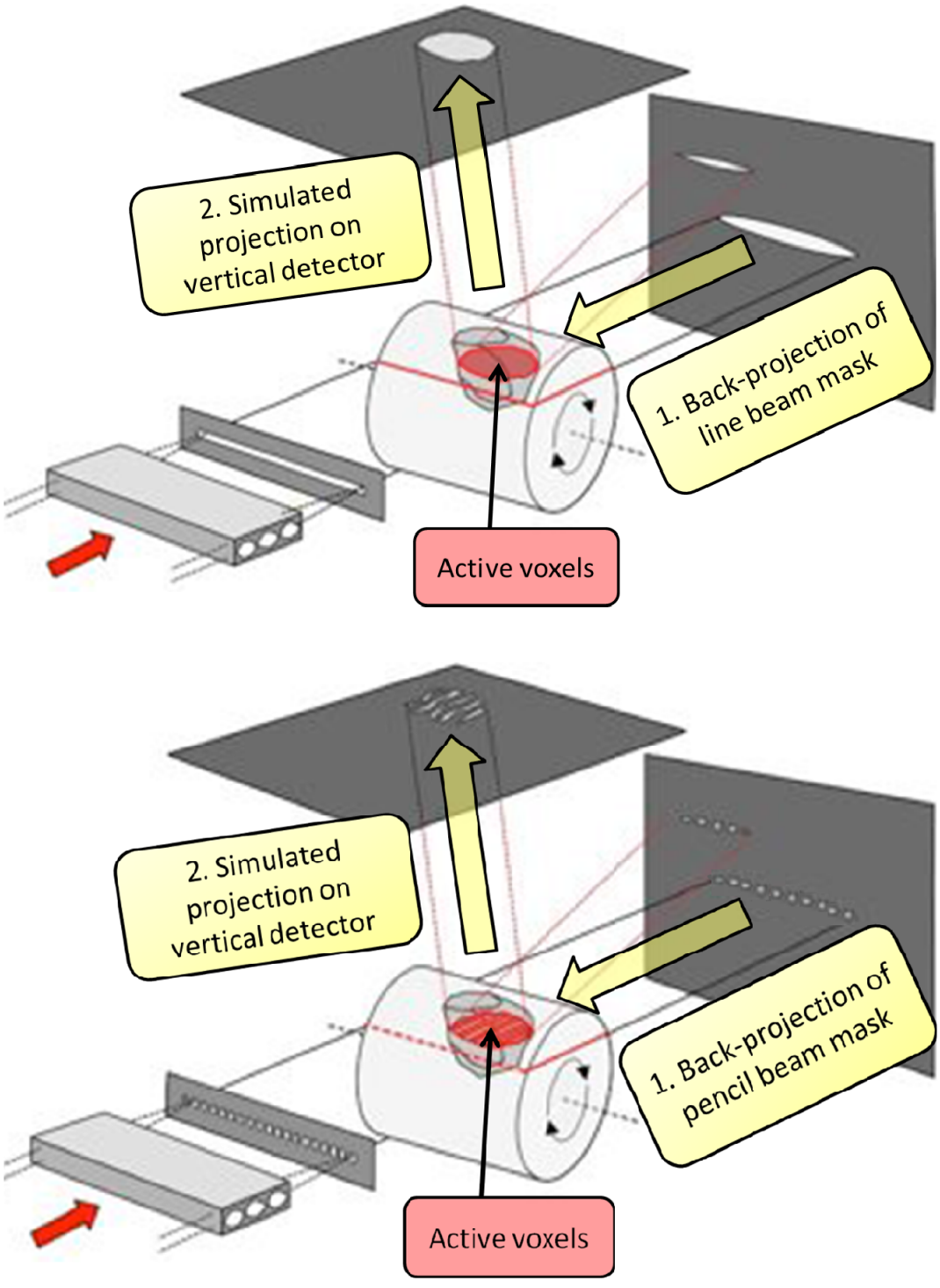

Figure 6.4.3: Steps involved in the simulation of diffraction patterns from line beam (top) and pencil beam (bottom) illumination on a vertical detector. The active voxels, i.e., voxels with some diffracting power, are obtained by back-projecting the illumination profile of the mask from the forward detector into the sample volume (step 1). These voxels are then forward-projected on the vertical detector (step 2).

6.4.5 Results and discussion

The three reflections which were chosen for the comparison correspond to rotation angles of 1.8°, 181.8°, and 63.8°, the first and the second one making a Friedel pair.

Two reconstructions were performed with a 6DTV regularization over $\mathbb{X}^6$. The first one considered a volume in orientation space of size 10.5° × 8.5° × 5.0° sampled with 17 × 14 × 8 = 1904 orientations, corresponding to one orientation every 0.6° in each dimension. Such a choice was made in order to include all the orientations present in the grain, as one can see in Figure 6.4.4, where an isosurface of the ODF is shown in three plots. The presence of weak tails in the ODF should be noted, which may be caused by the cutting process by electric discharge machining, leading to surfaces more deformed than the bulk.

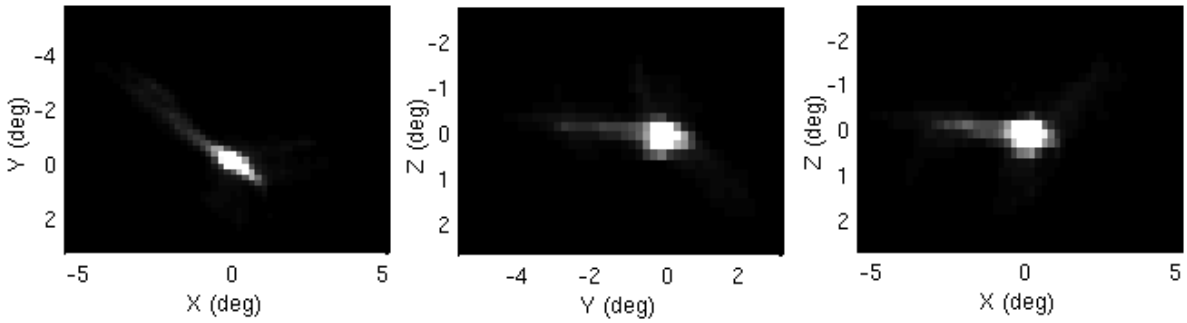

Figure 6.4.4: Isosurface of the ODF at 2.25 % of the maximum intensity variation for the largest grain in the sample, using an orientation volume enclosing all the orientations.

Figures 6.4.5, 6.4.6, and 6.4.7 show corresponding slices for the three reflections as experimentally observed and theoretically simulated. Simulated line beam projections reproduce the shape of experimental blobs, as well as the most intense losses in intensity due to twins traversing the grain and scattering at different rotation angles. Some intensity peaks are also reconstructed, as one can especially see on the left-hand side of the blob in Figure 6.4.7.

From a comparison between a line beam projection and its related pencil beam projection one can infer that areas with high / low intensity correspond to regions with closer / larger spacing of pencil beams, respectively. The stripe pattern of the blob in Figure 6.4.7 presents several trends which can be recognized in the experimental image: the strong gradient of stripes towards left on top of the blob; most lines breaking in the same positions; and the group of very close lines leading to an increase in intensity in the corresponding line beam projection. As a consequence,

line beam projections look similar as well.

On the other hand, a glance at the stripe patterns of the two other blobs reveals the limits of the reconstruction. It is not possible to see convincing common trends. In particular, the twin diagonally traversing the blob in Figure 6.4.5 is visible neither in the line beam simulated projection nor in the pencil beam one.

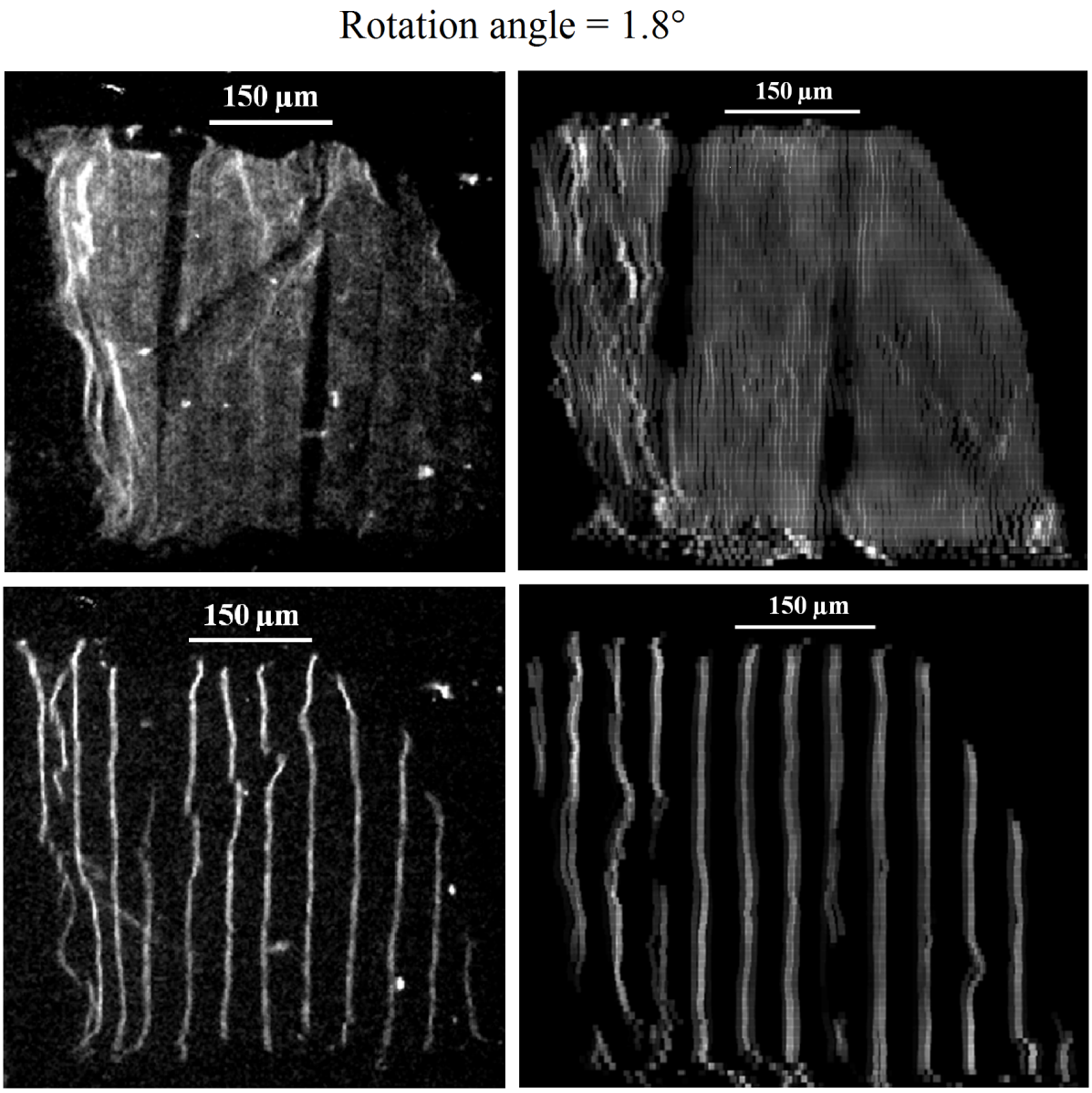

Figure 6.4.5: Comparison between experimental (left column) and simulated (right column) diffraction images with line beam (top) and pencil beam (bottom) illumination for the reflection at ω = 1.8°.

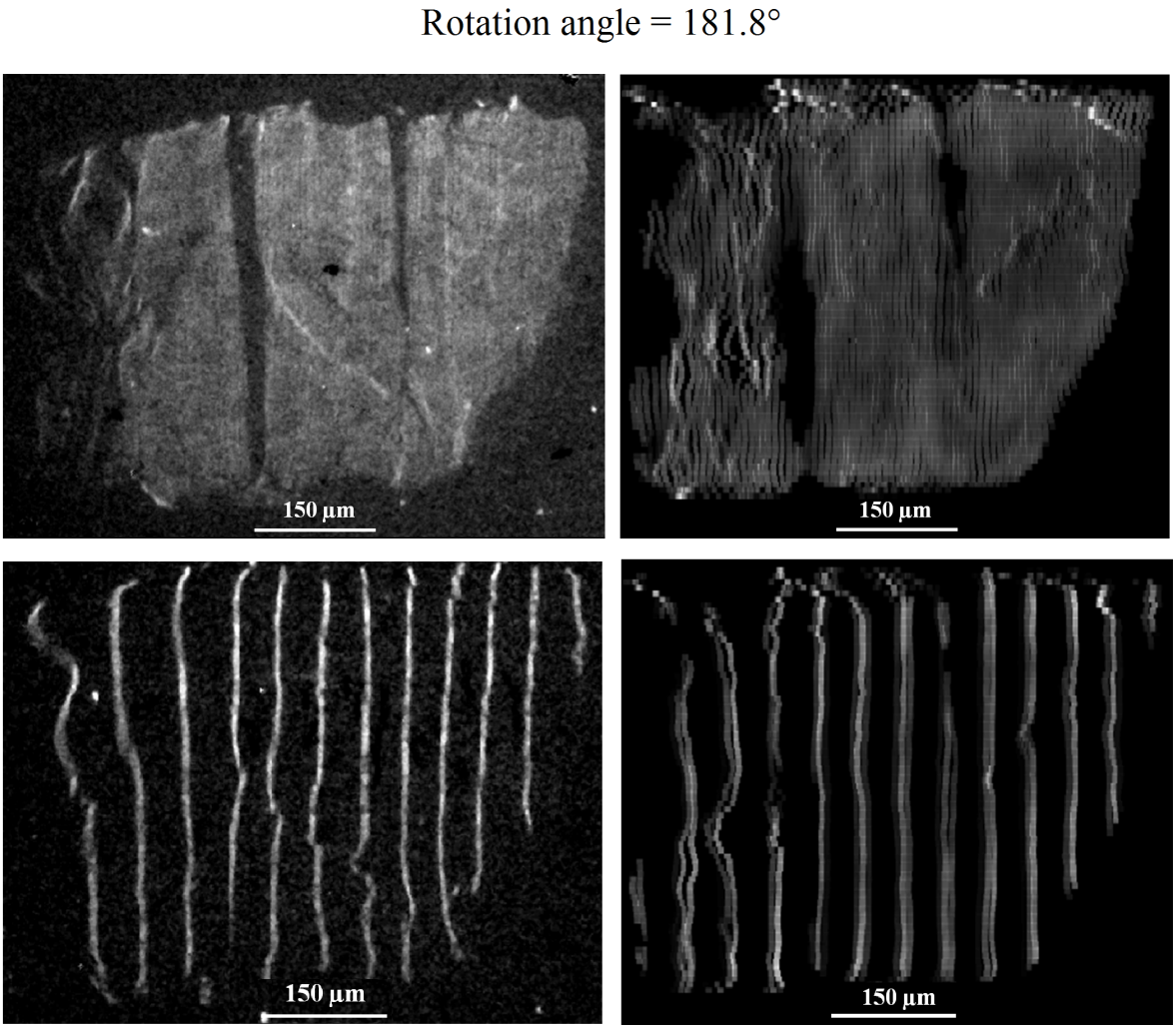

Figure 6.4.6: Comparison between experimental (left column) and simulated (right column) diffraction images with line beam (top) and pencil beam (bottom) illumination for the reflection at ω = 181.8°.

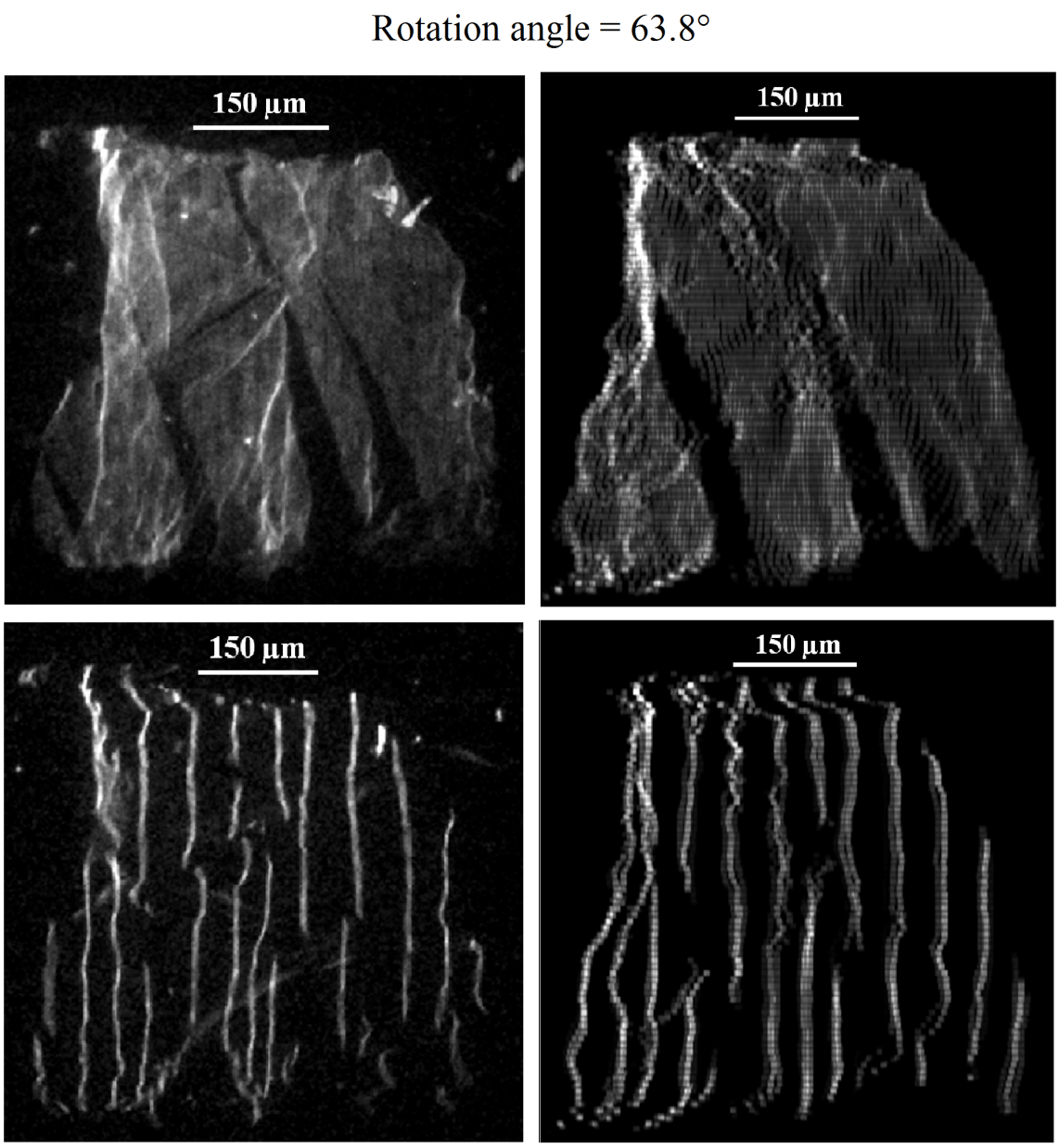

Figure 6.4.7: Comparison between experimental (left column) and simulated (right column) diffraction images with line beam (top) and pencil beam (bottom) illumination for the reflection at ω = 63.8°.

In order to hope for a better agreement between experimental data and simulations, a finer sampling of orientation space would be needed. This can be easily understood by considering that, in the current optimized acquisition geometry, if a projected stripe is so deflected because of deformation that it crosses one adjacent

stripe at 50 μm distance, a misorientation of

$$atan\left(\frac{0.05\,mm}{2.34\,mm}\right) \approx 1.22°$$

is observed. The resolution which was used in this first reconstruction is 0.6° in each dimension of the orientation space, implying that only imaging of strong deformations (for which one stripe reduces its distance from the next one by a factor of 2) can be reliably accounted for. This can partly explain why it was impossible to reconstruct most features that were experimentally observed. Moreover, the use of the TV minimization functional favors solutions with constant intensity. The presence of twins can be expected to disturb the algorithm at these locations.

At the present time, memory constraints prevents from improving resolution in orientation space. Therefore, a different attempt was made by shrinking the orientation space to about 1/8 of its previous volume. Using a 5° $\times$ 4° $\times$ 2° orientation volume sampled by 18, 15, and 7 orientations in each dimension (1890 total orientations), one can reach a resolution of $\sim$ 0.28°, thus gaining a factor 2 improvement. In Figure 6.4.8, the results from this second reconstruction are compared to those from the first one and to experimental data.

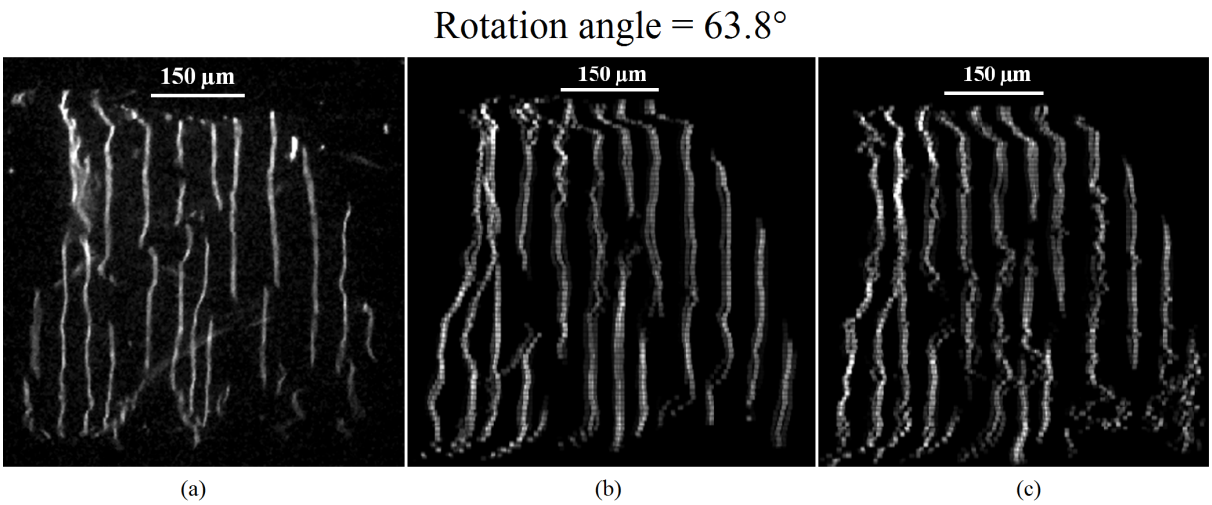

Figure 6.4.8: Comparison between experimental projection (a) and simulated ones with: (b) a resolution in orientation space of 0.6° which encloses all the orientations in the grain, or (c) a resolution in orientation space of 0.28° which does not enclose all the orientations in the grain. The same reflection as in Figure 6.4.7 was chosen.

Considering a smaller orientation volume implies that some of the intensity tails

in Figure 6.4.4 are cut out. From a mathematical point of view, this results in:

- a loss in the number of equations in the linear system $\mathbf{A}\,\mathrm{x} = \mathrm{b}$;
- an increase of the condition number of the forward-projection matrix $\mathbf{A}$, which means that the rate at which the solution x changes with respect to a change in b increases.

As one could expect from the above discussion, reducing the size of orientation space leads to a noisier reconstruction, and relevant improvements due to the enhanced resolution are not visible yet.

Chapter 7

CONCLUSIONS AND PERSPECTIVES

The aim of this thesis was to make progress in the reconstruction of polycrystalline samples with the technique known as diffraction contrast tomography (DCT). With the introduction of the Friedel pairs approach, a processing routine for DCT data sets provides access to the shape, orientation and elastic strain state of grains in polycrystalline samples containing up to one thousand grains and more.

During the last months, new and more robust algorithms which could deal with different non ideal situations were suggested and tested.

Firstly, a study on the possibility to perform a successful matching of Friedel pairs when the rotation axis is not perpendicular to the direction of the incident beam was conducted. The interest in such a case was stimulated by the review of unpublished work by Qiru Yi *et al.* An algorithm applicable in this situation would allow to recover a number of experimental data sets, suffering from this type of misalignment. Provided the grain position was known, the problem would be easy to solve from a mathematical point of view. In practice, one has to cope with the unknown position of the scattering grain giving rise to an observed diffraction spot. A simple solution was suggested, allowing for the largest tolerance interval compatible with the size of the sample. However, this trivial attempt did not lead to significant improvements in the matching algorithm, and further developments would be required in order to determine the Friedel pair of an arbitrary diffraction spot with more precision. Within this approach, having a sample whose projection on the detector is much smaller than the detector size would help reducing this uncertainty. Yet, another possible solution was suggested as a future perspective.

Most of the time was spent on a very promising and recently developed algo-

rithm by Nicola Viganò (ESRF) allowing for the reconstruction of local orientations in grains. It can overcome one of the main limitations in the previous DCT reconstruction approach, which progressively fails when intra-granular misorientations come close to or exceed 1°, thus preventing a whole class of materials and microstructures from being imaged with this technique. In this framework, two validation procedures were suggested and applied.

The first validation consisted of the reconstruction of a deformed Ti alloy sample by means of the new six-dimensional algorithm. Considerable effort was put in producing a grain map matching another grain map of the same sample obtained through electron backscatter diffraction (EBSD). A comparison with a reconstruction obtained with the previous algorithm neglecting misorientations revealed significant improvements in the determination of the microstructure of polycrystals at early stages of deformation.

The second validation study was performed on a large - grained Mg alloy sample, displaying larger values of intra-granular orientation spread ($\sim 2°$). After reconstructing the deformation and intensity volume of the sample, these pieces of information were used to simulate the diffraction patterns corresponding to a pinhole and section topography experiment conducted on the same sample. Simulated projections were finally compared with experimental observations.

The described procedures allow to draw the following conclusions about the new algorithm:

- Including the symmetry related twin variants to the sampled orientations would help the six-dimensional reconstruction to reproduce these important features appearing during plastic deformation of metals with hexagonal lattice structure. This was clear from both the validation tests.

- Despite the huge potentialities of this algorithm, memory constraints set limits to the computation of a large number of orientations and/or big grain volumes.

- Its performances, which now have been tested both on synthetic and experimental data sets, appear very promising, since they allow for an unprecedented sub-grain resolution. This was especially confirmed in section 6.3, containing a comparison with the previous three-dimensional approach.

For these reasons, one can anticipate a new exciting era in the field of three-dimensional materials science based on X-ray diffraction imaging techniques.

References

[1] J. Als-Nielsen, and D. McMorrow. *Elements of Modern X-ray Physics, 2nd Edition*. Wiley, 2011.

[2] N. W. Ashcroft, and N. D. Mermin. *Solid State Physics*. Saunders, 1976.

[3] The GISAXS Community Website: www.gisaxs.com.

[4] R. Dejus, and M. Sanchez del Rio. *Xop: A graphical user interface for spectral calculations and X-ray optics utilities*. Rev. Sci. Instr., 67(3356), 1996.

[5] P. Cloetens, M. Pateyron-Salomè, J.-Y. Buffière, G. Peix, J. Baruchel, F. Peyrin, and M. Schlenker. *Observation of microstructure and damage in materials by phase sensitive radiography and tomography*. J. Appl. Phys., 81(9):5878-5886, 1997.

[6] D. M. Paganin. *Coherent X-ray Optics*, *volume 6 of Oxford Series on Synchrotron Radiation*. Oxford University Press, Oxford, 2006.

[7] D. M. Paganin, S. C. Mayo, T. E. Guereyev, P. R. Miller, and S. W. Wilkins. *Simultaneous phase and amplitude extraction from a single defocused image of a homogeneous object*. J. Microsc., 206:33-40, 2002.

[8] J. P. Guigay, M. Langer, R. Boistel, and P. Cloetens. *Mixed constrast transfer and transport of intensity approach for phase retrieval in the Fresnel region*. Opt. Lett., 32:1617-1619, 2007.

[9] A. Kak, and M. Slaney. *Principles of Computerized Imaging*. IEEE press, 1988.

[10] G. Herman. *Fundamentals of Computerized Tomography*. Advances in Pattern Recognition. Springer, 2009.

[11] Y. De Witte. *Improved and practically feasible reconstruction methods for high resolution X-ray tomography*. Universiteit Gent, Faculteit Wetenschappen, 2010.

[12] S. Kaczmarz. *Angenaherte auflosung von systemen linearer gleichungen*. Bull. Acad. Pol. Sci. Lett. A, vol. 6-8A, pp.355-357, 1937.

[13] K. Tanabe. *Projection method for solving a singular system*. Numer. Math., vol. 17, pp. 203-214, 1971.

[14] R. Baruzzo, A. Stevanato, G. V. Lamanna, G. Vaughan, J. Wright, A. Bytchkov, C. Curfs, C. Gundlach, M. Rossat, and T. Buslaps. *Laue –Laue monochromator for ID11 beamline at ESRF.* 2008.

[15] Image available at ESRF website:
http://www.esrf.eu/home/UsersAndScience/Experiments/StructMaterials/ID11/technical-overview.html .

[16] S. Corde, K. Ta Phuoc, G. Lambert, R. Fitour, V. Malka, and A. Rousse. *Femtosecond X-rays from laser-plasma accelerators.* Rev. Mod. Phys., 85, 2013.

[17] Image available at Wikipedia, the free enciclopedia website:
http://en.wikipedia.org/wiki/Undulator .

[18] Image courtesy of ESRF ID group & Technical services. *Status of In-Vacuum undulators at ESRF.*

[19] P. Suortti, T. Buslaps, V. Honkimaki, M. Kretzschmer, M. Renier, and A. Schukla. *Monochromators for High-Energy Synchrotron Radiation.* Zeitschrift für Physikalische Chemie, 215, 11, 1419-1435, 2001.

[20] S. D. Shastri, K. Fezzaa, A. Mashayechi, W.-K. Lee, P. B. Fernandez, and P. L. Lee. *Cryogenically cooled bent double-Laue monochromator for high-energy undulator X-rays (50±200 keV).* J. Synch. Rad. 9, 317-322, 2002.

[21] A. Stevanato. *Laue-Laue Monochromator for ID11 Beamline at ESRF.* Presentation 10-13 June 2008, Saskatoon, Canada.

[22] G. B. M. Vaughan, J. P. Wright, A. Bytchkov, M. Rossat, H. Gleyzolle, I. Snigireva, and A. Snigirev. *X-ray transfocators: focusing devices based on compound refractive lenses.* J. Synch. Rad. 18, 125-133, 2011.

[23] S. Matsuyama, and H. Yumoto. *Textbook for hard X-ray focusing with Kirkpatrick-Baez optics.* 2009.

[24] J. R. Helliwell, and P. M. Rentzepis. *Time-resolved Diffraction.* Clarendon Press, Oxford Series on Synchrotron Radiation 2, 1997.

[25] B. E. Warren. *X-ray Diffraction.* Addison-Wesley Pub. Co., 1969.

[26] Image available at the Università degli Studi di Padova website: http://www.chimica.unipd.it/federico.rastrelli/pubblica/research.html .

[27] H. F. Poulsen. *Three-Dimensional X-ray Diffraction Microscopy.* Springer-Verlag Berlin Heidelberg, 2004.

[28] S. Van Boxel, S. Schmidt, W. Ludwig, Y. Zhang, H. Sørensen, W. Pantleon, and D. Juul Jensen. *Monitoring grain boundary movement during recrystallization using topo-tomography.* In #1st Risø Intrenational Symposium on Materials Science: Challenges in Materials Science and possibilities in 3D and 4D characterization techniques, volume 31, pages available at https://hal.archives-ouvertes.fr/hal-00534883/document .

[29] W. Ludwig, E. M. Lauridsen, Soeren Schmidt, H. F. Poulsen, and J. Baruchel. *High-resolution three-dimensional mapping of individual grains in polycrystals by topotomography*. J. Appl. Cryst. 40, 905-911, 2007.

[30] W. Ludwig, S. Schmidt, E. M. Lauridsen, and H. F. Poulsen. *X-ray diffraction contrast tomography: a novel technique for three-dimensional grain mapping of polycrystals. I. Direct beam case.* J. Appl. Cryst., 41, 302-309, 2008.

[31] G. Johnson, A. King, M. C. Honnicke, J. Marrow, and W. Ludwig. *X-ray diffraction contrast tomography: a novel technique for three-dimensional grain mapping of polycrystals. II. The combined case.* J. Appl. Cryst., 41, 310-318, 2008.

[32] P. Reischig, A. King, L. Nervo, N. Viganò, Y. Guilhem, W. J. Palenstijn, K. J. Batenburg, M. Preuss, and W. Ludwig. *Advances in X-ray diffraction contrast tomography: flexibility in the setup geometry and application to multiphase materials.* J. Appl. Cryst. 46, 297-311, 2013.

[33] W. Ludwig. *Combined use of synchrotron radiation X-ray imaging and diffraction techniques for the characterization of polycrystalline materials*, 2011.

[34] W. Ludwig, P. Reischig, A. King, M. Herbig, E. M. Lauridsen, G. Johnson, T. J. Marrow, and J. Y. Buffière. *Three-dimensional grain mapping by x-ray diffraction contrast tomography and the use of Friedel pairs in diffraction data analysis.* Rev. Sci. Instr. 80, 033905, 2009.

[35] O. Engler, and V. Randle. *Introduction to Texture Analysis. Macrotexture, Microtexture, and Orientation Mapping, 2nd Edition.* CRC Press, 2010.

[36] Wikipedia, the free enciclopedia website:
http://en.wikipedia.org/wiki/Rodrigues%27_rotation_formula .

[37] N. Viganò, W. Ludwig, K. J. Batenburg. *Reconstruction of local orientation in grains using a discrete representation of orientation space.* J. Appl. Cryst., 47, 1826-1840, 2014.

[38] R. M. Suter, D. Hennessy, C. Xiao, and U. Lienert. *Forward modeling method for microstructure reconstruction using x-ray diffraction microscopy: Single-crystal verification.* Rev. Sci. Instrum. 77, 123905, 2006.

[39] S. F. Li, and R. M. Suter. *Adaptive reconstruction method for three-dimensional orientation imaging.* J. Appl. Cryst. 46, 512-524, 2013.

[40] E. Candes, and J. Romberg. *Sparsity and Incoherence in Compressive Sampling.* Inverse Probl. 1-20, 2007.

[41] S. S. Chen, D. L. Donoho, and M. A. Saunders. *Atomic Decomposition by Basis Pursuit.* SIAM Rev., 43(1), 129–159, 2001.

[42] A. Chambolle, T. Pock. *A First-Order Primal-Dual Algorithm for Convex Problems with Applications to Imaging.* J. Math. Imaging Vis. 40, 120-145, 2011.

[43] Wikipedia, the free enciclopedia website:
http://en.wikipedia.org/wiki/Texture_(crystalline)#Orientation_distribution_function
.

Appendix A

MATLAB scripts

A.1 DCT with non-perpendicular rotation axis: modifications applied to the matching algorithm

The following is a simple script dealing with the issue of rotation axis non perpendicular to the beam direction (chapter 5). For each diffraction spot considered by the matching algorithm, a "conservative" prediction of the pair spot is computed as explained in section 5.2. The function has been added as part of the matching algorithm and gave the results discussed in chapter 5.

```
function [eta, pair_red] = gtPredictOmegaShiftNonPerpOpt(u, v, ...
    w, rot_axis_tilt)
% GTPREDICTOMEGASHIFTNONPERPOPT   Predicts at which omega displacement from
% 180 degrees Friedel pairs will be observed, in case of non-perpendicular
% rotation axis. Should improve pair candidates search in matching
% algorithm. Vectorised for speed (uses gtFedPredictOmegaMultiple).
%
%   gtPredictOmegaShiftNonPerpOpt(u, v, w, rot_axis_tilt)
%  ------------------------------------------------------------------------
%
%   INPUT
%       u, v, w       = centroidX, centroidY, centroidImage of one
%                       diffraction spot (1, n)
%       rot_axis_tilt = rotation axis tilt from z axis on XZ plane (deg)
%                       positive if rotation axis inclined towards detector
%                       only used if you haven't rotated labgeo by rotating
%                       needed vectors except from the rotation axis
%
%   OUTPUT:
```

```
20 %       eta           = angular position of diffraction spot on detector
21 %                       eta angle defined as in gtGeoEtaFromDiffVec
22 %       pair_red      = omega angle of the paired image
23
24 load parameters.mat
25 labgeo = parameters.labgeo;
26 samgeo = parameters.samgeo;
27 if (~isfield(labgeo, 'detorig'))
28     labgeo.detorig = gtGeoDetOrig(labgeo);
29 end
30
31 % Calculate rotation axis versor from the tilt
32 % Use the rot_axis_tilt variable if you haven't rotated labgeo yet, then
33 % uncomment next line and comment line 35
34 % rot_axis = [sind(rot_axis_tilt); 0; cosd(rot_axis_tilt)];
35 rot_axis = labgeo.rotdir';
36
37 % Convert from pixel units to mm
38 bb_lab = parameters.acq.bb * parameters.acq.pixelsize;
39
40 % Two-dimension sample bounding box on detector
41 % Sides of rectangular sample bounding box: (1) along u, (2) along v
42 bb_side(1) = bb_lab(3);
43 bb_side(2) = bb_lab(4);
44
45 % Find 4 vertices E, F, G, H
46 E = labgeo.detorig + bb_lab(1) * labgeo.detdiru + bb_lab(2) * labgeo.detdirv;
47 F = E + bb_side(1) * labgeo.detdiru;
48 G = F + bb_side(2) * labgeo.detdirv;
49 H = E + bb_side(2) * labgeo.detdirv;
50
51 % Three-dimension sample bounding box centered in the origin of samgeo
52 % The faces perpendicular to the incident beam are equal to the bb
53 % projected on the detector plane
54 % Farthest face from detector: upper-case letters
55 E = E - labgeo.beamdir * (E(1) - samgeo.orig(1) + bb_lab(3)*0.5);
56 F = F - labgeo.beamdir * (F(1) - samgeo.orig(1) + bb_lab(3)*0.5);
57 G = G - labgeo.beamdir * (G(1) - samgeo.orig(1) + bb_lab(3)*0.5);
58 H = H - labgeo.beamdir * (H(1) - samgeo.orig(1) + bb_lab(3)*0.5);
59 % Nearest face from detector: lower-case letters
60 e = E - labgeo.beamdir * (E(1) - samgeo.orig(1) - bb_lab(3)*0.5);
61 f = F - labgeo.beamdir * (F(1) - samgeo.orig(1) - bb_lab(3)*0.5);
62 g = G - labgeo.beamdir * (G(1) - samgeo.orig(1) - bb_lab(3)*0.5);
63 h = H - labgeo.beamdir * (H(1) - samgeo.orig(1) - bb_lab(3)*0.5);
64
```

```
% Calculate plane normal from [u, v, w]
% We don't know the position of the diffracting grain
% In this case, we assume scattering from the eight vertices of the sample
% bounding box we have just calculated
% We create a 1-to-1 correspondence between each point on detector (uvw)
% and the scattering points inside the sample
labBXYZ = [E; F; G; H; e; f; g; h];
labBXYZ = repmat(labBXYZ, length(u), 1);
rep = 1:length(u);
rep = rep(ones(1, 8), :);
rep = rep(:).';

% u, v, w vectors lengths amplified by 8 in order to correspond to 8
% vertices of sample bounding box
u_ext = u(rep, :);
v_ext = v(rep, :);
w_ext = w(rep, :);
[diffvec, ~, theta] = gtGeoDiffVecInLab([u_ext v_ext], labBXYZ, labgeo);
plane_normal = gtGeoScattVecFromDiffVec(diffvec, labgeo.beamdir);

% Calculate eta
eta = gtGeoEtaFromDiffVec(diffvec, labgeo);

% Calculate plane normal in SAM coordinates
om_step = 180 / parameters.acq.nproj;
rot_omega = w_ext * om_step;
[plane_normal_sam, ~] = gtGeoLab2Sam(plane_normal, rot_omega, ...
                        labgeo, samgeo, 0, 1);

% Calculate rotation angles at which Friedel pairs are observed
rotcomp = gtMathsRotationMatrixComp(rot_axis, 'col');
om = gtFedPredictOmegaMultiple(plane_normal_sam', sind(theta)', ...
     labgeo.beamdir', rot_axis, rotcomp, []);
om = reshape(om, 4, 8, []);

% Pair matrix gives, for each vertex of the sample bounding box, a
% prediction of the omega angle where the paired image is found
pair = zeros(8, length(u));
for iom = 1:length(u)
    if ( abs(w(iom)*om_step - om(1, :, iom)) < ...
         abs(w(iom)*om_step - om(2, :, iom)) )% we are dealing with a 1A spot
        pair(:, iom) = om(3, :, iom);          % get the 2A spot
    else                                      % we are dealing with a 1B spot
        pair(:, iom) = om(4, :, iom);          % get the 2B spot
    end
```

```
110 end
111
112 % Construction of pair_red matrix: among the 8 values for each spot, we
113 % save the minimum and the maximum for later definition of search
114 % intervals
115 low  = min(pair);
116 high = max(pair);
117 pair_red = [low; high];
118 end
```

A.2 Calculation of diffracting voxels by back-projection of two types of illumination masks

The algorithm for the calculation of active voxels with the procedure explained in subsection 6.4.4 is presented here. Basically, once the type of illumination has been chosen (either line beam of 7 μm thickness, or pencil beam, each ray having 7 μm $\times$ 7 μm section and with 49 μm period), the illumination mask on the forward detector can be back-projected on the sample volume. This is done for three reflections, two of which making a Friedel pair, by making use of ASTRA tomography library.

```
1  function active_vol = gtFedActiveVolumeVoxels(phase_vol, ...
2      parameters_inline, varargin)
3  % GTFEDACTIVEVOLUMEVOXELS    Backprojects the absorption
4  % image from a mask on the sample volume, obtaining the diffracting
5  % voxels for a given diffraction geometry.
6  %
7  % gtFedActiveVolumeVoxels(phase_vol)
8  % --------------------------------------------------------------------
9  %
10 % INPUT
11 %   phase_vol          = assembled phase volume reconstructed with 6D
12 %                        algorithm
13 %   parameters_inline = parameters for an in-line acquisition
14 %
15 % OUTPUT
16 %   active_vol         = three volumes with modulated intensities
17 %                        according to scattering powers, one for each
18 %                       considered reflection
19 %
20 % OPTIONAL INPUT
21 %   mask               = {'pencil', 'line'} [pencil by default]
```

```
22
23 conf = struct('mask', 'pencil');
24 conf = parse_pv_pairs(conf, varargin);
25
26 detgeo = parameters_inline.detgeo;
27 labgeo = parameters_inline.labgeo;
28 samgeo = parameters_inline.samgeo;
29 recgeo = parameters_inline.recgeo;
30 acq = parameters_inline.acq;
31 xyz = size(phase_vol.intvol);
32 mask = zeros(xyz(2), xyz(3));
33 vert_idx = round(xyz(2) / 2);
34
35 if strcmp(conf.mask, 'pencil')
36     % Creation of the pencil mask: 70 micron windows
37     % with 7 vx period, 1 vx vertical thickness
38     disp('Creating a pencil mask ...')
39     % Dealing with mask's period non multiple of
40     % the reconstructed voxel size
41     coords = (1:50:xyz(3)*7) / 7;
42     pmin = floor(coords);
43     pmax = pmin + 1;
44     cmin = pmax - coords;
45     cmax = 1 - cmin;
46     v(pmin + 1) = cmin;
47     v(pmax(cmax > 0) + 1) = cmax(cmax > 0);
48     v(end) = [];
49     mask(vert_idx, :) = v;
50 else
51     % Creation of the line mask: 1 vx vertical thickness
52     mask(vert_idx(1), :) = true;
53 end
54
55 % Manual correction of intensity volume
56 phase_vol_corr = double(phase_vol.intvol);
57
58 % Back-projection of absorption image into sample volume
59 pmo = [-88.2 91.8 -26.2];
60 omega = pmo + 90;
61 active_vol = zeros(xyz(1), xyz(2), xyz(3), numel(pmo));
62 for irefl = 1:numel(pmo)
63     fprintf(['Rotation angle = %f, pmo = %f : calculating projection ...'
64             'geometry ...\n'], omega(irefl), pmo(irefl))
65     proj_geom = gtGeoProjForReconstruction([], omega(irefl), [], ...
66             acq.bb, [0 0], detgeo, labgeo, samgeo, recgeo, ...
```

```
67              'ASTRA_absorption');
68      proj_stack(:, 1, :) = mask;
69      vol = gtASTRABackprojection(proj_stack, proj_geom, xyz(1), ...
70              xyz(2), xyz(3));
71      active_vol(:, :, :, irefl) = vol .* phase_vol_corr;
72  end
73
74  end
```

Thanks

Here I am at the end of a long journey, and this is the time I realize it wouldn't have been so special without a lot of people that I would like to thank.

I am very grateful for the prestigious experience Prof. Giacomo Ghiringhelli allowed me to do, and for the constant support and helpful advice he gave me from Milan.

I had one of the best experiences in my life here in Grenoble, something I will never forget. I found ESRF a welcoming and exciting place where I could grow and learn how science means hard work, but it becomes enjoyable if you share it with some really excellent colleagues. I am truly indebted to Dr. Wolfgang Ludwig, who took on a big challenge, letting in his office a rookie scientist (real scientists will forgive me for using this word!!) and always bearing with him. His helpfulness and his good will are an example for him.

I had the pleasure to benefit from the teaching of Nicola, as well, who will earn his PhD very soon. Good luck and congratulations! I thank him for all the time he stole from his own thesis work, to give precious advice and instill the beauty of a well written and efficient code into my mind. But I wouldn't be fair if I didn't thank him for all the time spent together, both at ESRF and outside, sharing funny and not always "politically correct" stories (he had way more than me, though!). I feel very lucky because these two guys never left me alone, and were always willing to help me solve my troubles. I am proud of having them as conventional (and unconventional) mentors. I wish them all the very best.

A special thank is for the friends and flatmates I shared the everyday life with. Starting from the most recent experience in Grenoble, I would like to thank Andrea and Fabio for being two reliable and excellent life companions. Looking back at the early past, I must admit that part of my heart is still living in Via Ronchi, together with a crew of crazy and legendary friends. The group includes: Andre, my very first friend in Milan, so I owe him a lot; Guasto, the best colleague with whom I grasped the meaning of a lot of apparently meaningless physics equations, but above all a real

friend, always supporting me; then Ferro, Sara, Simo, Villa, Andrea (the Grenoble flatmate, here he goes again), Boa, and Raggio. I tried to do all my best for you, and I beg your pardon if I didn't manage sometimes.

I would also like to thank my hometown friends, for never excluding me from their group even if I am often far from them. I hope they will forgive me.

I wouldn't be writing these lines without all the support and love from my family: my mother, my father, and my brother, for always having a word for me. I seldom had many words for them, but still I owe them everything. They have been encouraging me to do all my best since I was a young child, so this work is dedicated to them and to the sacrifices they made for allowing me to study at Polytechnic University of Milan. This thesis is also meant to be the best present I could give to all of my grandparents, since I've never been very good at showing my feelings with words.

Last, but not least, my heartfelt thanks go to Alessandra, the person who (madly) decided to bear with an insane Physics Engineer who stole a huge deal of time from her. Despite that, she always supports my choices, even when they involve being far from each other. All the sacrifices she's been doing for two years are meant to make me a really happy person. I would be glad if I could one day return just half of what she's giving to me.

Lorenzo